LBNL-39840
UC-411

ERNEST ORLANDO LAWRENCE
BERKELEY NATIONAL LABORATORY

The Structures and Dynamics of Atomic and Molecular Adsorbates on Metal Surfaces by Scanning Tunneling Microscopy and Low Energy Electron Diffraction

Hyungsuk Alexander Yoon
Materials Sciences Division

December 1996
Ph.D. Thesis

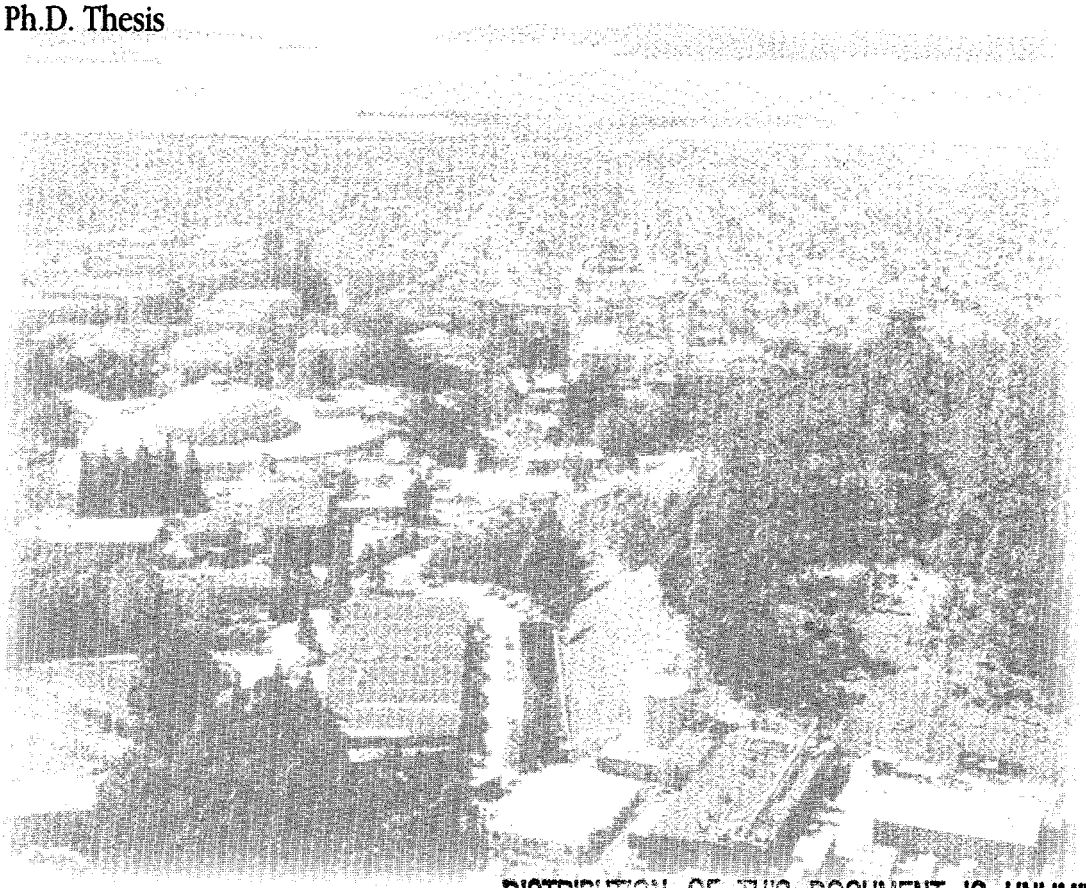

LBNL-39840
UC 411

The structures and dynamics of atomic and molecular adsorbates on metal surfaces by scanning tunneling microscopy and low energy electron diffraction

Hyungsuk Alexander Yoon
Ph.D. Thesis

Department of Chemistry
University of California

and

Materials Sciences Division
Lawrence Berkeley National Laboratory
University of California
Berkeley, CA 94720

December 1996

This work was supported by the Director, Office of Energy Research, Office of Basic Energy Science, Materials Sciences Division, of the U.S. Department of Energy under Contract No. DE-AC03-76SF00098

The structures and dynamics of atomic and molecular adsorbates on metal surfaces by scanning tunneling microscopy and low energy electron diffraction

by

Hyungsuk Alexander Yoon

B.S. (University of California at Los Angeles)

A dissertation submitted in partial satisfaction of the
requirements for the degree of
Doctor of Philosophy

in

Chemistry

in the

GRADUATE DIVISION

of the

UNIVERSITY of CALIFORNIA at BERKELEY

Committee in charge
Professor Gabor A. Somorjai, Chair
Dr. Miquel Salmeron, Co-chair
Professor Paul Alivisatos
Professor Alex Zettl

1996

The structures and dynamics of atomic and molecular adsorbates on metal surfaces by scanning tunneling microscopy and low energy electron diffraction

by

Hyungsuk Alexander Yoon

Dedicated to my parents,

Abstract

The structures and dynamics of atomic and molecular adsorbates
on metal surfaces by scanning tunneling microscopy
and low energy electron diffraction

by

Hyungsuk Alexander Yoon
Doctor of Philosophy in Chemistry

University of California at Berkeley

Professor Gabor A. Somorjai, Chair
Dr. Miquel Salmeron, CO-chair

Studies of surface structure and dynamics of atoms and molecules on metal surfaces are presented. My research has focused on understanding the nature of adsorbate-adsorbate and adsorbate-substrate interactions through surface studies of coverage dependency and coadsorption using both scanning tunneling microscopy (STM) and low energy electron diffraction (LEED).

The effect of adsorbate coverage on the surface structures of sulfur on Pt(111) and Rh(111) was examined. On Pt(111), sulfur forms p(2x2) at 0.25 ML of sulfur, which transforms into a more compressed ($\sqrt{3}$x$\sqrt{3}$)R30° at 0.33 ML. On both structures, it was found that sulfur adsorbs only in fcc sites. When the coverage of sulfur exceeds 0.33 ML, it formed more complex c($\sqrt{3}$x7)rect structure with 3 sulfur atoms per unit cell. In this structure, two different adsorption sites for sulfur atoms were observed - two on fcc sites and one on hcp site within the unit cell.

In contrast to Pt(111) the lowest coverage of ordered sulfur formed on Rh(111) was the $(\sqrt{3}x\sqrt{3})R30°$ overlayer at 0.33 ML, in which the adsorption site of sulfur was determined to be fcc site from LEED I-V analysis. When the sulfur overlayer was compressed by adsorbing additional sulfur atoms on the surface, it forms a c(4x2) overlayer at 0.5 ML. STM experiments clearly show that there are two different adsorption sites for sulfur in this structure, notably one fcc and one hcp site in the unit cell. A (4x4) overlayer can also be formed at the same sulfur coverage as the c(4x2) structure as determined by Auger electron spectroscopy, but at a higher annealing temperature. STM images of the (4x4) overlayer show that all sulfur atoms have same adsorption site, presumably fcc site, but the distances between sulfur atoms are much shorter than those for the c(4x2) structure, suggesting the cluster formation. This is more evident in a (7x7) structure, which it is postulated to form a surface sulfide with sulfur dissolved into the subsurface. In order to accommodate the large number of sulfur atoms on the surface, the substrate metal atoms may have gone through reconstruction to form a more energetically stable overlayer.

STM was also used to study the structures of carbon monoxide on Rh(111) surface at different partial pressures of CO. Carbon monoxide forms two different (2x2) ordered overlayers depending on the background pressure of CO. At low pressure, ¼ ML structure was observed, while at the high partial pressure of CO, the coverage increased to ¾ ML and the formation of CO cluster were observed.

The coadsorption of benzene and carbon monoxide was used as a model system to elucidate the interaction between different molecular species on Rh(111) surface. Benzene

molecules do not form a long range ordered overlayer on Rh(111) at saturation coverage, but form well ordered overlayers when they were coadsorbed with carbon monoxide. When the coverage of benzene reaches approximately 0.5 ML, only benzene molecules at the top side of the step edges were imaged, while those on the terraces could not be imaged by the STM due to rapid diffusion. However, coadsorption of carbon monoxide decreased benzene mobility which could then be imaged by STM. The attractive interaction between benzene and carbon monoxide on Rh(111) surface contributes to the inhibition of benzene diffusion and the enhancement of surface overlayer ordering. Para- and meta-xylene and their coadsorption with carbon monoxide were also studied. These structural isomers have different shape in the STM images. When coadsorbed, the intercalation of CO with meta-xylene was observed suggesting the attractive interaction between these two molecules.

Table of Contents

List of Tables

List of Figures

Acknowledgments

I would like to extend my sincere gratitude to my advisor Professor Gabor Somorjai for providing the opportunity to perform research in his group. His enthusiasm in surface science, catalysis and science in general continues to intrigue me. I would also like to thank Dr. Miquel Salmeron whose encouragement and helpful discussions made this work possible. Both Gabor and Miquel deserve thanks for creating a research group of very good scientists with whom I've been fortunate to interact both inside and out of the lab.

I also would like to acknowledge the past and present members of the Somorjai and Salmeron groups. I would especially like to thank Dr. Uli Starke who taught me all I know about the vacuum chamber. I would also like to thank Dr. Nick Materer for his help and encouragement. He also took my LEED data and analyzed results of which appear in this dissertation. Also thanks to Dr. Frank Ogletree, Jim Dunphy, and Heather Galloway who helped me on numerous occasions about the problems with STM. Other people who deserves my thanks includes Joung, Michael, Julius, Pete, Enrico, Howard, Rudy, John, Yong-Ki, Craig, Joel and Paul, with whom I could enjoy the life at Berkeley both in and out of the lab. I would especially like to thank Howard Fairbrother and Craig Tewell for proofreading this dissertation. Their professional relationship and friendship is something that I will never forget.

I am very grateful for Bob Kehr and Mae Lum for their help in circumventing bureaucratic situations. I am also thankful to the technical staff of the Chemistry

Department and LBL. Thanks to Hans, Chuck and Eric for making all the main parts of my microscope. Henry has fixed all the electronics over the years. James Wu has provided many special tip wires and other materials.

Last but not least, I would like to thank my parents, my sister and brother who believed in me and encouraged me over the years.

This work was supported by the Director, Office of Energy Research, Office of Basic Energy Sciences, Materials Science Division of the U.S. Department of Energy under Contract No. DE-AC03-76SF00098.

Chapter 1

Introduction

The study of surfaces has been aimed at achieving an atomic or molecular level understanding of important technologies that rely on the surface properties of materials, such as catalysis [1], lubrication [2], adhesion [3], and microelectronics devices [4]. Intrinsically, the surface is more difficult to study than the bulk as there are only 10^{15} atoms/cm^2 at the surface compare to 10^{24} atoms/cm^3 in the bulk. As a result, experimental techniques for surface studies must be able to detect signals associated with a relatively small number of atoms in addition to discriminating those atoms from the bulk. For the last thirty years, the developments of new 'surface sensitive' or 'surface specific' techniques allowed one to explore the chemistry and the physics of the surface and related phenomena.

The studies of chemisorbed atoms and molecules have provided a fundamental understanding to heterogeneous catalysis, adhesion, and friction. To understand how chemical reactions occur on the surface, one must know the chemical composition and

the structure of the surface, how the atoms and molecules bond to the surface, and as well as how they interact with the surface and/or with one another.

This work focuses on the structures and dynamics of atoms and molecules on metal surfaces. These experiments have been performed using scanning tunneling microscopy (STM) and low energy electron diffraction (LEED). Low energy electron diffraction has been used widely to determine the surface structure of atomic species and small molecules [5, 6]. The improvement in the LEED calculations allow one to solve the surface structure within an accuracy of 0.01 Å. However, LEED is a diffraction technique which does not provide information of the local structure nor how to solve surface structures involving large unit cells or complex structures since a large number of parameters must be considered. The invention of scanning tunneling microscopy by Binnig and Rohrer, and the related scanning probe microscopy (SPM) techniques, open a new door to study of the nature of the surface and interface [7-9].

In this work, experiments were carried out to elucidate the interactions between adsorbate and substrate as well as between adsorbates on transition metal surfaces through a determination of the surface structure and its variation with external parameters such as adsorbate coverage. To carry out these task, two different approaches have been employed.

The first method is to study the coverage dependency on the surface structure of an adsorbate. The study of sulfur adsorption on Pt(111) and Rh(111) falls in this category. Sulfur is ideal for this type of study since several different ordered structures can be produced on a given surface. The structures of different sulfur overlayers on Pt(111) and Rh(111) has been determined with both LEED and STM. LEED was used to

solve the detailed structures of the (2x2) and the ($\sqrt{3}$x$\sqrt{3}$)R30° sulfur overlayers on Pt(111). The results from these LEED analyses were extrapolated to determine the structures of more complex sulfur overlayers, such as Pt(111)-c($\sqrt{3}$x7)rect-3S, Rh(111)-c(4x2)-2S and Rh(111)-(4x4)-8S.

The other method employed to study the interaction between adsorbates was to look at coadsorption systems. Since many real surface phenomena involve more than one adsorbed species, such as poisons and promoters in heterogeneous catalysis, this approach would give a more relevant understanding of the real problem. The study of the structures of one chemical species and the change of the its structure due to the coadsorption of another will allow one to understand the interaction between two different chemical species. To this end, the benzene and carbon monoxide coadsorption system was studied, as well as the para- and meta-xylene and their coadsorption with carbon monoxide on Rh(111) surfaces.

In this dissertation, first, different surface techniques are presented with emphasis on the principles and operations of LEED and STM. Then the LEED and STM studies on the structures of sulfur overlayer on Pt(111) and Rh(111) are presented, followed by the pressure dependent structures of carbon monoxide on Rh(111). Then the work on the coadsorption systems are presented. The structure of benzene and its coadsorption with carbon monoxide is discussed first followed by the studies on para- and meta-xylene and their coadsorption with carbon monoxide.

Chapter 1 References

1. G.A. Somorjai, *Chemistry in Two Dimensions: Surfaces*. 1981, Ithaca, NY: Cornell University Press.
2. A. Leonard, *Lubrication and lubricants*. 1907, London: Griffin.
3. M. Grunze and H.J. Kreuzer, *Adhesion and Friction : Proceedings of the Third International Workshop on interface Phenomena*. 1989, New York: Springer-Verlag.
4. S.A. Campbell, *The science and engineering of microelectronic fabrication*. 1996, New York: Oxford University Press.
5. M.A. Van Hove, W.H. Weinberg, and C.-M. Chan, *Low Energy Electron Diffraction*. 1986, Berlin, Heidelberg, New York: Springer-Verlag.
6. M.A. Van Hove, W. Moritz, H. Over, P.J. Rous, A. Wander, A. Barbieri, N. Materer, U. Starke, D. Jentz, J.M. Powers, G. Held, and G.A. Somorjai, Surf. Sci. Rep., 1993. **19**: p. 191.
7. G. Binnig, H. Rohrer, C. Gerber, and E. Wiebel, Phys. Rev. Lett., 1982. **49**: p. 57.
8. G. Binnig, H. Rohrer, C. Gerber, and E. Wiebel, Appl. Phys. Lett., 1982. **40**: p. 178.
9. G. Binnig, H. Rohrer, C. Gerber, and E. Wiebel, Phys. Rev. Lett., 1983. **50**: p. 120.

Chapter 2.

Experimental Methods

2.1 Introduction

In order to study the structures and dynamics of adsorbates on the surface, it is necessary to have some idea about the surface, such as how clean it is, what adsorbates are on the surface, and how well it is ordered. In order to carry out successful experiments, it is required to prepare and characterize the surface before and after the experiments. Ultrahigh vacuum (UHV) chamber was used to carry out the experiments. In this chapter, the ultrahigh vacuum system that has been used for this dissertation will be discussed along with the techniques and the equipment used. However, the principles and experimental details of scanning tunneling microscopy (STM) and low energy electron diffraction (LEED) are described in the following chapters since these techniques are used extensively for this work.

2.2 Ultrahigh Vacuum (UHV) Chamber

Experimental surface science requires a well-characterized surface for at least the duration of a experiment. Most clean metal surfaces are highly reactive with oxygen- and carbon-containing contaminants present in the laboratory environment. In order to keep a surface in its clean or otherwise well characterized condition, a good vacuum is needed. The necessary quality of vacuum can be approximated by considering the arrival rate of molecules to the surface [1]. The arrival rate (r) of molecules to the surface using simple kinetic theory of gases is:

$$r = 3.51 \, x \, 10^{22} \frac{P}{\sqrt{TM}} \qquad (2.1)$$

where P is pressure (torr), T is temperature (K) and M is atomic mass unit. If we consider the arrival rate of carbon monoxide (CO) molecules at room temperature and 1 torr, they have an arrival rate of 3.83 x 10^{20} molecules $cm^{-2}s^{-1}$. If all of these molecules stick to the 1 cm^2 area of the sample (approximately 10^{15} metal atoms per cm^2), they form a monolayer in about 3 x 10^{-6} seconds. It is from this consideration that the unit *Langmuir* (L) is derived. One *Langmuir* is 1 x 10^{-6} torr•sec and it represents the exposure corresponding to 1 ML coverage. This unit is used experimentally to measure the exposure of gas molecules. To have contamination rate of only a few percent of a monolayer for an hour, a pressure of approximately 10^{-10} torr or less is required. This range of pressure is referred to as ultrahigh vacuum or UHV.

Studies carried out for this dissertation were conducted in a standard Varian ultrahigh vacuum chamber. This stainless-steel chamber is equipped with a sample

manipulator, a four-grid low energy electron diffraction (LEED) optics for LEED and used as a retarding field analyzer (RFA) for Auger electron spectroscopy, a mass spectrometer for residual gas analysis, an ion sputter gun for cleaning the sample, a solid state electrochemical sulfur source and an ultrahigh vacuum scanning tunneling microscope (STM). The total pressure of the system is measured with a UHV ionization gauge. Schematics of the camber is shown in Figure 2.1.

The single crystal sample is mounted on a sample holder with tantalum strips as illustrated in Figure 2.2. The sample holder is made out of molybdenum, chosen for its good thermal conductivity. The sample holder is then clamped to the sample manipulator as shown in Figure 2.3.

In this way, the sample is transferred to the scanning tunneling microscope from the sample manipulator where the sample can be cleaned, prepared and characterized by surface analysis techniques. The sample in the manipulator can be translated in the x, y and z directions and can be rotated to face various preparation and analysis facilities in the chamber. The crystal is heated with electron bombardment when the sample is in the sample manipulator. The electron bombardment heater is made out of a 5 mil tungsten filament from which electrons are thermally emitted, then accelerated toward to the sample which in turn heats the sample to 1200 K. The sample is cooled to 90 K by flowing liquid nitrogen through the cooling block which is in mechanical contact with the sample.

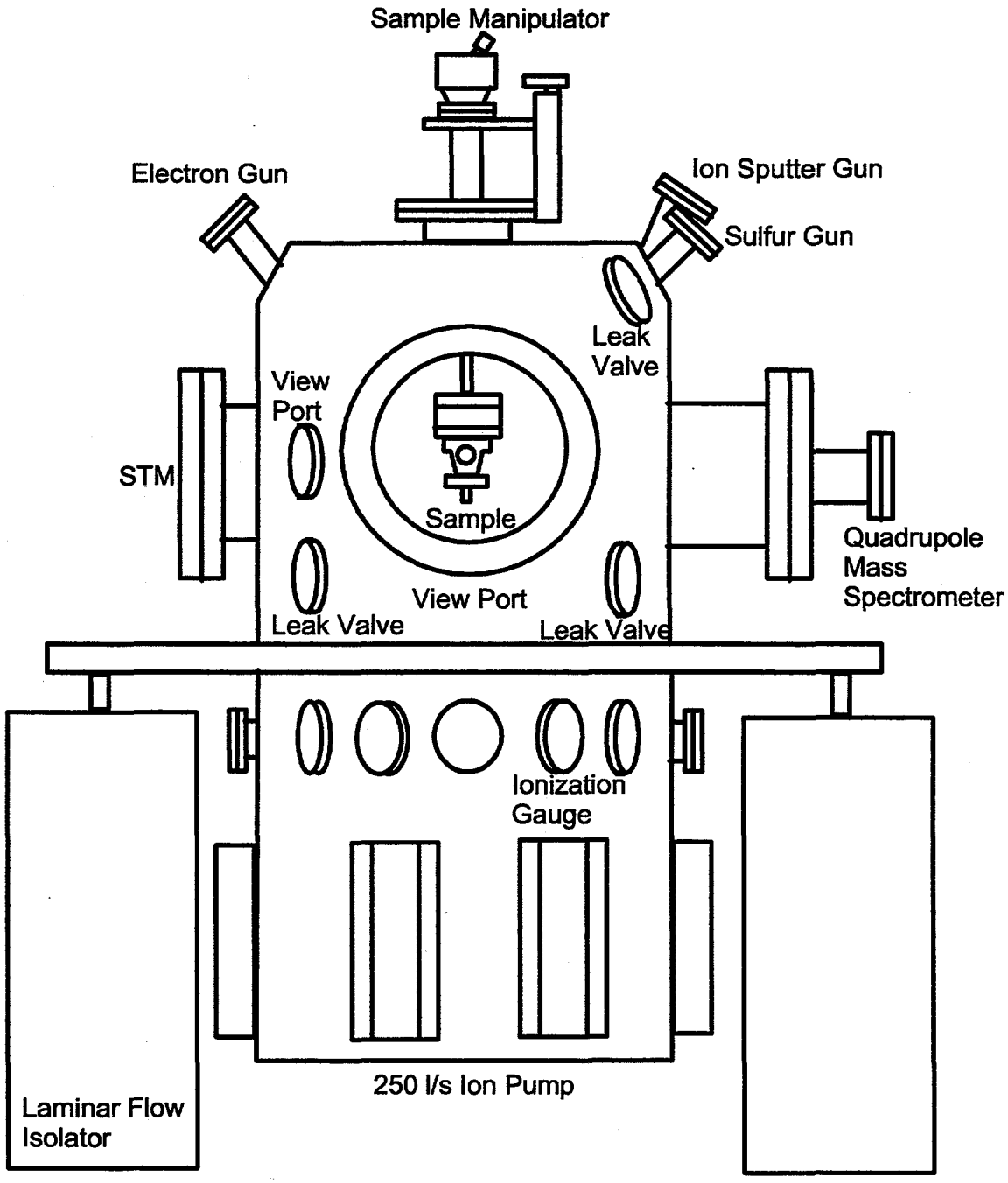

Figure 2.1 (a) The schematic of the UHV chamber used in this study. For clarity, the LEED optics and turbo molecular pumps were not shown.

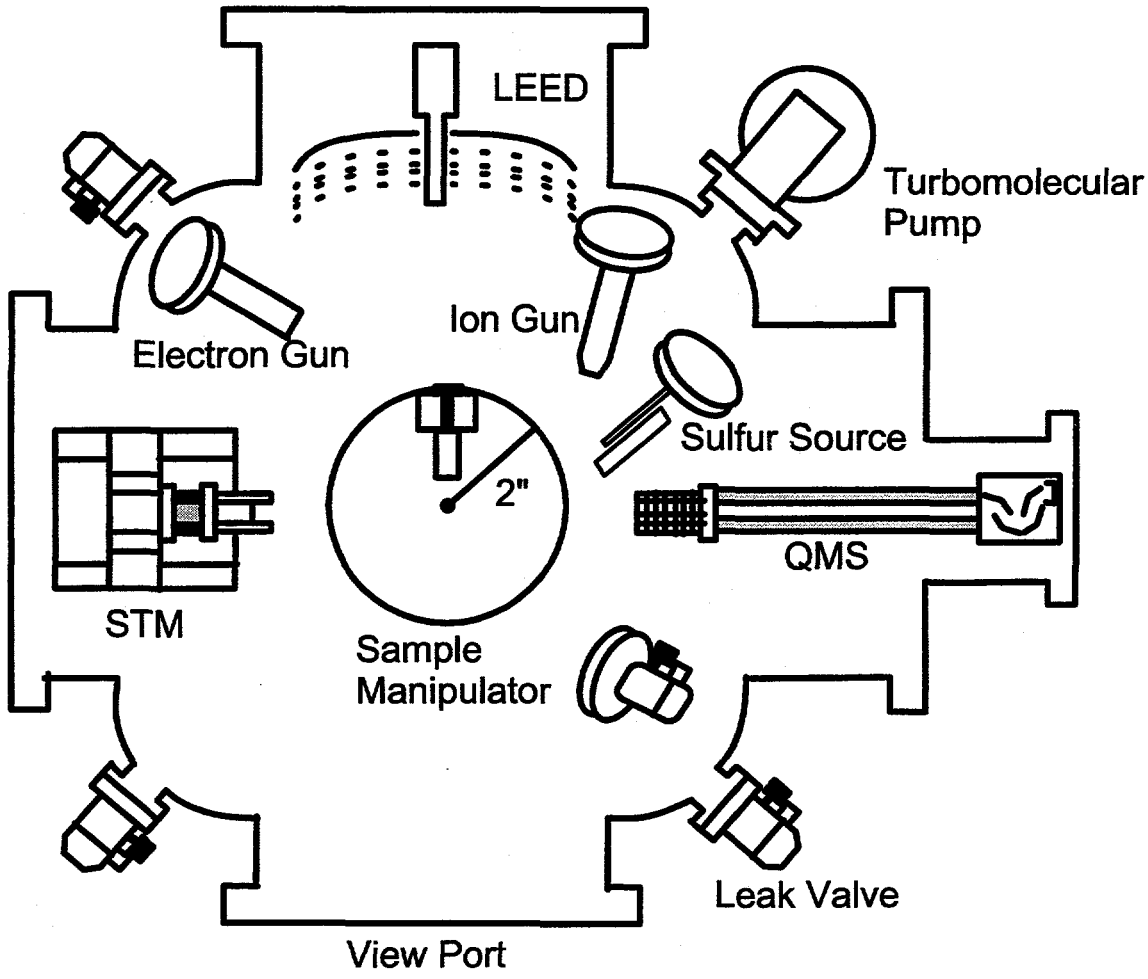

Figure 2.1 (b) Cross sectional view of the chamber showing the arrangement UHV setup.

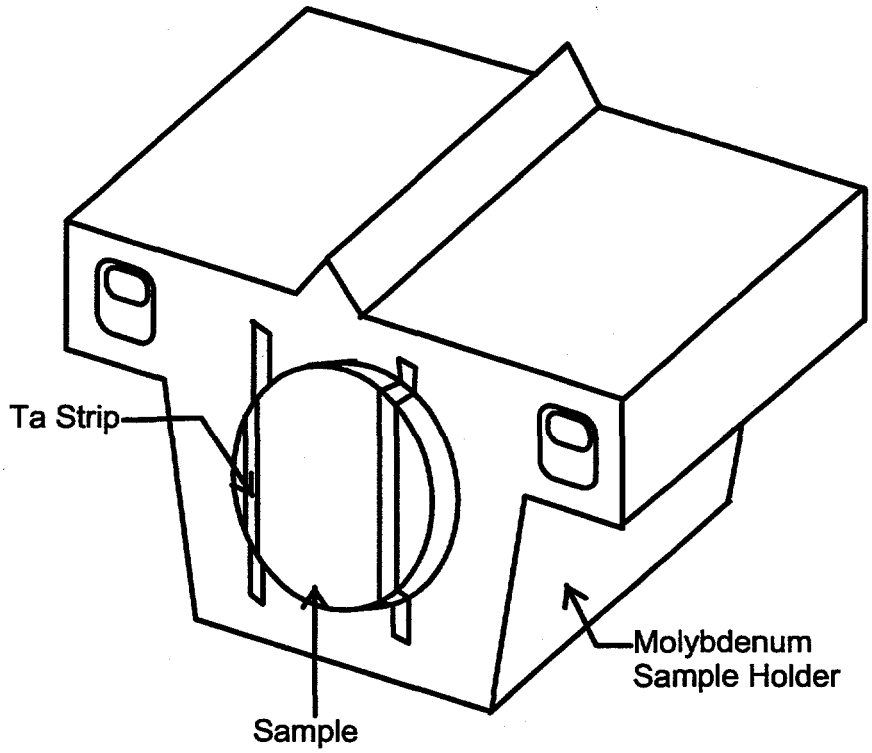

Figure 2.2 The schematics of the sample holder used in the studies for this dissertation. A single crystal sample is tightly held to the sample holder by two tantalum strips.

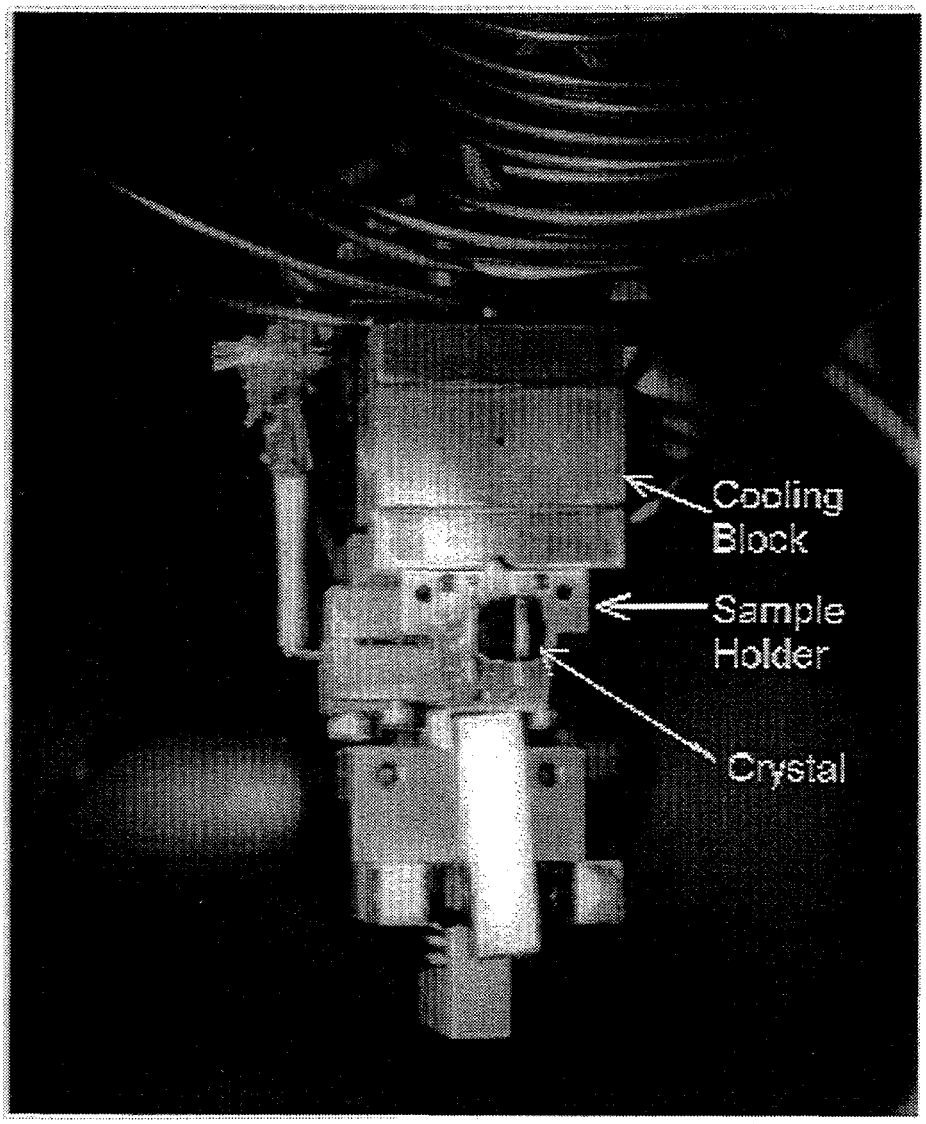

Figure 2.3 The photograph of a sample manipulator. The sample is mounted on the sample holder which is clamped to the manipulator. The cooling block is visible.

For STM, the sample holder is simply removed from the sample manipulator and set onto the rails of the outer tube of the microscope. The description on the STM will be discussed in the following chapter.

The vacuum is achieved in three steps. Rough pumping is provided either by a sorption pump or a dual stage mechanical pump. Either pump can evacuate the system down to a 200 to 400 millitorr range. A turbo molecular pump (Balzers Model TPU 060) backed by a mechanical pump is used to get high vacuum (down to 10^{-6}-10^{-7} torr). The ultrahigh vacuum (low 10^{-10} torr) can be achieved by an ion pump and intermittent use of a titanium sublimation pump (TSP). Typical base pressure when running experiments ranges from 7 x 10^{-11} to 5 x 10^{-10} torr after bakeout of the chamber. The background gases are mainly composed of hydrogen and carbon monoxide with small trace amount of carbon dioxide, methyl and carbon as detected by residual gas analyzer (UTI 100C mass spectrometer).

2.3 Sample preparation

The samples used in this dissertation are platinum and rhodium single crystals. The crystal boules are first oriented with Laue X-ray diffraction to the desired index plane surfaces, then sliced and polished [2, 3]. The electric discharge machine (EDM) is used to cut slices of single crystals. The polishing consisted of two steps. Rough polishing is carried out with silicon-carbide (SiC) sand papers of different grades, then diamond pastes are used for fine polishing. For both Pt and Rh, the final polishing of crystals were

carried out with 1 μm diamond paste. The rest of the sample preparation is carried out in an ultrahigh vacuum chamber. The basic method for cleaning the surface of a single crystal is to perform repeated cycles of argon ion sputtering, annealing and heating in a reactive gas such as oxygen [4]. Since the mechanical and chemical properties of Pt and Rh samples are similar, virtually identical cleaning processes are employed. Layers of contaminants are removed by sputtering with 0.5 to 2 keV argon ion (Ar^+) using ion gun in 5 x 10^{-5} torr of argon. The crystal is then heated at 500 to 1000 K with the electron bombardment heater. The temperature of the sample is measured within ± 20 K with an optical pyrometer (IRCON) calibrated with a type K thermocouple in a similar chamber. For oxidation or oxygen treatment, the sample is annealed at 700 to 800 K in the presence of 5 x 10^{-8} to 1 x 10^{-7} torr of oxygen to burn any carbon contaminant off the surface.

Most common contaminants are easily identified using Auger electron spectroscopy (AES). The sample cleaning is repeated until no contaminants are detected by AES. The resulting surface has a very sharp low energy electron diffraction pattern free of any background intensities.

2.4 Auger Electron Spectroscopy

Auger Electron Spectroscopy (AES) provides a method of identifying the chemical compositions of the surface. An electron beam with an incident energy of 2

keV is directed on to the sample at a glancing angle (~ 15 °) and the electrons ejected from the sample are collected with an energy analyzer.

Electron with high incident energy eject an inner shell electron creating a hole in the core level. The outer shell electron decays to fill the core hole. The process proceeds either by the emission of a photon (X-ray) or the ejection of an Auger electron as the energy is transferred to an electron in the outer shell. The Auger process is illustrated in Figure 2.4.

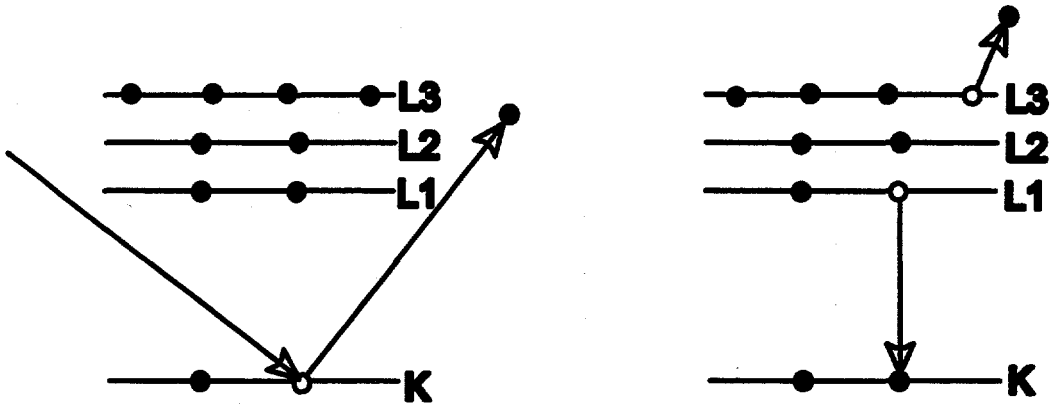

Figure 2.4 The schematic of Auger electron process. The energetic electron knocks an electron in the core level of the atom, then one of the valence electrons decay, then the energy is transferred to an electron in the outer level (Auger electron).

The energy of the ejected electron is given by:

$$\Delta E = (E_K - E_{L1}) - E_{L3} \qquad (2.2)$$

where the subscripts refer to the levels depicted in Figure 2.4. As this energy is specific to an element, chemical identification of the surface can de obtained. The method is surface specific since most Auger electrons have energy corresponding to an escape depth in the order of the first few layers beneath the surface. Surface sensitivity can be enhanced by using an off-axis electron gun at 15° glancing angle.

Four-grid low energy electron diffraction optics are used to collect Auger electrons in the retarding field mode. The principle of operation of retarding field analyzer is illustrated in Figure 2.5. In order to enhance the sensitivity, the derivative of the number density of electron (dN(E)/dE) is being used. The derivation is achieved by modulating the voltage to the grid, then detecting the second harmonic of the signal with a lock-in amplifier. The detailed procedure can be found in several references [1, 5, 6]. These spectra can be easily compared to reference spectra to determine the chemical composition of the surface species. Figure 2.6 is an Auger electron spectrum of clean rhodium surface.

In addition to the qualitative use of AES to identify the elements on the surface, the quantitative analysis can be also carried out. The quantitative analysis is used to determine the surface coverage of sulfur on Rh(111) surfaces by comparing the relative intensity of adsorbate and the substrate which will be discussed in a later chapter.

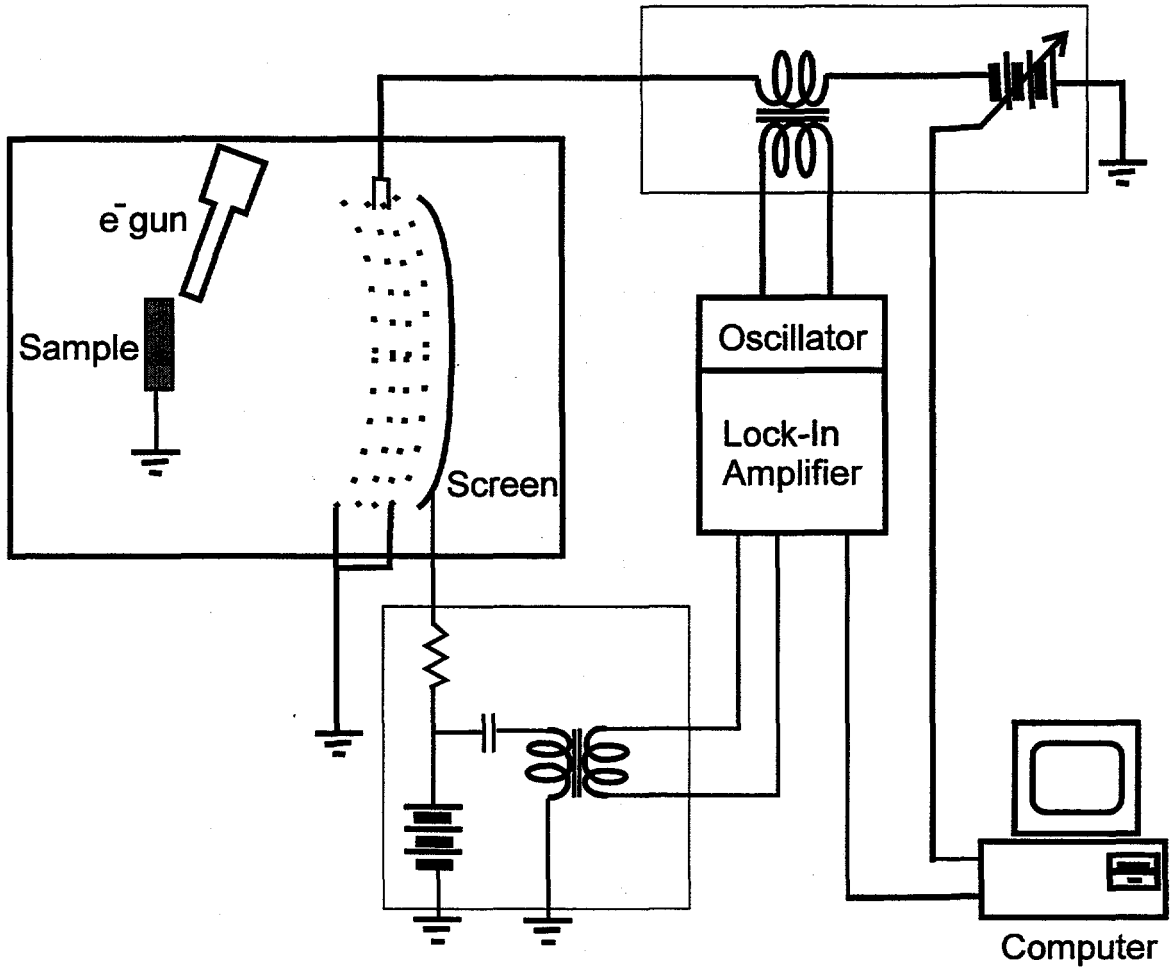

Figure 2.5 The schematic of AES experimental setup using Retarding Field Analyzer (RFA).

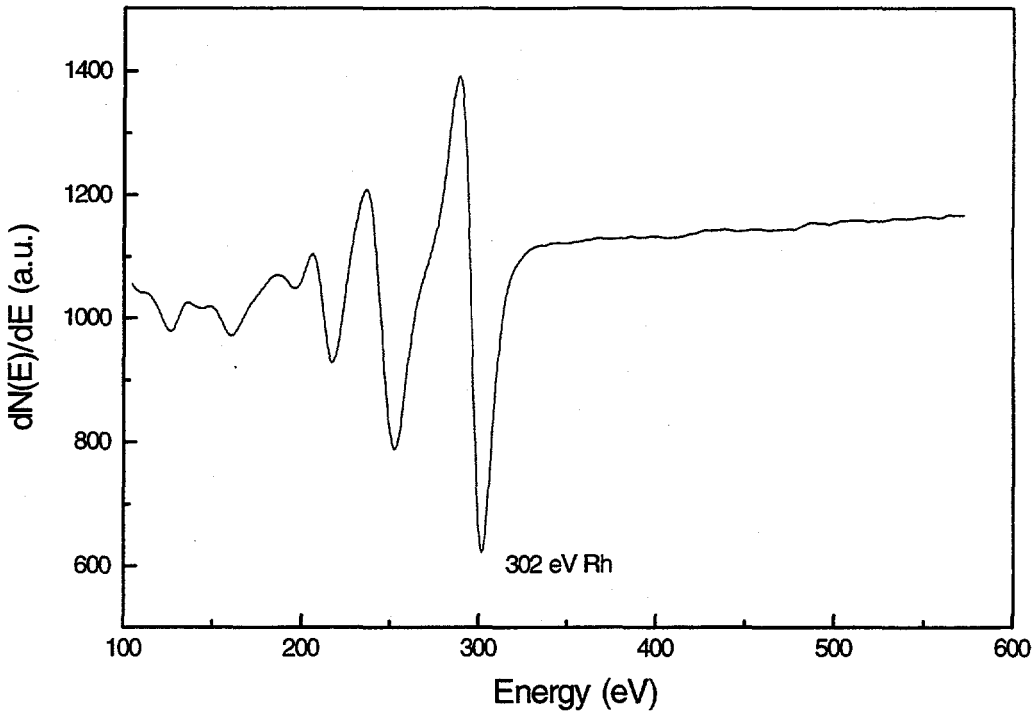

Figure 2.6 An Auger electron spectrum of clean rhodium surface.

2.5 Electrochemical Sulfur Source

Chapters 5-7 involve the structure of sulfur on Pt(111) and Rh(111) surfaces. In both studies, the solid-state electrochemical sulfur source (Pt/Ag/AgI/AgS/Pt) was utilized to deposit sulfur on the surface [7]. The schematic diagram of the source is shown in Figure 2.7.

Silver iodide (AgI) becomes conductive when it is heated to 400 K. By applying the voltage across the cell, silver sulfide is decomposed into sulfur and silver metal.

Mass spectrometer data indicate mainly the dimeric form of sulfur (S_2) is produced which evaporates in a conical beam towards the sample. The half cell reactions are:

$$Ag_2S \longrightarrow 2Ag^+ + \frac{1}{2}S_2 + 2e^- \qquad \text{(Anode)} \qquad (2.3)$$

$$2Ag^+ + 2e^- \longrightarrow 2\,Ag \qquad \text{(Cathode)} \qquad (2.4)$$

and the overall cell reaction is:

$$Ag_2S \longrightarrow 2\,Ag + \frac{1}{2}S_2 \qquad (2.5)$$

A potential of 0.2 V was applied to the cell to induce the reaction. The exposure can be controlled either by the current to the cell or by the exposure time. Typically, 1 A of current through the cell produces 1.56 x 10^8 S_2 molecules per second. Using this source we attained much higher coverages than by use of H_2S gas [8].

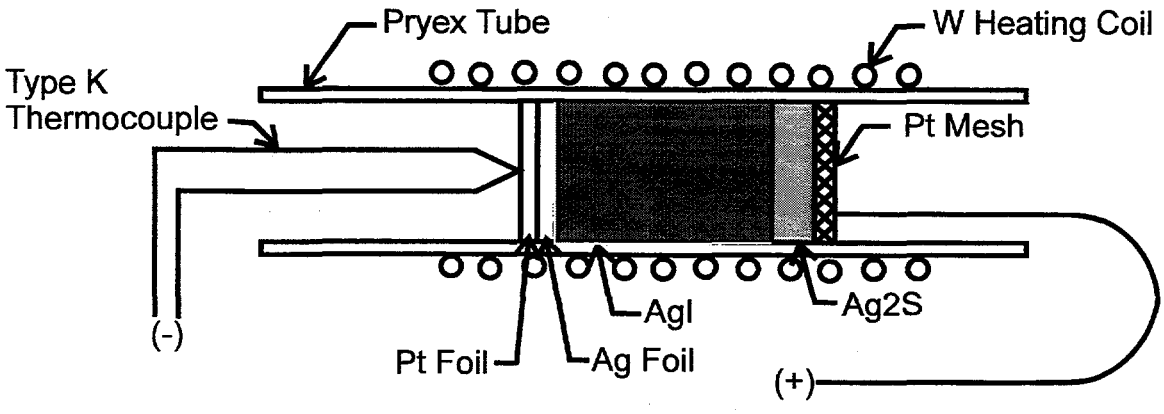

Figure 2.7 The schematic diagram of electrochemical sulfur source.

Chapter 2 References

1. D.P. Woodruff and T.A. Delchar, *Modern techniques of surface science*. 1986, Cambridge: Cambridge University Press.
2. E.A. Wood, *Crystal Orientation Manual*. 1963, New York: Columbia University Press.
3. W. Heppler, *Crystal Preparation at LBL, 1976 to 1986*. 1987, Berkeley: LBL Publication.
4. R.G. Musket, W. McLean, C.A. Colmenares, D.M. Makowiecki, and W.J. Siekhaus, Applications to Surf. Sci., 1982. **10**: p. 143.
5. G. Ertl and J. Küppers, *Low Energy Electrons and Surface Chemistry*. 1974, Weinheim: Verlag Chemie.
6. G.A. Somorjai, *Chemistry in Two Dimensions: Surfaces*. 1981, Ithaca, NY: Cornell University Press.
7. C. Wagner, J. Chem. Phys., 1953. **21**: p. 1819.
8. J.S. Foord and A.E. Reynolds, Surf. Sci., 1985. **152/153**: p. 426.

Chapter 3

Scanning Tunneling Microscopy (STM)

3.1 Introduction

The Scanning Tunneling Microscope (STM) was first invented by Binnig and Rohrer [1-3] in 1982 and since then it has been widely used to study metal and semiconductor surfaces at the atomic scale [4-7]. STM has been used to determine the adsorption site of atoms and molecules [8-10], diffusion of adsorbed atoms [11], organic overlayers [12, 13] and coadsorption systems [14]. Recently the development of STM theory has proven to be effective to distinguish the different contributions to the tunneling current [15-18]. In this chapter, the principles of STM and the UHV STM used for this dissertation are discussed

3.2 Principle of Operation

STM is based on the quantum mechanical effect of electron tunneling between two conducting solids through a classically forbidden energy barrier. In classical mechanics, the electrons in a solid are confined to the interior by a potential barrier at the surface. In the quantum mechanics, electrons are not confined within the potential barrier, but rather the amplitude of the electron wavefunction decays exponentially away from the surface. When the two solids are brought very close to each other such that the electron wavefunctions overlap, electrons can 'tunnel' from one solid to another.

In an STM experiment, a sharp tip is brought extremely close to a conducting sample (< 10 Å) so that electron tunneling through the vacuum gap can take place. The tunneling current is given by:

$$I \propto e^{-2d\kappa} \tag{3.1}$$

where d is the distance between the tip and the sample, κ is the reciprocal of the decay length of the electron wavefunction. κ is given by:

$$\kappa = \sqrt{\frac{2m\Phi}{h^2}} \tag{3.2}$$

where Φ is the average barrier height. Figure 3.1 illustrates the concept of tunneling in a STM. The average barrier height can be estimated by:

$$\Phi = \frac{1}{2}(\phi_{tip} + \phi_{sample}) - (E - \frac{eV_{Bias}}{2}) \tag{3.3}$$

for electrons tunneling into the empty states of the sample at an energy E above the sample Fermi level for a positive sample bias (V_{bias}).

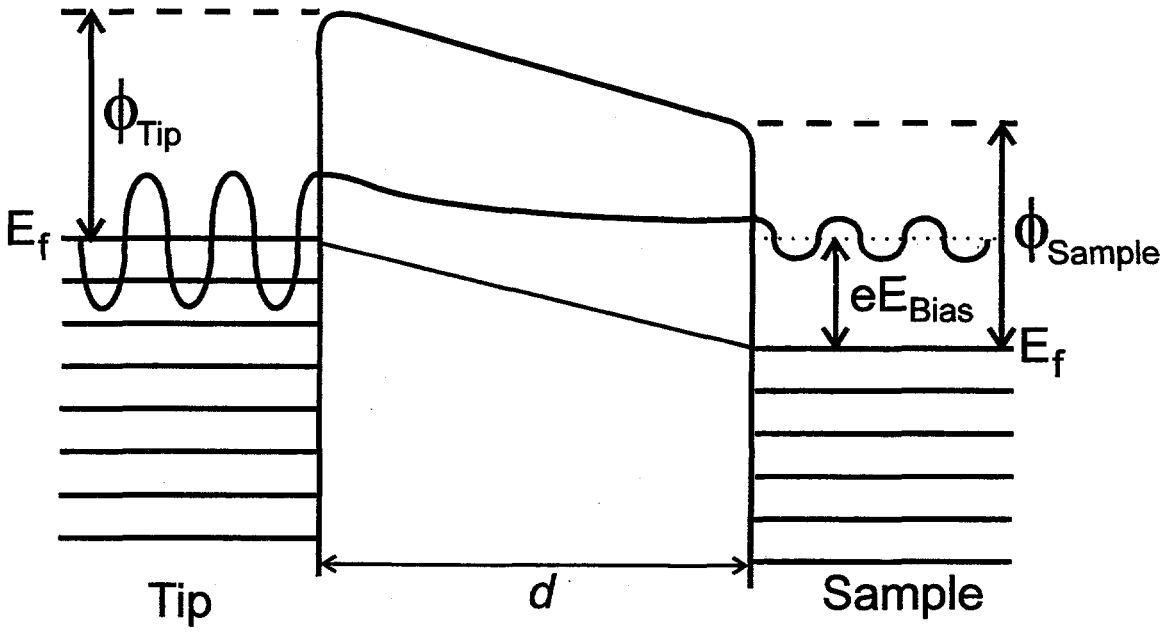

Figure 3.1 A model of the tunneling barrier. In STM tip and the sample are brought close together to allow their wavefunctions to overlap. The electron wave function decays exponentially in the barrier because the potential in the vacuum region is higher than the Fermi level. When the bias voltage is applied , a net current flow is produced.

ϕ_{tip} and ϕ_{sample} are the workfunctions of the tip and the sample respectively. Bias voltage is applied across the barrier to have a net current. When the sample is positively biased, the direction of electron flow is from tip to sample (direction of the current is from sample to tip), thus the STM images the empty states of the sample. Similarly, when the sample is negatively biased, the electron tunnels from sample to tip, thus STM provides an image reflecting the filled states of the sample.

The exponential decay of the tunneling current attributes the high spatial resolution of a STM. For a average workfunction value of 4 eV, the change in gap distance (d) by 1 Å, changes the tunneling current by approximately an order of magnitude. Thus, even though the tip may consist of many points, only the one that is close to the sample will have significant tunneling. The typical spatial resolution is ~ 1Å in x and y directions (parallel to the surface) and less than 0.1 Å in z direction (perpendicular to the surface).

Once the tunneling current is established, then the tip is rastered over the surface to produce an 'image'. The rastering as well as the control of the tip-to-sample distance are provided by piezoelectric ceramics ('piezo' for short). These ferroelectric materials have the perosvkite crystal structure. Their asymmetric unit cells with an electrical dipole moment provides the slight change in the shape with applied potential. They lengthen in the direction of the field while contracting in the perpendicular direction. By combining different piezo ceramics, rastering (x, y control) and z control can be accomplished. A lead titanate-zirconate (Stavely EBL 3 PZT) piezoelectric ceramic tubes are used in our STM.

STM utilizes a feedback loop to control the tip-to-sample distance such that the tunneling current is constant to a set value (reference current). The schematics of the feedback loop is illustrated in Figure 3.2. The tunneling current is measured and compared with an externally controlled set point. The difference is sent to an electronic integrator which controls the z position of the tip. If the current is lower than the set-point, the tip is moved closer to the sample, and vise versa.

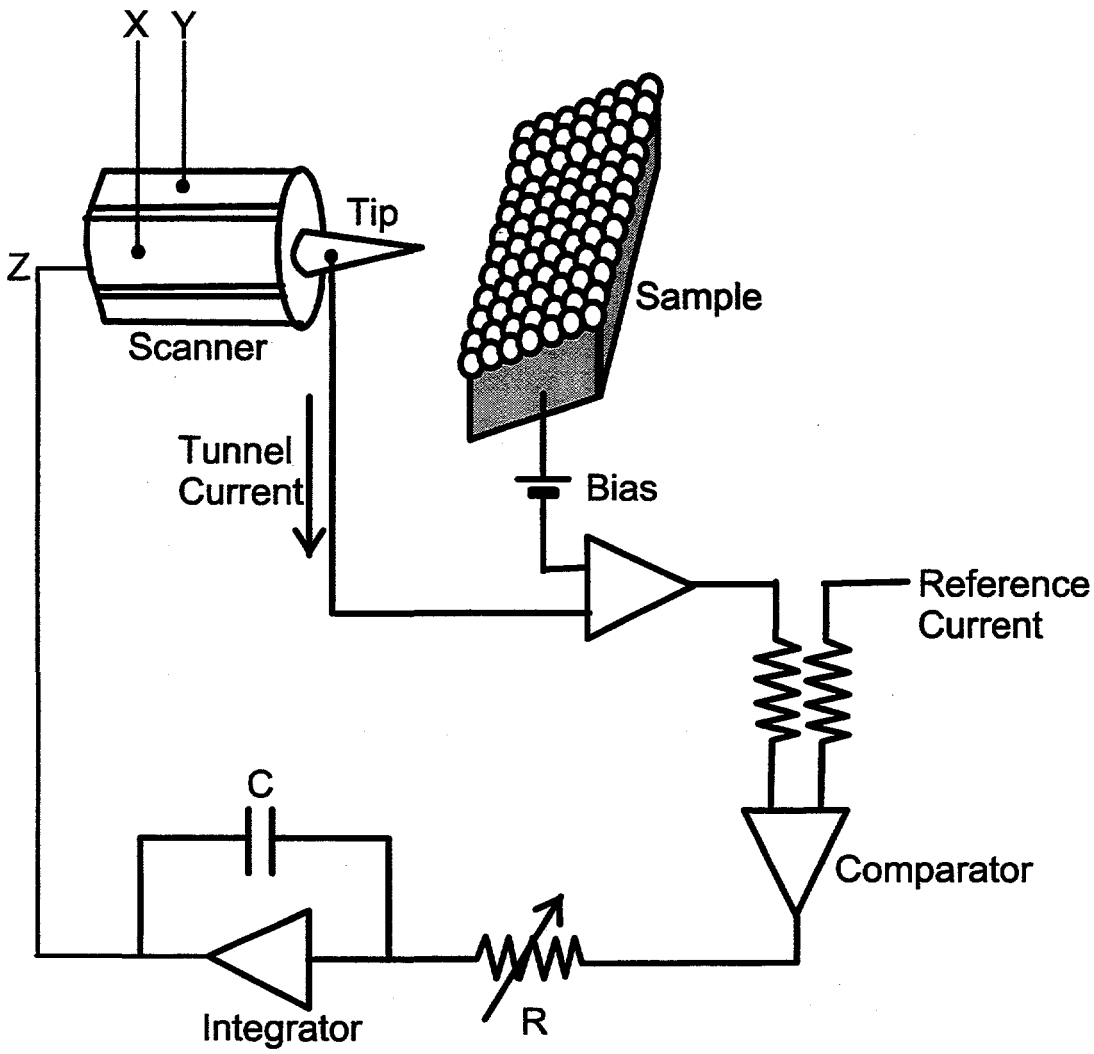

Figure 3.2 A schematic of the feedback loop operation. A feedback controls the tip-to-sample distance to maintain the tunneling current at the reference value.

An image is produced by rastering the tip over the surface while collecting data. Depending on the source of the data, several common modes of operation are available. In topographic mode, images are acquired by collecting the feedback loop output (voltage applied to piezo to move the tip in z direction) while the tip is scanned slowly so that the feedback loop can respond to the change in the tunneling current. A second common mode is 'current' mode. In current mode, images are made by recording the change in the tunneling current while tip is moved quickly over the surface. In this mode, the feedback loop is set to respond slower than the scanning rate. High scanning speed can be obtained with this mode compare to topographic mode, but it requires a very flat surface to prevent the tip from crashing into the surface. Another mode of imaging is 'barrier height' mode. It measures the rate of decay in the tunneling current when the tip-to-sample distance is modulated with small amplitude (< 0.1 Å) at a frequency above the cutoff frequency of the feedback loop. The measured signal can be related to the local surface workfunction. These three modes of operation are shown in Figure 3.3.

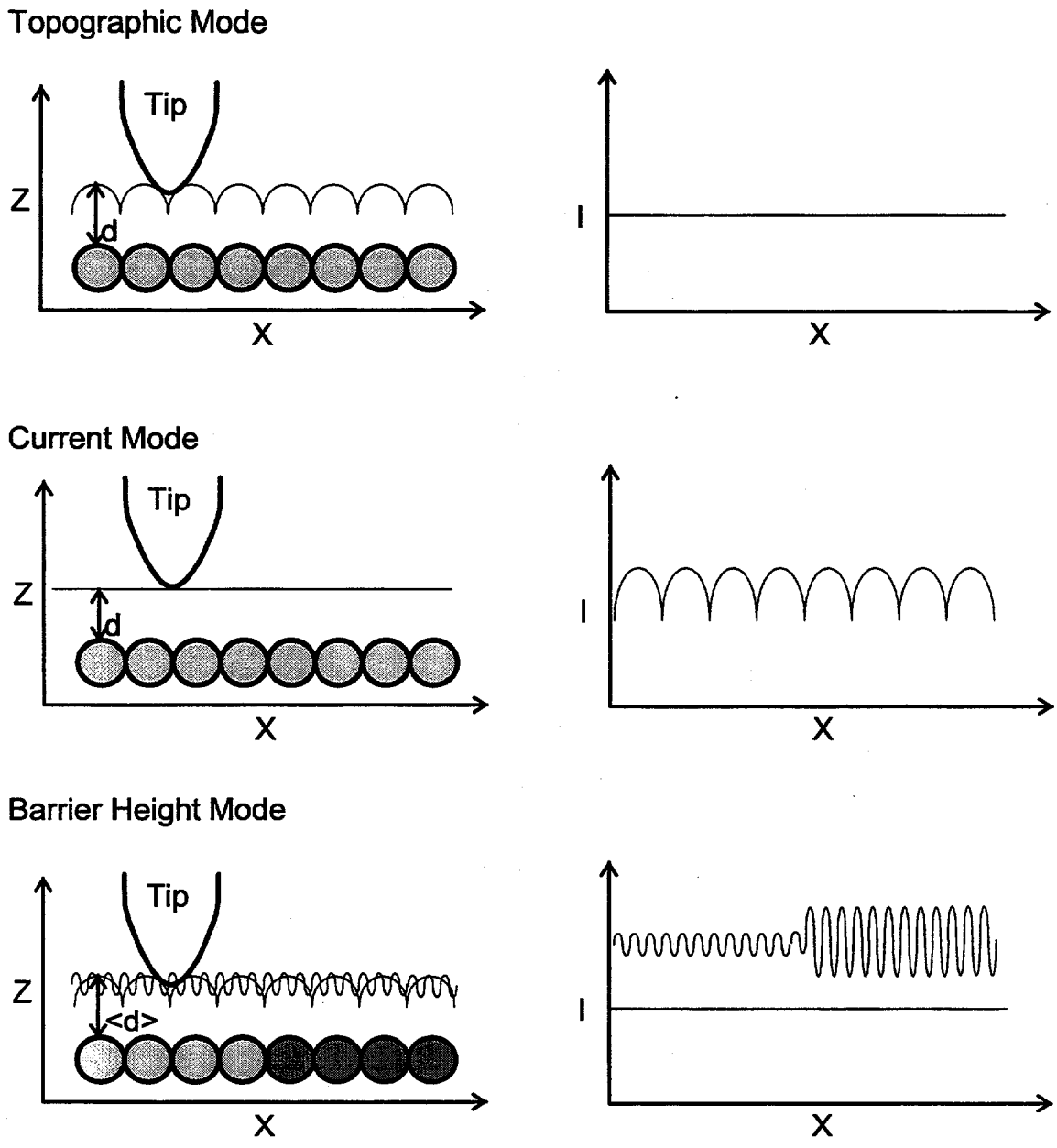

Figure 3.3 Three common modes of STM operation. In topographic mode the position of the tip in the *z* direction is recorded at a constant current value. In current mode, the tip is rastered at a certain height over the sample while the change in the tunneling current is recorded. The barrier height mode used the modulating the height of the tip and the response of the tunneling current is detected with the lock-in amplifier.

3.3 Ultrahigh Vacuum STM

3.3.1 STM Head

The microscope used for this dissertation is homemade based on the existing design and very similar to those in Ref. [19, 20]. The STM is mounted on an 8" flange. The STM head is "double tube" which consists of two concentrically mounted piezo tubes. The concentric design provides thermal compensation in x and y directions and reduces the thermal drift due to symmetry around its z axis. The outside electrode of tubes are sectored in quadrants to provide the control of position of each sector in three dimensions. Both tubes are soldered to a copper piezo holder. The outer piezo controls the coarse x and y positions as well as provides the sample approach. The inner piezo controls the scanning and the tip-to-sample distance. While the inside electrode of the inner piezo is ground, the inner electrode of the outer piezo is sectored to give independent z control. The STM head has been modified over the years to improve its performance. A big improvement was accomplished by changing the inner piezo to one with a smaller diameter and thinner wall. The field responses of these 1/8" tubes are about 200 Å in x and y directions and about 50 Å in the z direction. The tip is made out of 12 mil Pt-10% Rh thermocouple wire. These Pt/Rh wires provide stiffness as well as good resistant to oxide formation. At first, these wires are mechanically cut to provide a sharp tip, however this method was not reliable. Later, electrochemical etching was introduced to make a sharp tip. The tip is emerged in a molten solution of Nalco and $NaNO_3$, then the current is applied. Often inside the UHV chamber, the tip was cleaned

by 'pulsing' the bias voltage from ~ 1 to 10 V to remove some of the contaminants on the tip. The schematics of STM head is illustrated in Figure 3.4.

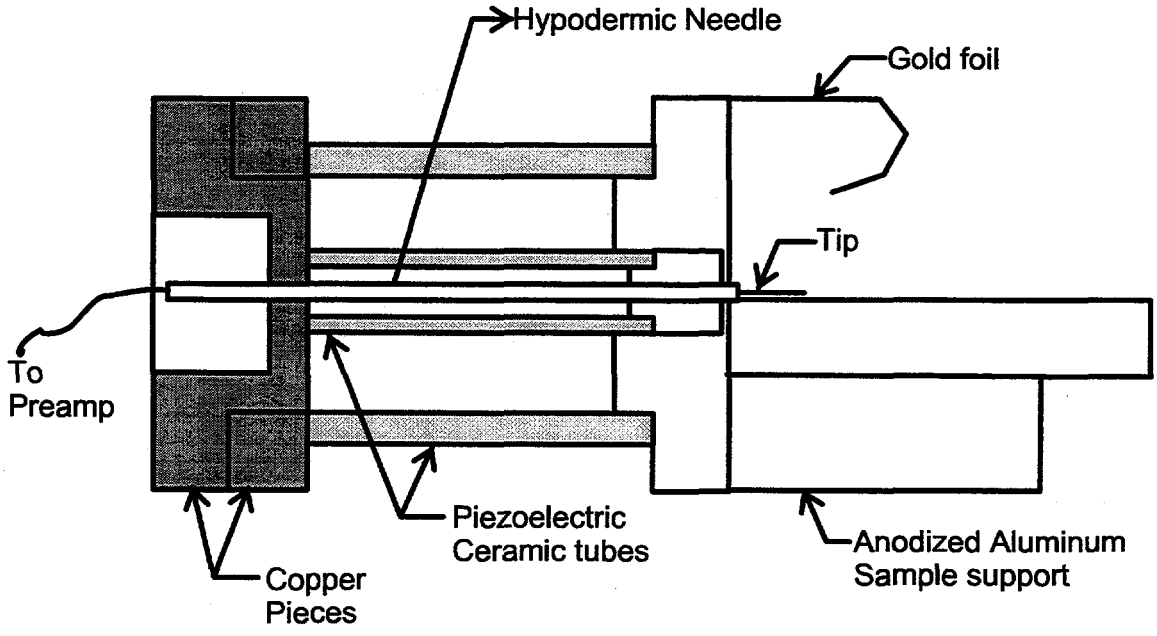

Figure 3.4 The cross-sectional schematics of the STM head. Two piezoelectric ceramics are soldered on the copper to provide the stiffness. The tip is held into the tip holder made out of Macor piece. Macor is glued to the end of inner piezo tube. The anodized aluminum rail is soldered to the end of the outer piezo. The sample holder block is resting on top of these rails during STM operation.

When the sample is cleaned, prepared and characterized, the sample holder is transferred from the manipulator. The sample holder is placed onto the rail made out of anodized aluminum. An inertial approach technique is used to produce the coarse and fine movements to bring the sample within the tunneling range. In this approach method, the sample is translated toward the tip by applying an asymmetric ramp waveform to the outer piezo tube causing the piezoelectric to change its length rapidly. This rapid change in length provides stick-slip motion of the sample holder block resulting in motion in one direction. The asymmetric ramp of opposite direction is applied for the sample retraction.

3.3.2 Vibration Isolation

In order to achieve stability for imaging, the vibration isolation is very crucial. Three vibrational isolations were employed in this STM. The STM head is mounted on a copper block which is then mounted on stacked plates separated by UHV compatible silicone elastomer. The bottom plate is held to the support arms of the flange by four springs. Viton cords are wound around these springs to provides additional damping. These vibration isolation decouples the microscope from acoustic noise and vibration above 20Hz. The schematic of the scanning tunneling microscope is illustrated in Figure 3.5 and the picture is shown in Figure 3.6. In addition to these isolation systems in the vacuum chamber, the entire UHV chamber is supported on air legs (Newport Laminar Flow Isolator) to decouple any building vibration above 1 ~ 2 Hz (see Figure 1.2(a)). During STM operation, all the unnecessary electronic cables are disconnected from the chamber to prevent them from conducting any vibrations.

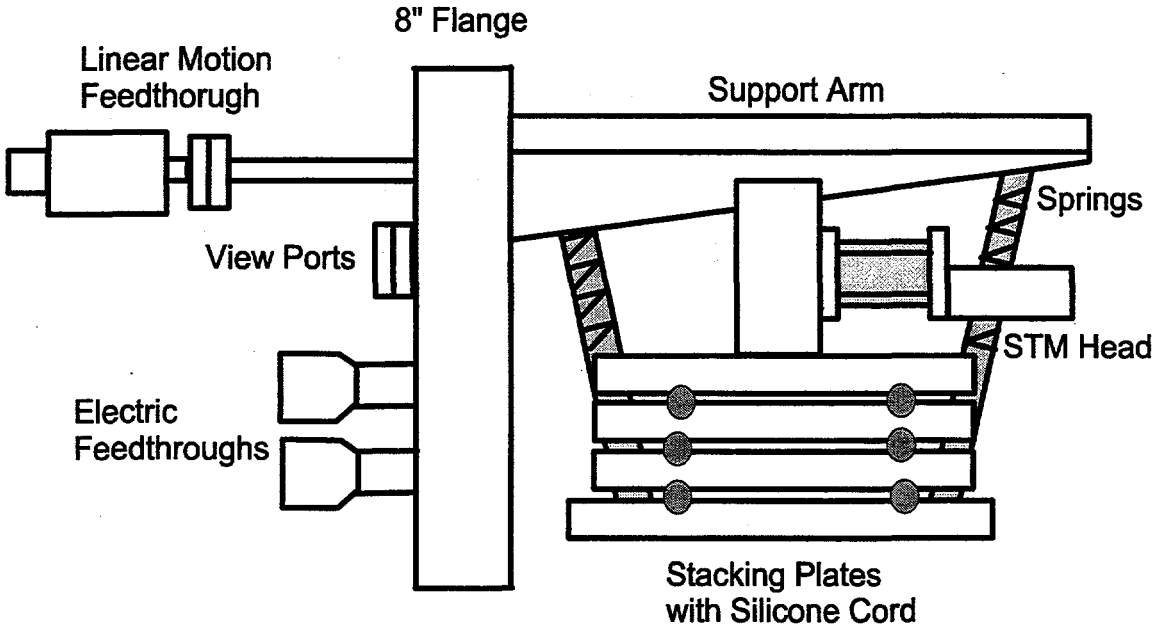

Figure 3.5 A schematic of the STM. The entire STM assembly is mounted on an 8" flange. The STM head is mounted on the copper block which is mounted on the stacking plates. These plates are separated by the silicone elastomers for vibration damping. The four springs hold the STM to the support arms. Viton is wound around the spring for additional damping.

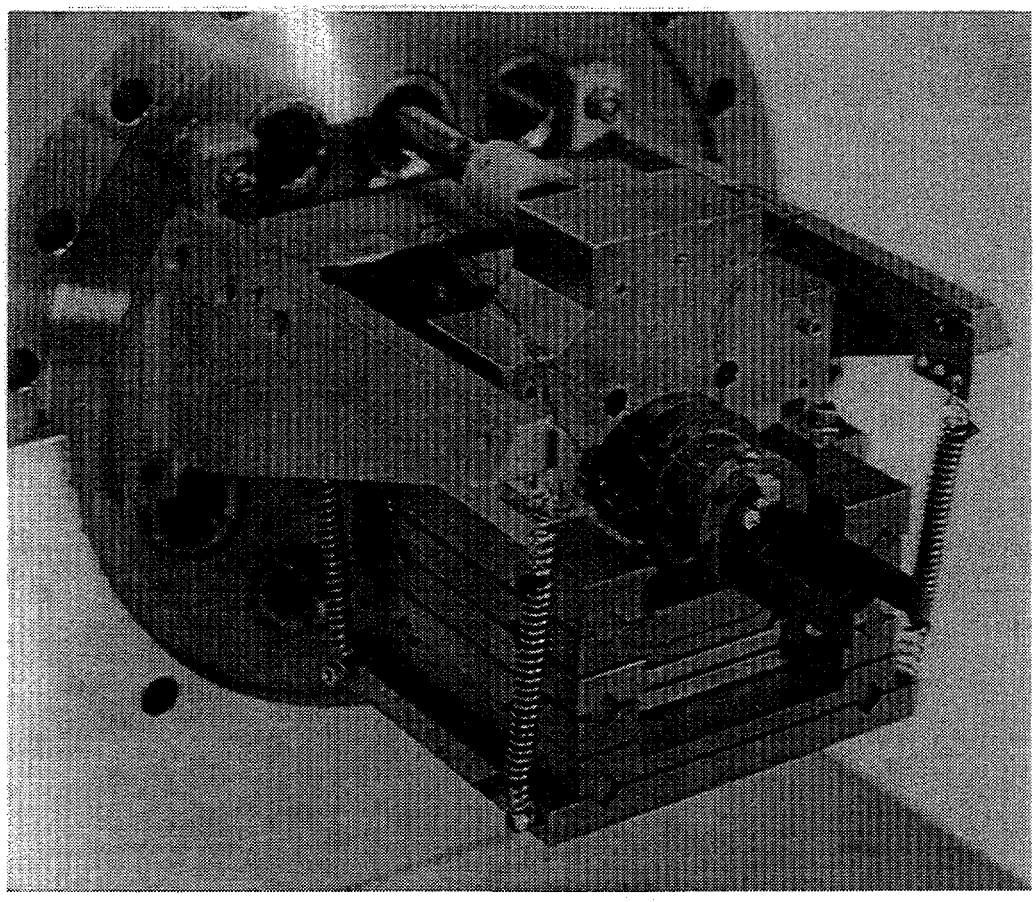

Figure 3.6 (a) A photograph (side view) of the STM. The STM head as well as the vibrational isolation components are shown including the stacking plates, silicone elastomer, and springs with Viton cord.

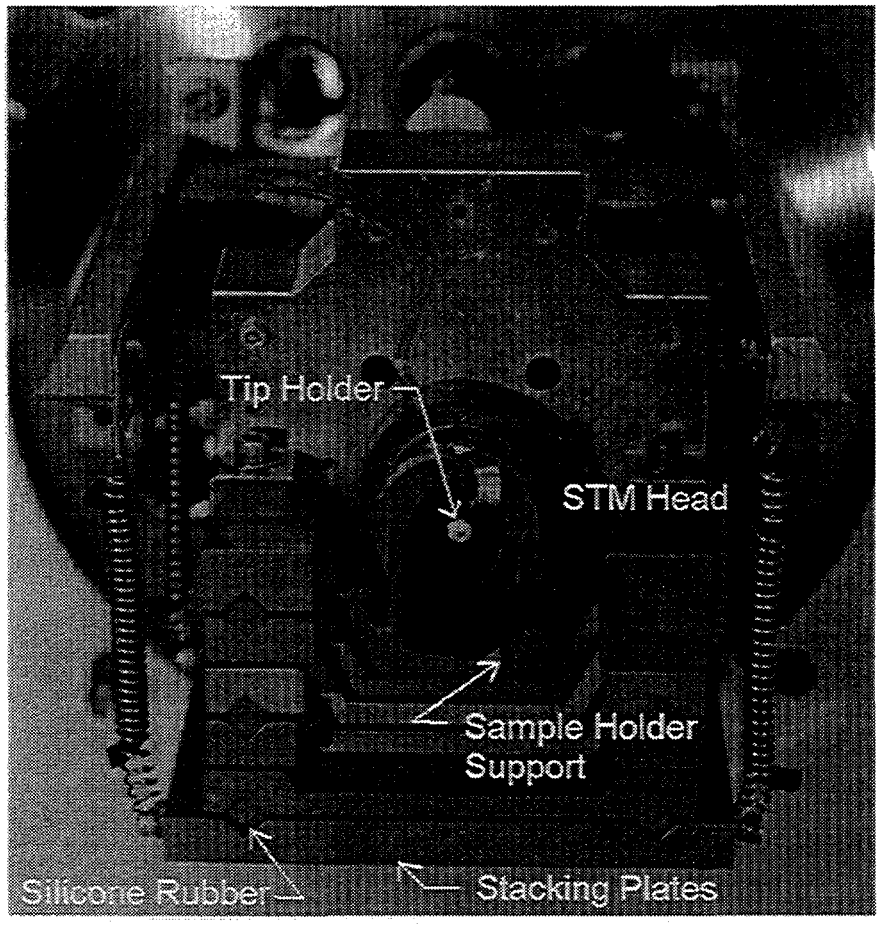

Figure 3.6 (b) A Front view photograph of STM. The tip holder (white cylinder) is visible. The vibrational isolation components are also shown including the stacking plates, silicone elastomer, and springs with Viton cord.

3.4 Electronics

The RHK STM 100 is used to control the microscope. It provides each electrodes with ± 130 V, a 260 V swing. Scans are always concentric around 0 V. This minimizes cross talk between x, y and z sectors and reduces piezo creep. Scan area is set by adjusting the voltage to the inner piezo tubes. It is interfaced with computer through Data Translation board. The coarse positioning, as well as the scanning size can be controlled externally while the rastering of the inner piezo (scanning of the tip) is controlled by the on-board computer. STiMage386 software is used to acquire images, spectroscopy and data processing.

3.5 Initial Testing

After having built the microscope, the performance of the microscope was tested with a Highly Oriented Pyrolytic Graphite (HOPG) and Au(111) surface. The scanner (inner piezo) was calibrated with these samples since the structural parameters of these materials are already known. A current image of HOPG was obtained with atomic resolution. The image was compared with the known lattice parameter of graphite to calibrate the piezo in x and y directions as shown in Figure 3.7. The topographic image of the Au film shows the terraces separated by the monoatomic height steps. The height of these steps are also know to be 2.7 Å. The scanning piezo was calibrated in the z direction with images like Figure 3.8 shown below.

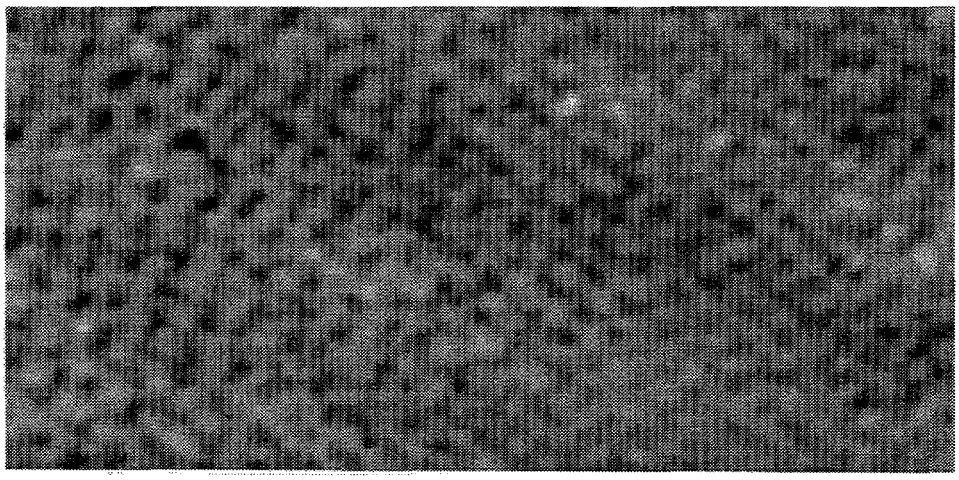

Figure 3.7 Current image of graphite taken at 1 nA and 100 mV in ambient conditions. The lattice spacing of graphite is used to calibrate the piezo ceramics.

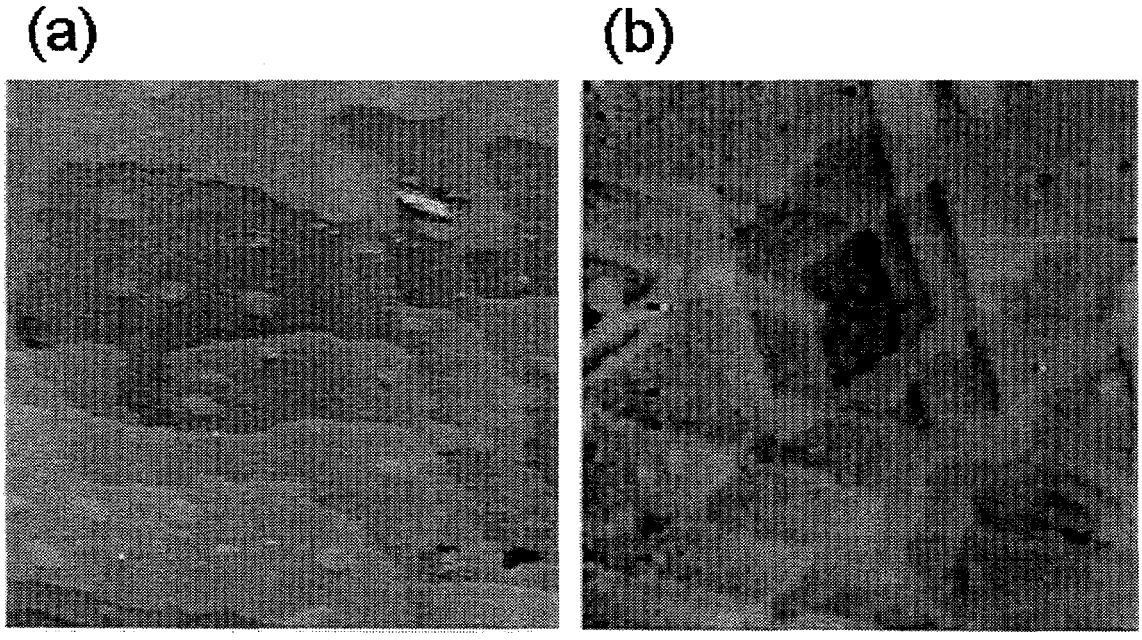

Figure 3.8 Topographic images of a gold thin film deposited on mica. (1000 Å x 1000 Å). Typically the images of a gold thin film show many steps with islands.

3.6 Image of clean metal surface in UHV

Once, the STM is in vacuum chamber, also the piezo can be calibrated with a clean metal surface. The calibration in z direction with clean metal is relatively easy since the height of single atomic height steps are ~ 2 Å. Figure 3.9 shows a couple of topographic images of a clean Rh(111) surface. Sometimes a very large terrace can be seen as well as some screw dislocations on the surface as shown in Figure 3.9 (a), but most of the time, the surface has a series of monoatomic height steps separated by 150 to 200 Å as shown in Figure 3.9 (b).

The calibration in the x and y directions is more difficult due to the small corrugation of the metal atoms on the surface. However, in some cases, the metal atoms can be imaged and be used to calibrate the piezo ceramics. Figure 3.10 (a) shows a topographic image of a clean Rh(111) surface showing atomic resolution. Figure 3.10 (b) is the line scan of A-A' showing the spacing between these atoms is about 2.7 Å, and the average corrugation is about 0.1 Å

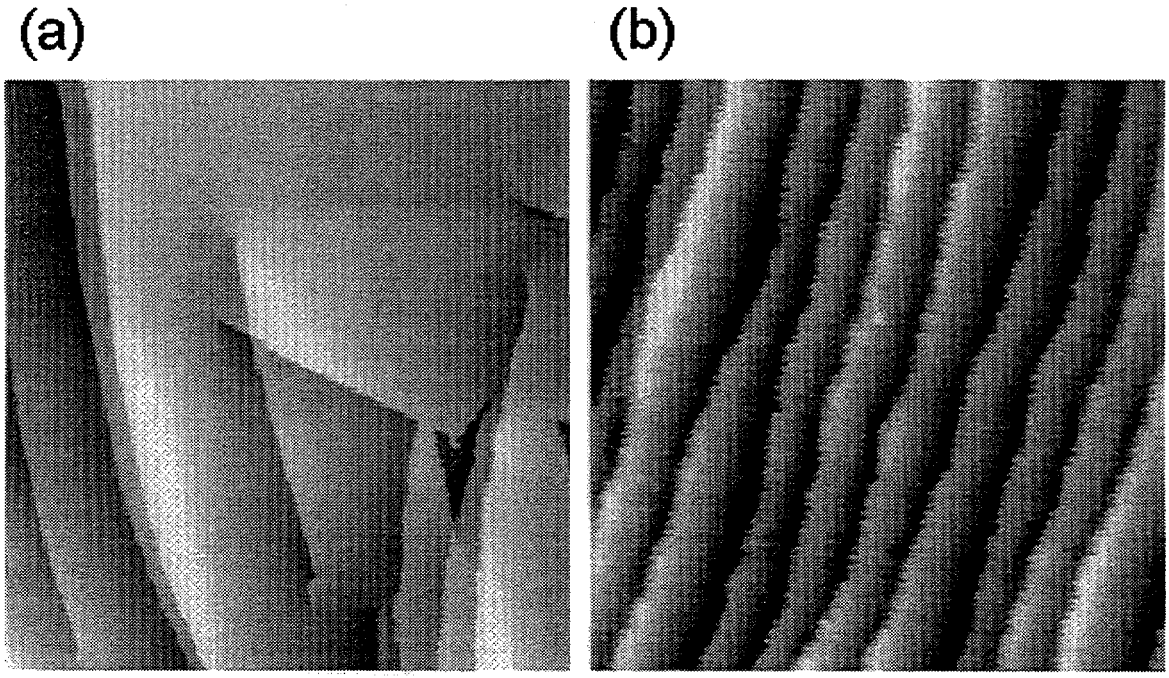

Figure 3.9 Topographic image of clean Rh(111) surface. (a) 1000 Å x 1000 Å image shows very large terrace with many screw dislocations on the surface. (b) 1500 Å x 1500 Å image shows a series of steps separated by about 150 Å.

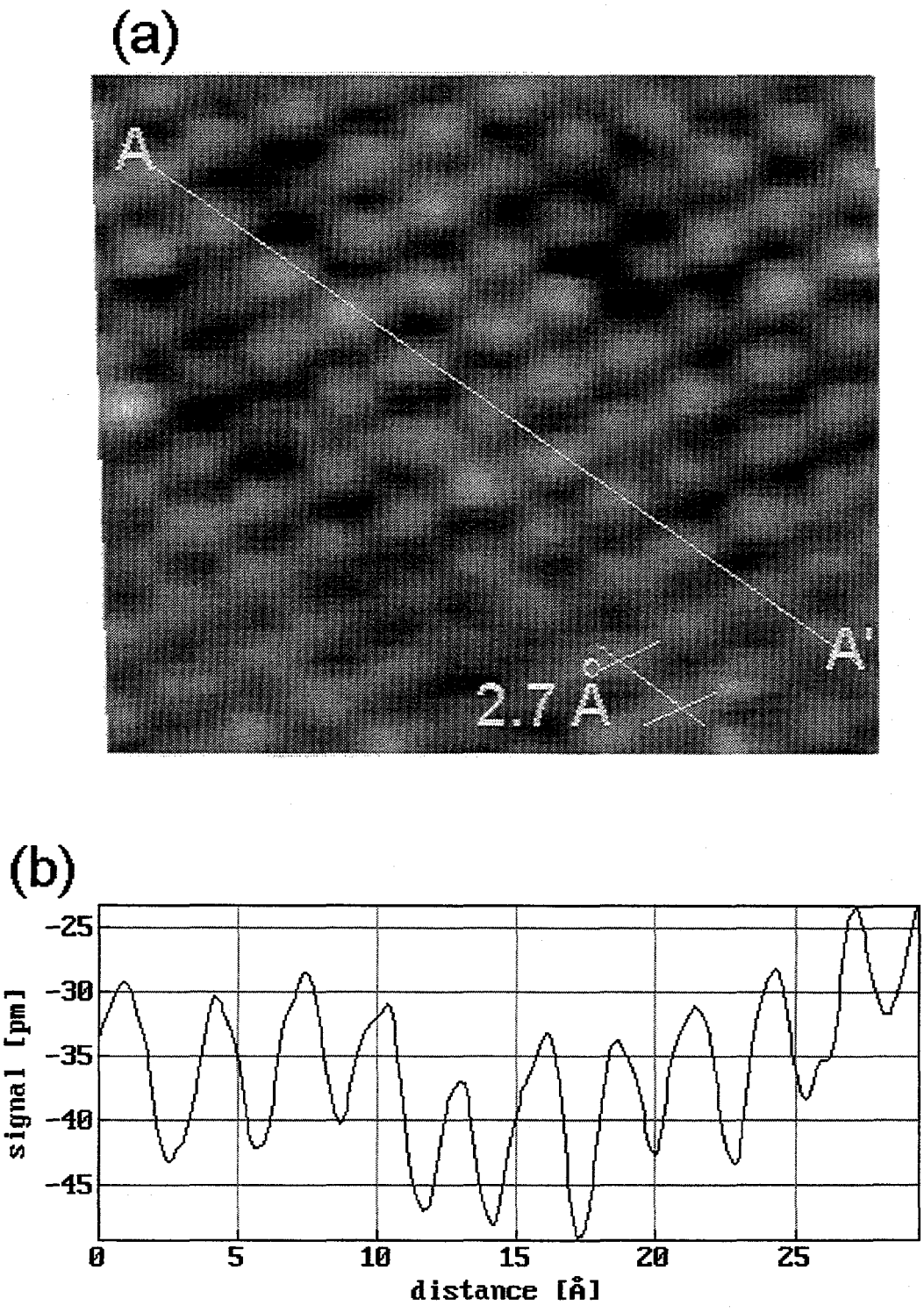

Figure 3.10 A topographic image of clean Rh(111) surface showing rhodium atoms. The distance between these atoms are 2.7 Å. An averaged corrugation of atoms is 0.1 Å as shown in (b).

Chapter 3 References

1. G. Binnig, H. Rohrer, C. Gerber, and E. Wiebel, Phys. Rev. Lett., 1982. **49**: p. 57.
2. G. Binnig, H. Rohrer, C. Gerber, and E. Wiebel, Appl. Phys. Lett., 1982. **40**: p. 178.
3. G. Binnig, H. Rohrer, C. Gerber, and E. Wiebel, Phys. Rev. Lett., 1983. **50**: p. 120.
4. R. Wiesendanger and H.-J. Güntherodt, eds. *Scanning Tunneling Microscopy III.* 1993, Springer-Verlag: Berlin.
5. M. Salmeron, *Scanning tunneling microscopy*, in *Emerging Techniques for Catalyst Characterization*, J. Horsley, Editor. 1989, Catalica, Inc.: Mountain View.
6. H.-J. Güntherodt and R. Wiesendanger, eds. *Scanning Tunneling Microscopy I.* 1992, Springer-Verlag: Berlin.
7. J.A. Golovchenko, Science, 1986. **232**: p. 48.
8. D. Bürgler, G. Tarrach, T. Schaub, R. Wiesendanger, and H.-J. Güntherodt, Phys. Rev. B, 1993. **47**: p. 9963.
9. J.C. Dunphy, P. Sautet, D.F. Ogletree, and M.B. Salmeron, J. Vac. Sci. Technol. A, 1993. **11**: p. 1975.
10. D. Heuer, T. Müller, H. Pfnür, and U. Kohler, Surf. Sci., 1993. **297**: p. L61.
11. J.C. Dunphy, P. Sautet, D.F. Ogletree, O. Dabbousi, and M.B. Salmeron, Phys. Rev. B, 1993. **47**: p. 2320.
12. S. Chiang, R.J. Wilson, C.M. Mate, and H. Ohtani, J. Microsc., 1988. **152**: p. 567.

13. S. Chiang, R.J. Wilson, C.M. Mate, and H. Ohtani, Vacuum, 1990. **41**: p. 118.

14. H. Ohtani, R.J. Wilson, S. Chiang, and C.M. Mate, Phys. Rev. Lett., 1988. **60**: p. 2398.

15. P. Sautet and C. Joachim, Chem. Phys. Lett., 1991. **185**: p. 23.

16. P. Sautet, J. Dunphy, D.F. Ogletree, and M. Salmeron, Surf. Sci., 1993. **295**: p. 347.

17. P. Sautet, J.C. Dunphy, D.F. Ogletree, C. Joachim, and M. Salmeron, Surf. Sci., 1994. **315**: p. 127.

18. P. Sautet and M.-L. Bocquet, Surf. Sci. Lett., 1994. **304**: p. L445.

19. J.W. Lyding, S. Skala, R. Brockenbrough, J.S. Hubacek, and G. Gammie, J. Microsc., 1988. **152**: p. 371.

20. D.M. Zeglinski, D.F. Ogletree, T.P. Beede, R.Q. Hwang, and M. Salmeron, Review of Scientific Instruments, 1990. **61**: p. 3769.

Chapter 4

Low Energy Electron Diffraction (LEED)

4.1 Introduction

Low Energy Electron Diffraction (LEED) involves scattering of electrons elastically off a surface to generate a diffraction pattern. Because electrons have wave-like properties, the electron has a wavelength between 2.7 and 0.7 Angstroms at energies between 20 and 300 eV as given by the de Broglie relationship.

$$\lambda = \frac{h}{\sqrt{2mE}} \tag{4.1}$$

Because this wavelength is of the same order as a typical lattice constant, a Monoenergetic beam of electrons will diffract from an ordered surface, analogous to X-ray diffraction. The low energy electrons have a small mean free path of only a few atomic layers between 40 and 100 eV as measured for many materials and the resulting curves then to follow a 'universal curve' [1]. The small mean free path of electrons to a few atomic layers give LEED surface sensitivity. Besides the difference in surface sensitivity, electrons strongly interact with the surface resulting in multiple scattering.

4.2 Basic Principles

The LEED pattern formed is related to the 2D surface unit cell as the X-ray diffraction pattern is to the 3D unit cell of a crystal. The LEED pattern is a projection in reciprocal space of the real space 2D unit cell. The quantum mechanical wave-like properties of electrons combined with the translational symmetry of the substrate restricts momentum transfer to values that are integer multiples of a reciprocal lattice vector [2]. The LEED scattering process is illustrated in Figure 4.1. The electrons first pass through a hole in the detector and strike the sample with a certain $k_{\perp}$ and $k_{\parallel}$. The electrons are scattered with their parallel momentum changed by integer multiples of a reciprocal lattice vector of the substrate. The elastically back scattered electrons then travel back to the detector forming a LEED pattern.

A one dimensional infinite line of scatterers are considered to understand the diffraction process, as shown in Figure 4.2. In this figure, a plane-wave is scattered off a 1D lattice with a periodicity of d. Each atom scatters the incident wave into spherical waves, which merges into outgoing plane waves. Only the waves with constructive interference will be out going, thus the path difference between waves generated by each scatterer must be an integer multiple of the electron's wavelength. The path length difference between scattering events at two adjacent lattice point must be equal to $n\lambda$. The following equation can be derived from the Figure 4.2.

$$d\,(\sin\phi_f - \sin\phi_o) = n\lambda \qquad (4.2)$$

In the two dimensional case, scattering takes place in a plane rather than a line.

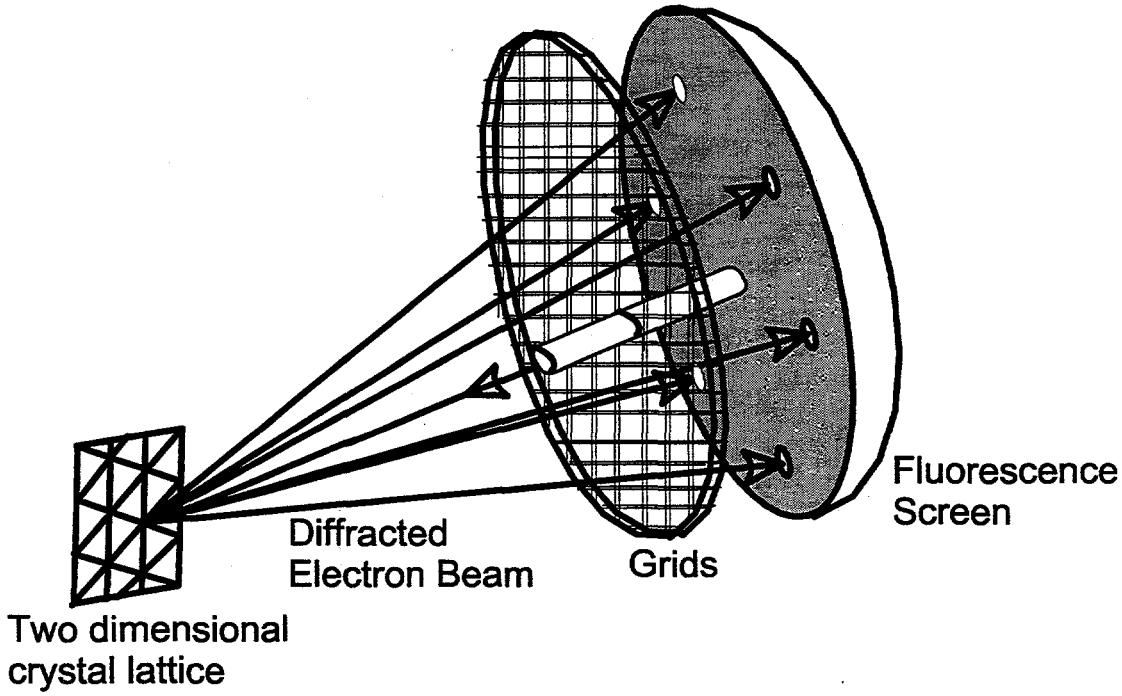

Figure 4.1 A simple representation of the scattering process in the LEED experiment. Monoenergetic electrons generated in the e-gun are scattered off the lattice of the crystal. Only the elastically scattered electrons will pass through the grids to hit the fluorescence screen on which the impact position is recorded. The arrows represent the possible paths of electrons.

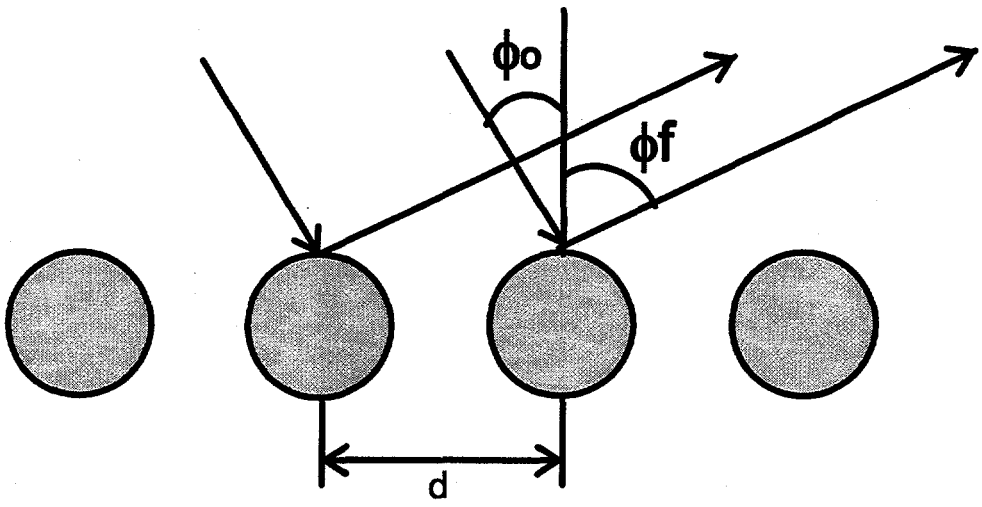

Figure 4.2 Scattering of an electron plane wave off a one dimensional lattice. ϕ_o and ϕ_f are the incident and scattered angles plane waves respectively. *d* is the lattice spacing.

Reciprocal lattice vectors, $\vec{b}_1$ and $\vec{b}_2$, are determined from the real space lattice vectors, $\vec{a}_1$ and $\vec{a}_2$, by the following relationship:

$$\vec{a}_i \bullet \vec{b}_j = 2\pi\delta_{ij} \qquad (i, j = 1, 2) \tag{4.3}$$

where δ_{ij} is the Kronecker delta function. In order to have constructive interference between the incoming and outgoing waves, the parallel component of an elastically scattered electron's momentum can only change by integer multiples of a reciprocal lattice vector [3]. The restriction for the parallel momentum transfer can be obtained as follows.

$$\Delta\vec{k}_{\parallel} = n_1\vec{b}_1 + n_2\vec{b}_2 \tag{4.4}$$

$\Delta\vec{k}_{\parallel}$ is the change in parallel momentum transfer, n_1 and n_2 are integers. In an elastic process, the total energy of the incoming electron must be equal to the total energy of the outgoing electron. Thus, the perpendicular component of the electron's momentum must be:

$$\vec{k}_{\perp} = \sqrt{\vec{k}^2 - \vec{k}^2_{\text{initial}} - \Delta\vec{k}^2_{\parallel}} \tag{4.5}$$

Each spot in a LEED pattern can be associated with values of b_1 and b_2 such that the perpendicular component of the electron' momentum, $\vec{k}_{\perp}$ is real. The direction of the back scattered electron is determined by Equation 4.4. Two Laue conditions for LEED are:

$$\vec{a}_1 \bullet (\vec{k}_{backscattered} - \vec{k}_{initial}) = 2\pi n_1 \tag{4.6a}$$

$$\vec{a}_2 \bullet (\vec{k}_{backscattered} - \vec{k}_{initial}) = 2\pi n_2 \tag{4.6a}$$

due to the loss of translational symmetry perpendicular to the surface. Figure 4.3 illustrates both the surface and the resulting diffraction pattern at normal incident ($\vec{k}_{\parallel initial} = 0$) for an fcc(111)-(1x1) crystal face. The labels of the diffraction spots correspond to the n_1 and n_2 of Equation 4.4.

The formation of a typical ordered overlayer generates additional spots in the diffraction pattern. The overlayer reciprocal lattice vectors are smaller than those of substrate. Figure 4.4 shows a (2x2) overlayer on an fcc(111) surface. Because the real space unit vectors for the overlayer are tow times that of the substrate, the additional spots appear at 'half-order' positions with respect to the substrate spots.

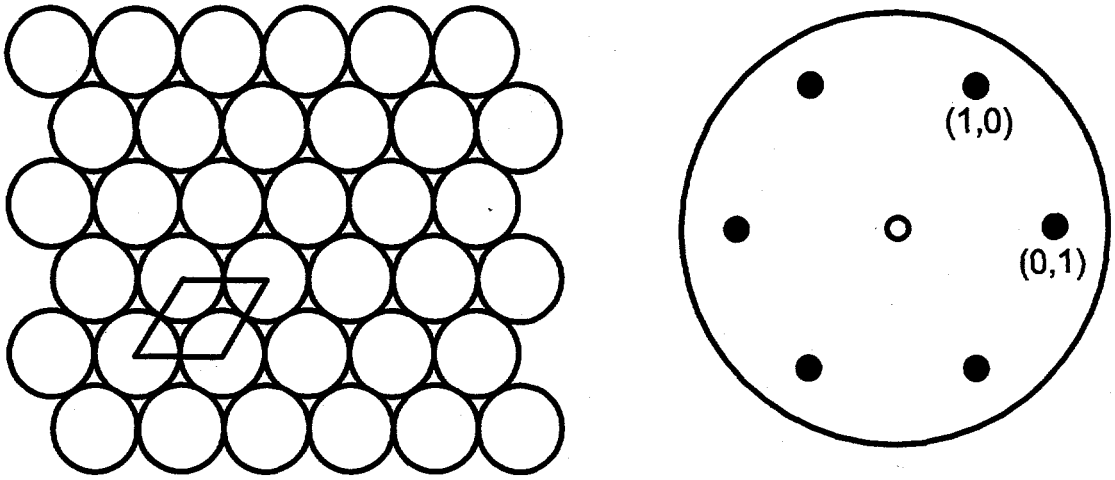

Surface Diffraction Pattern

Figure 4.3 An illustration of the real space lattice and its diffraction pattern (at normal incidence) of an fcc(111)-(1x1) surface. The labels of the diffraction spots correspond to the n_1 and n_2 described in text.

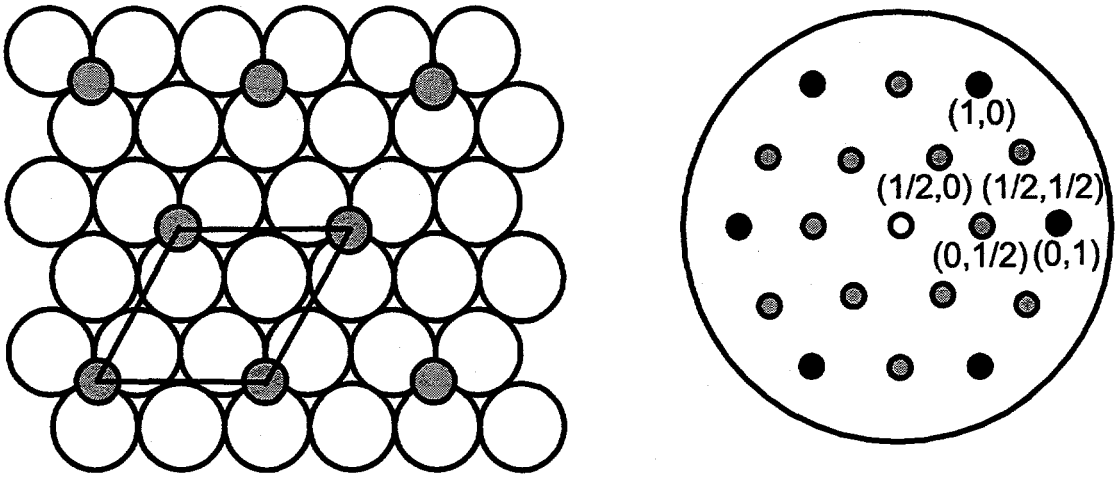

Surface Diffraction Pattern

Figure 4.4 An illustration of the real space lattice and its diffraction pattern of an fcc(111)-(2x2) surface. The labels of the diffraction spots correspond to the n_1 and n_2 described in text.

4.3 Experiments

Varian 4-grid LEED optics with an off-axis electron gun was used in the studies for this dissertation. The first grid is grounded to have a field-free region between the sample and LEED optics. On the second and third grid, the voltage is applied so that only the elastically scattered electrons would be accelerated toward to the screen. The screen lies directly behind the grids. The screen is coated with P-11, and biased up to 6 kV. The brightness of the beam generated on the screen is proportional to the number of electron impacts [4, 5].

A video camera was used to capture the LEED pattern as a function of incident electron beam energy. In this case, all k space can be recorded simultaneously reducing the time required to get whole sets of I-V curves, thus minimize possible electron beam damage to the surface. A Dage-MIT SIT-68 high sensitivity video camera was used to produced the video signal which was then digitized. The video output of the camera is connected to a Matrox MVP-AP video digitizer. Data collection normally requires the averaging of 128 images. The typical Video LEED experimental setup is illustrated in Figure 4.5.

Once these images were recorded, further analysis can be performed with 'Intensity vs. Voltage' (I-V) curves. The I-V curves are generated by calculating the integrated intensity of the diffraction beams at each energy of incident electron beam. The resulting I-V curves can be used as the basis for the Tensor LEED (TLEED) calculation to determine the structure of the surface [6]. The tensor LEED analysis will be discussed in the next section.

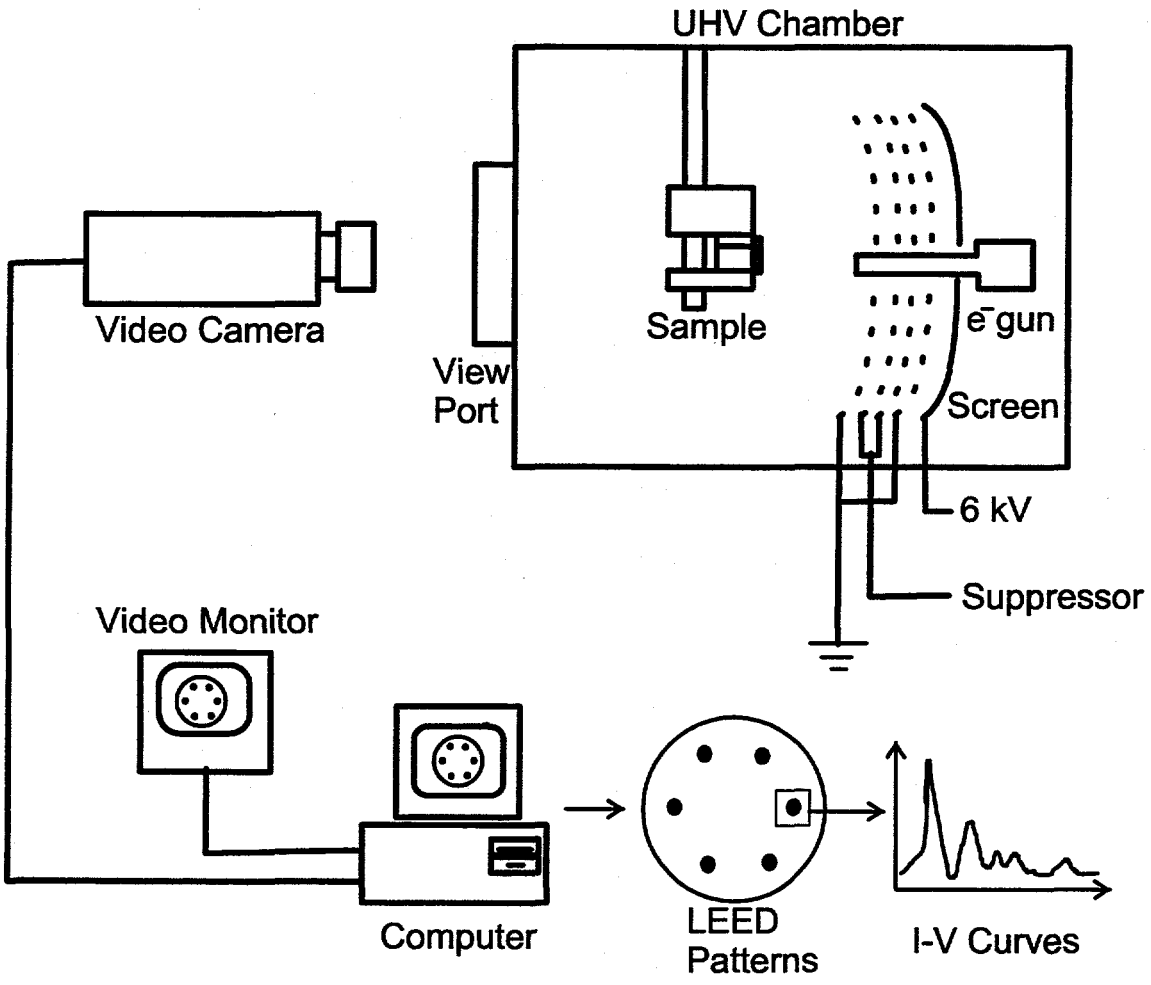

Figure 4.5 A schematic of Video LEED (VLEED) experimental setup. LEED patterns are recorded by the video camera, digitized, then stored in the computer. The I-V curves are generated by integrating the intensity of each diffraction beam at each incident electron beam energy. The resulting I-V curves can be used as the basis for the structural analysis.

4.4 Structural Analysis

The structural analysis for LEED is based on a trial and error procedure. This procedure including theories is described in detail in Reference [3, 7]. Only a simplified description will be discussed in this section. Figure 4.6 is a flow-chart representing the procedure to find the surface structure. First, the 'model' structure is made. The multiple scattering of electron prevents the direct inversion of the experimental data to the geometrical positions of the surface atoms. Full dynamic LEED calculation is then carried out with a model structure (reference structure). The resulting I-V curves are compared with the experimental I-V curves. The 'Reliability factor' (R-factor) is used to judge how well the theoretical I-V curves fit with the experimental ones [8]. The R_p-factor (Pendry's R-factor) is used in this study and it is designed to have high sensitivity to structural information and low sensitivity to non-structural parameters. When the theoretical I-V curves do not fit well with experiment, modification of the model structure is necessary. The tensor LEED (TLEED) approximation is used for the refinement of a model structure [7]. For a small displacement the change in the amplitude of diffracted beams can be treated using first order perturbation theory. The TLEED approximation allows one to quickly compute the change in intensity of a diffracted beam for a structure in which the positions of atoms have been displaced by a small amount with respect to a reference structure. This TLEED approximation can be combined with the 'Automated Search' algorithm to obtain the best-fit structure [6]. However, full dynamic LEED calculation must be carried out for models with large difference in structure, i.e. different

adsorption site, since TLEED approximation fails for displacement larger than 0.2 to 0.4 Å. When a model gives the lowest R_p-factor then the model is taken as the structure.

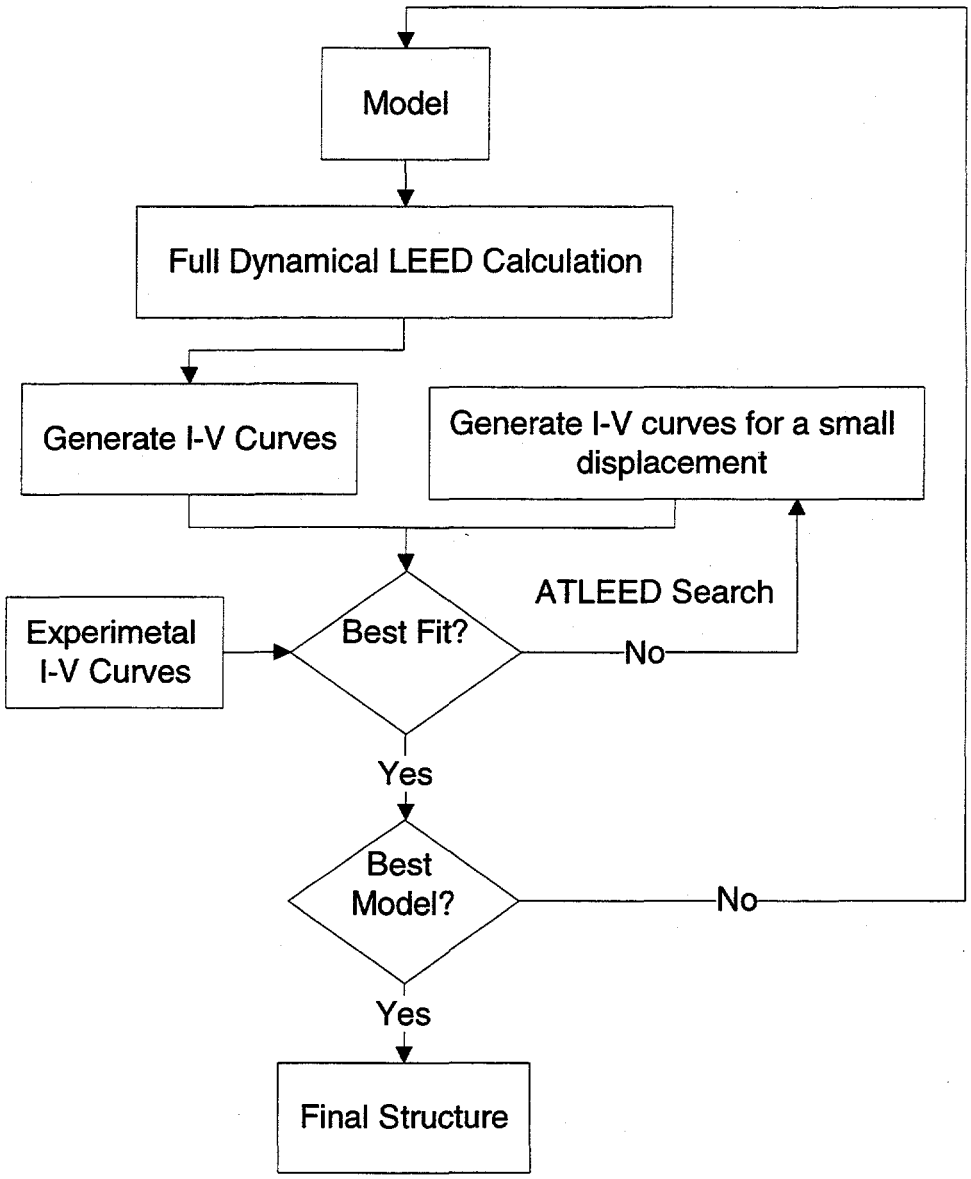

Figure 4.6 A Flow-chart of steps in a LEED structure determination. The outer loop represents a coarse search over different models (i.e. adsorption sites), and the inner loop is the automated TLEED search for the refinement of each model.

Chapter 4 References

1. G.A. Somorjai, *Chemistry in Two Dimensions: Surfaces.* 1981, Ithaca, NY: Cornell University Press.
2. J.B. Pendry, *Low Energy Electron Diffraction.* 1974, London: Academic Press.
3. M.A. Van Hove, W.H. Weinberg, and C.-M. Chan, *Low Energy Electron Diffraction.* 1986, Berlin, Heidelberg, New York: Springer-Verlag.
4. D.P. Woodruff and T.A. Delchar, *Modern techniques of surface science.* 1986, Cambridge: Cambridge University Press.
5. G. Ertl and J. Küppers, *Low Energy Electrons and Surface Chemistry.* 1974, Weinheim: Verlag Chemie.
6. M.A. Van Hove, W. Moritz, H. Over, P.J. Rous, A. Wander, A. Barbieri, N. Materer, U. Starke, D. Jentz, J.M. Powers, G. Held, and G.A. Somorjai, Surf. Sci. Rep., 1993. **19**: p. 191.
7. P.J. Rous and J.B. Pendry, Surf. Sci., 1989. **219**: p. 355.
8. J.B. Pendry, J. Phys. C, 1980. **13**: p. 937.

Chapter 5

Adsorbate Induced Surface Relaxation;

LEED Studies of Sulfur on Pt(111)

5.1 Introduction

Sulfur adsorption on metal substrates has been the subject of numerous studies due to the formation of a relatively large number of stable ordered overlayers as the adsorbate coverage is altered [1]. The possibility of many different ordered overlayers on a given metal surface suggests a delicate balance of forces between the adsorbates and between the adsorbate and the metal surface. Many surface structures have been determined by LEED in considerable detail [2].

On fcc (111) and hcp (0001) metal surfaces, sulfur forms from simple (2x2) and ($\sqrt{3}$x$\sqrt{3}$) R30^{o} to more complex structures such as c(4x2), (2$\sqrt{3}$x2$\sqrt{3}$) R30^{o}and ($\sqrt{7}$x$\sqrt{7}$) R19.1^{o}. These results are summarized in Table 5.1.

Table 5.1 Summary of Structures of sulfur adsorbed on fcc(111) and hcp(0001) surfaces

	Structure		LEED/ SEXAFS	STM
Ag (111)	(4x4)	[3]		
	$\begin{pmatrix} 3 & 2 \\ \bar{2} & 1 \end{pmatrix}$	[3]		
Ir (111)	(√3x√3)R30°		[4]	
Cu(111)	(√3x√3)R30°	[5]		
	$\begin{pmatrix} 3 & 1 \\ \bar{2} & 5 \end{pmatrix}$			[6]
	(√7x√7)R19°	[7]	[8]	[6]
Mo (111)	c(4x2)	[9]		
Ni (111)	(2x2)	[10]	[11]	
	(√3x√3)R30°	[10]		
	(5x5)	[10]		
	(5√3x2)	[12]		[13]
	(8√3x2)	[10]		
Pd (111)	(√3x√3)R30°		[14]	[15]
	(√7x√7)R19°			[15]
	(3x3)	[16]		
Pt (111)	(2x2)	[17, 18]		This work
	(√3x√3)R30°	[17, 18]	[19, 20]	This work
	$\begin{pmatrix} 4 & \bar{1} \\ \bar{1} & 2 \end{pmatrix}$	[17, 18]		This work
Re (0001)	(2x2)	[21]	[22]	[23]
	(2√3x2√3)R30°-6S	[21]	[22]	[23]
	c(√3x5)rect			[23]
	(3√3x3√3)R30°			[23]
	$\begin{pmatrix} 3 & 1 \\ 1 & 3 \end{pmatrix}$			[23]
Rh (111)	c(2x4)	[24]	[25]	[26]
	(√3x√3)R30°	[24]	[25]	[26]
	(4x4)	[24]		[26]
	(7x7)	[24]		[26]
Ru (0001)	(2x2)	[27, 28]	[29]	[30]
	(√3x√3)R30°	[27, 28]	[29]	[30]
	c(4x2)	[27, 28]		
	(7,0,3,6)	[28]		
	(√7x√7)R19°	[28]		

All orderings are detected by LEED, and some structures are determined by LEED analysis. In low coverage structures, such as in (2x2) and ($\sqrt{3}$x$\sqrt{3}$)R30^{o}, the general trend is toward sulfur occupying high symmetry adsorption sites, notably the fcc site on fcc metals and the hcp adsorption site on hcp metals.

The coverage of sulfur on Pt(111) has been investigated by both Auger electron spectroscopy (AES) [18] and radiotracers (S^{35}) [17]. In the work of Heegemann et al., three ordered LEED patterns were observed at approximately 0.25, 0.33 and 0.43 monolayers (ML) [18]. The lowest coverage structure is a (2x2) and that of the next higher is ($\sqrt{3}$x$\sqrt{3}$)R30°. Above 0.33 ML, a $\begin{pmatrix} 4 & \bar{1} \\ \bar{1} & 2 \end{pmatrix}$ = c(7x$\sqrt{3}$)rect pattern is formed; this last notation will be used. In addition, the ($\sqrt{3}$x$\sqrt{3}$)R30° structure of sulfur on Pt(111) has been studied by Hayek et al. using LEED I-V curve analysis [19, 20]. They find adsorption in the fcc-hollow site and a Pt-S distance of 2.27 Å corresponding to a sulfur height of 1.61 Å above the metal surface. These authors did not investigate the possibility of adsorbate-induced relaxations in the substrate.

Despite all these previous studies, no detailed structural analysis has been performed for the low-coverage (2x2) and high-coverage c(7x$\sqrt{3}$)rect overlayers. In this study, we carried out LEED analysis to determine the adsorption structure and adsorbate-induced relaxations of the substrate for the (2x2) and ($\sqrt{3}$x$\sqrt{3}$)R30° sulfur overlayers on Pt(111).

5.2 Experiments

Our experiments were carried out in a stainless steel ultrahigh vacuum (UHV) chamber as described in Chapter 2. The sample was cleaned by repeated cycles of argon ion bombardment (0.5 to 1.0 keV at $P_{Ar} = 5x10^{-5}$ torr) and annealing in oxygen (500 to 700 K at $P_{Oxygen} = 5x10^{-8}$ torr) and in vacuum until no impurities could be detected by AES, and the LEED pattern of the clean surface was sharp and free of diffuse background intensities.

A Dage-MTI SIT-68 high-sensitivity video camera interfaced with a PC was used to digitize the LEED pattern on the phosphorus screen. I-V curves were generated by computing the integrated intensity of each individual diffraction spot over a range of energies. Data acquisition was performed at 90 K and normal incidence was confirmed by comparing I-V curves of symmetrically equivalent beams.

A solid-state electrochemical source (Pt/Ag/AgI/AgS/Pt) was utilized for sulfur deposition [31]. Sulfur was deposited at 90 K before annealing to 800 K for 10 seconds to form the (2x2) structure, and to 500 K for 10 seconds to form the $(\sqrt{3}x\sqrt{3})R30°$ structure, producing the sharp LEED patterns shown in Figure 5.1 (a) and 5.1(b) respectively. The $c(7x\sqrt{3})$rect structure was formed by depositing sulfur at room temperature then annealing at 500 K for 5 seconds producing the LEED pattern shown in Figure 5.1(c). For the (2x2) structure, LEED I-V curves were collected at normal incidence for 14 symmetry inequivalent beams from 90 to 300 eV in 2 eV steps for a total energy range of 2322 eV. I-V curves for two separate preparations were averaged together for use in the LEED analysis. LEED I-V curves for the $(\sqrt{3}x\sqrt{3})R30°$ structure

were collected at normal incidence for 11 symmetry inequivalent beams from 90 to 300 eV in 2 eV steps for a total energy range of 1616 eV.

5.3 LEED Analysis

LEED was used to determine both the adsorption site and the adsorbate-induced relaxations of the substrate atoms. An automated search method based on the tensor LEED (TLEED) approximation [32] was used. Nine spin-averaged phase shifts were generated from a muffin-tin model potential formed using relativistic atomic wavefunctions. Additional phase shifts did not influence the results. Scattering between the layers and towards the bulk was modeled using renormalized forward scattering (RFS). Up to 199 beams were necessary to achieve convergence for the interlayer multiple scattering in RFS. Electron damping was simulated by the imaginary part of the inner potential (V_i), which was found to be -5 eV. This damping was determined by fitting its value using the initial best-fit model; it was then used for all the models reported here. Thermal vibrations were modeled using temperature dependent phase shifts. These phase shifts were initially based on isotropic vibrations of the same amplitude for the S atom and metal atoms. The Debye temperature of platinum was set to 250 K, which was determined by fitting the clean surface data [33]. As with the imaginary part of the inner potential, we optimized the vibrational amplitude of the S atom for the initial best-fit model and report further results based on this value. For the sulfur atom, we find a Debye temperature of 417 K which corresponds to a vibrational root-mean-square (rms) enhancement of approximately 1.5 times that determined from initial rms vibrational amplitudes for both S and Pt.

The fit between theoretical and experimental I-V curves was quantified by Pendry's R-factor (R_p-factor) [34] which emphasizes peak positions in the spectra at the

expense of absolute intensity. Error bars were estimated using Pendry's method [34]. We have examined the influence of smoothing the experimental I-V curves, quantifying it by examining the resulting error bars for the initial best-fit model. For both the (2x2) and the ($\sqrt{3}$x$\sqrt{3}$)R30° experimental I-V curves, we find that four three-point smoothings of both the experimental and theoretical I-V curves, after interpolation onto a common 0.25 eV energy grid, minimize the R_p-factor value and the error bars on all optimized parameters. This smoothing was applied to the I-V curves for all models reported here.

5.3.1 Coarse Search

Given only one S atom in the unit cell, based on the previous AES analysis, four high symmetry adsorption sites are possible: top, bridge, fcc-hollow and hcp-hollow. We tested the high symmetry adsorption sites using TLEED analysis coupled with an automated search algorithm. For the (2x2) overlayer, the initial TLEED search was restricted to the (1,0), (0,1), (1,1), (1/2,0), (0,1/2) and (1/2,1/2) beams between 90 and 300 eV for a total energy range of 1198 eV. These beams have the lowest experimental noise and the largest total energy range. The initial search for the ($\sqrt{3}$x$\sqrt{3}$)R30° overlayer used all of the experimentally available beams: (1,0), (0,1), (1,1), (2,0), (0,2), (1/3,1/3), (2/3,2/3), (1/3,4/3), (4/3,1/3), (1/3,7/3), and (7/3,1/3). For each high symmetry site, automated searches were carried out over trial geometries with varying degrees of freedom. When needed, domain averaging was used to recover the full symmetry of the LEED pattern.

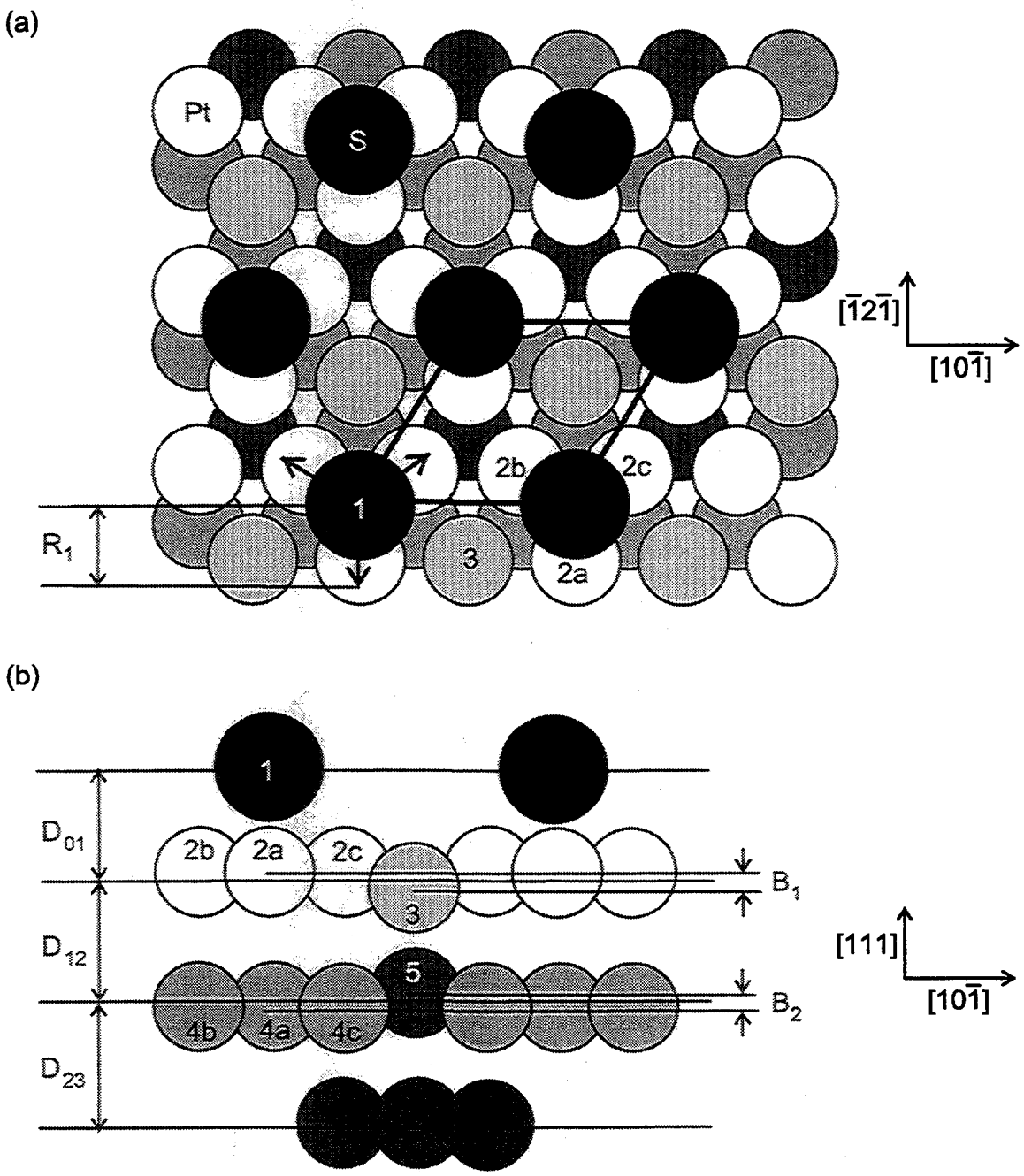

Figure 5.2 Top view (a) and side view (b) of the (2x2)-S structure. The parameter which characterizes the lateral expansion of the triangle of three metal atoms in the second metal layer directly below the S (R2) is not shown. The unit cell is outlined. Inequivalent atoms are shaded differently and numbered; the numbering corresponds to that in Table 5.4.

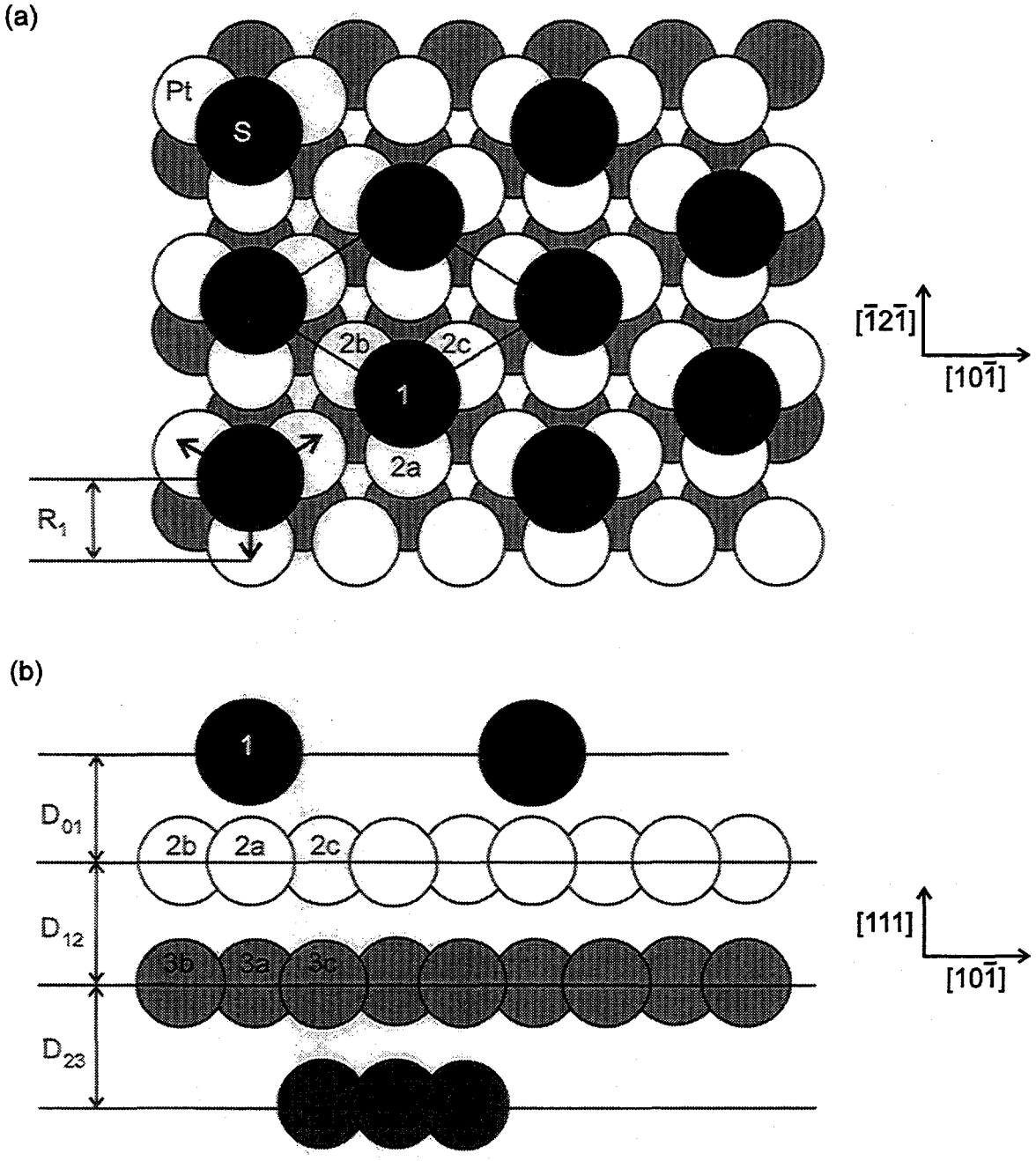

Figure 5.3 Top view (a) and side view (b) of the ($\sqrt{3}$x$\sqrt{3}$)R30°-S overlayer structure. The parameter which characterizes lateral expansion of the triangle of three metal atoms in the second metal layer directly below the S (R2) is not shown. The unit cell is outlined. Inequivalent atoms are shaded differently and numbered; the numbering corresponds to that in Table 5.5.

In our first structural searches, we allowed only the sulfur height and the first two substrate interlayer spacings to vary (D_{01}, D_{12} and D_{23} of Figs. 5.2(b) and 5.3(b)) for each model and overlayer. Table 5.2 summarizes these results under the heading "Planar". Additional perpendicular relaxations in the first two metal layers are possible in all models with the exception of the $(\sqrt{3}x\sqrt{3})R30°$ fcc-hollow site model. These parameters allow for buckling of the metal surface (as an example, B_1 and B_2 shown in Fig. 5.2(b)). The resulting R_p -factors are shown under the heading "Buckled" in Table 5.2. For the fcc-hollow site model, any possible symmetry-allowed relaxation would have to occur in metal layers below the first two metal layers. Although the R_p-factor for the models under the "Planar" heading have the same number of parameters included in the optimization, the models under the "Buckled" heading, due to differences in adsorption site, do not have the same number of parameters. The addition of lateral parameters in the structural search (for example, R_1 in Figures 5.2(a) and 5.3(a)), along with symmetry-breaking relaxations, is described later.

In these initial analyses of the (2x2) and the $(\sqrt{3}x\sqrt{3})R30°$ overlayers, the fcc-hollow site model clearly yields the best fit to the experimental data. The resulting R_p-factor for the other sites shown in Table 5.2 were obtained from structures which have unrealistic interatomic distances. Because the TLEED approximation becomes increasingly inaccurate as displacements get larger (unless the search is iterated), the tabulated R_p-factors do not reflect the true R_p-factor values of the resulting structures. One can use Pendry's method [34] to generate a range of R_p-factor values in which the resulting R_p-factor values of indistinguishable models should fall.

Table 5.2 The resulting R_p-factor values for the best-fit structure of each adsorption site and for various degrees of freedom. "Planar" refers to automated TLEED searches which varied only perpendicular displacements of the S and the top two metal layers. "Buckled" refers to all perpendicular relaxations in the first two metal layers allowed by the local symmetry of the site and determined by automated TLEED searches. (N/A = not allowed)

Site	(2x2)		(√3x√3)R30°	
	Planar	Buckled	Planar	Buckled
fcc-hollow	0.47	0.21	0.18	N/A
hcp-hollow	0.69	0.66	0.74	0.73
top	0.80	0.67	0.71	0.71
bridge	0.65	0.57	0.68	0.66

R_p-factor values of all sites other than the fcc-hollow for both structures fall outside this range centered on the fcc-hollow site's R_p-factor value. The buckling of the metal layers, which is responsible for the considerably lower R_p-factor of the TLEED analysis of the (2x2) overlayer, was not needed to differentiate between the various possible adsorption sites. No buckling of the first two metal layers in the (√3x√3)R30° overlayer was observed in the initial search due to the symmetry of the adsorption site. The third metal layer is the first metal layer in the (√3x√3)R30° fcc-hollow site model which can display a symmetry-allowed buckling. Finally, we see no evidence of symmetry-breaking features in either the (2x2) or the (√3x√3)R30° overlayers.

5.3.2. Effects of Buckling on the (2x2) Model

As seen in Table 5.2, relaxation or buckling of the metal surface results in a dramatic improvement in the agreement between the theoretical and the experimental I-V curves for the (2x2) overlayer. Figure 5.4 illustrates these improvements in the I-V curves of the (2x2) fcc-hollow site model with increasing degrees of freedom. In this figure, the label "Bulk" refers to automated TLEED searches in which only the S height above the ideally-terminated substrate was varied. The labels "Planar" and "Buckled" refer to the same structural optimizations described in the previous section.

In determining adsorbate-induced relaxation of the surface, it was noted that an important consideration in a LEED analysis is the ratio of the energy range of the fractional order beams to that of the integer order beams [35]. This is due to the greater sensitivity of fractional order beams to surface relaxation, as demonstrated for the case of Pt(111)+(2x2)-O [35]. This sensitivity is also illustrated for the (2x2)-S overlayer in Figure 5.4. Shown in Table 5.3 are the error bars computed with Pendry's method [34] for both the integer and fractional, only the integer, or only the fractional order beams using all of the available experimental beams. The restricted data set used in the coarse search gave rise to large error bars (range ± 0.1 Å) for the lateral displacements, R_1 and R_2. The large differences in the error bars shown in Table 5.3 are a direct result of the buckled atoms' contributions to the intensities of fractional order beams. By comparing the I-V curves of the non-relaxed model with those of the buckled model (Figure 5.4), one can clearly see the improvement of the fractional order beams, particularly in the higher energy region. The stronger scattering power of the buckled Pt atoms with respect

to that of the S atoms results in increased intensity in the fractional order beams relative to that which would normally be expected from just the S atoms.

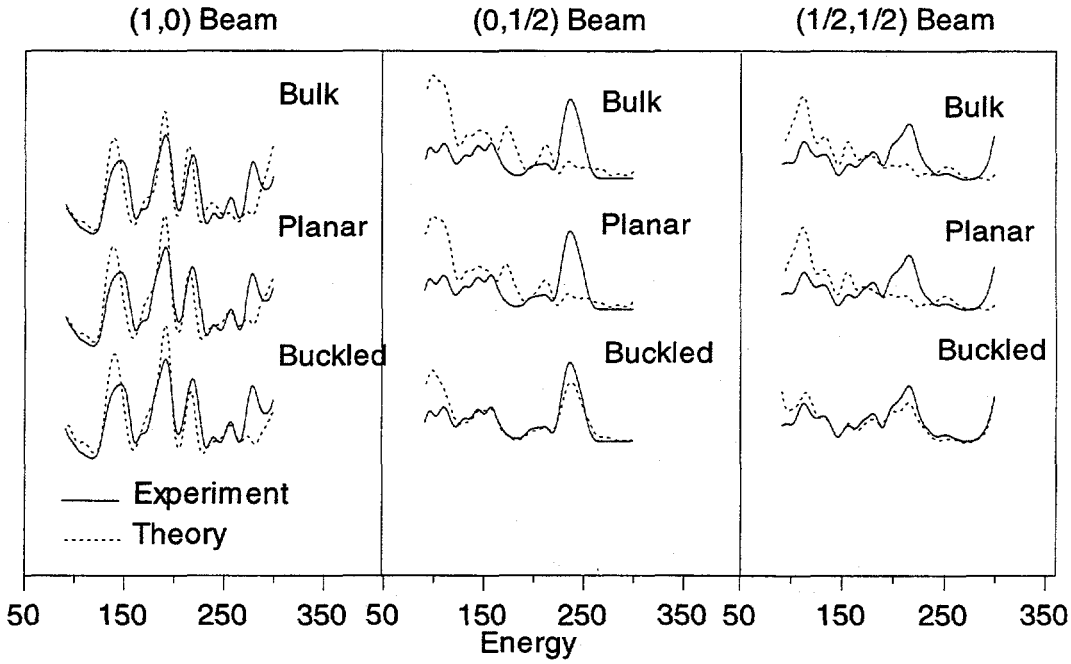

Figure 5.4 Comparison of the (2x2)-S I-V curves for the fcc site model with increasing degrees of freedom. By comparing the I-V curves of the "Planar" (no buckling of Pt atoms) with those of the "Buckled" model, one can clearly see the improvement of the fractional order beams, particularly in the higher energy region.

Table 5.3 Error bars (in Å) computed using Pendry's method [34] with either the fractional order, integer order, or both beam sets for the (2x2) structure. Notice the low sensitivity of the integer order beams to the surface buckling. The geometrical parameters are illustrated in Figures 5.2(a) and Figure 5.2(b).

Parameter	Error Bars		
	R_p-Both	R_p-Fractional	R_p-Integer
D_{01}	± 0.02	± 0.02	± 0.03
D_{12}	± 0.03	± 0.03	± 0.03
D_{23}	± 0.04	± 0.05	± 0.03
B_1	± 0.04	± 0.04	>± 0.1
B_2	± 0.05	± 0.06	>± 0.1
R_1	± 0.04	± 0.04	>± 0.1
R_2	± 0.06	± 0.06	>± 0.1

5.3.3. Lateral Displacements and Symmetry-Breaking Models

We have also examined various models, all based on the best-fit fcc-hollow site model, with different degrees of lateral relaxations of the metal atoms for both overlayers. As above, we used all the available experimental beams in these computations. The addition of fractional order beams with larger momentum transfer parallel to the surface than that found in the beam sets used in the coarse search was necessary to obtain the desired sensitivity to these displacements. The first model contained only relaxations consistent with the three-fold rotational axis and the mirror plane symmetry of the fcc

hollow site. These symmetry-allowed relaxations result in two additional parameters for both the (2x2) and the ($\sqrt{3}$x$\sqrt{3}$)R30° models. In both cases, a lateral expansion or contraction of the triangle of three metal atoms directly bonded to the sulfur and of the triangle of three metal atoms directly below the adsorption site is possible. One of these two parameters, R_1, is illustrated in Figures 5.2(a) and 5.3(a). The next two structural models contain features which break the bulk-like symmetry of the fcc-hollow site. In the first such model, the mirror plane was broken by allowing the triangle of three Pt atoms bonded to the S atom to rotate in-plane (*p3* symmetry); in the second the rotational symmetry was broken by allowing two of the three Pt atoms bonded to the S atom to move together and the third to move separately. Symmetry in the LEED pattern was regained by averaging beam intensities over the resulting domains. The small decrease in the R_p-factor value with an increasing number of parameters contained in these last two models does not allow one to distinguish between these models and the symmetry-conserving model. However, because of the large error bars (greater than 0.10 Å) associated with these symmetry-breaking displacements and because of the symmetry of the adsorption site, we believe that there are no detectable symmetry-breaking features in either the (2x2) or the ($\sqrt{3}$x$\sqrt{3}$)R30° overlayers.

5.4 LEED Results

The (2x2) and ($\sqrt{3}$x$\sqrt{3}$)R30° structures which resulted from the initial analysis were used as a starting point for the final analysis. We optimized all parameters which

are consistent with the bulk-like symmetry of the overlayer. For the final structures, we iterated automated TLEED structural searches starting from new reference structures until the resulting structure was within a 0.02 Å radius of the last reference structure. In this way, we were able to eliminate any error caused by the TLEED approximation in the final structure. We find that iteration, and thus re-computation of the reference structure, is imperative to minimize the errors induced by the TLEED approximation, which can affect the final structure.

5.4.1 Final (2x2) Structure

The final structure obtained for the Pt(111)- (2x2) -S has S atoms adsorbed in fcc-hollow sites with an R_p-factor of 0.22. Details of this final structure can be found in Table 5.4, and a comparison of final theoretical and experimental I-V curves in Figure 5.5. We find that the S atom induces a buckling (see Figure 5.2(b) for the relative displacements of the metal atoms within the layer) of 0.08 ± 0.04 and 0.08 ± 0.05 Å in the first and second metal layers respectively. In addition, sulfur induces a probable expansion of 0.03 ± 0.04 Å in the first metal-metal interlayer spacing and a possible small contraction of 0.02 ± 0.06 Å in the second. A metal-sulfur bond length of 2.24 Å was found. Lateral displacements consistent with the three-fold rotational and mirror plane symmetries yield a possible small lateral expansion (0.03 ± 0.04 Å) of the triangle of three metal atoms directly bonded to the sulfur. This expansion is within the error bars of the bulk positions.

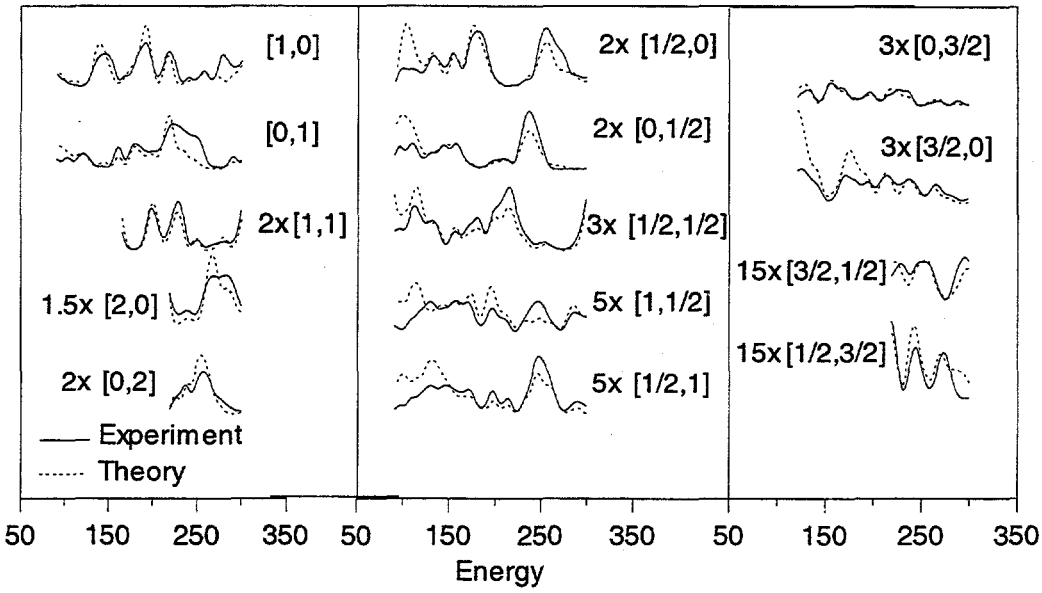

Figure 5.5 I-V curves of the best-fit (2x2)-S structure with an Rp-factor of 0.22. Some I-V curves are magnified as noted to give comparable intensity values

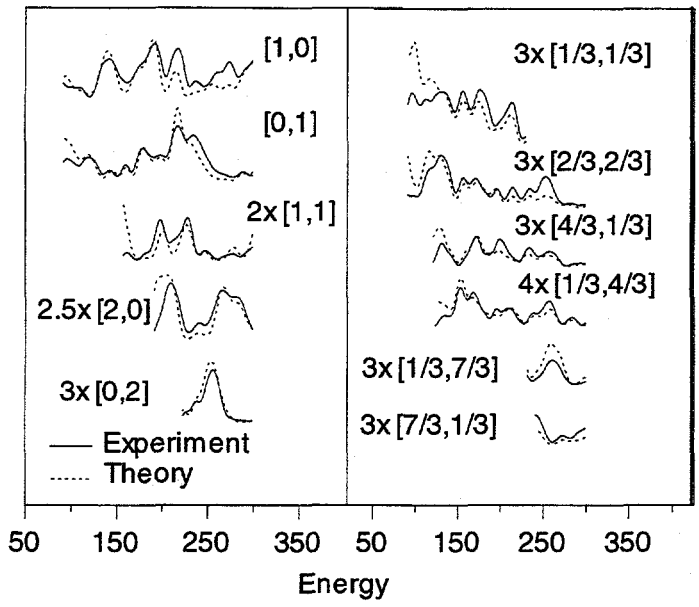

Figure 5.6 I-V curves of the best-fit ($\sqrt{3}$x$\sqrt{3}$)R30°-S structure with an Rp-factor of 0.18. Some I-V curves are magnified as noted to give comparable intensity values

Table 5.4 Optimal atomic coordinates (in Å) for the Pt(111)-(2x2)-S fcc hollow site model with an *Rp*-factor of 0.22. *X* coordinate is defined as positive towards the bulk. *Y* and *Z* are coordinates parallel to the surface. The "Atom" numbers correspond to inequivalent atoms labeled in Figures 5.2(a) and 5.2(b). Error bars are given for each set of equivalent atoms.

Atom	*X*	*Y*	*Z*
1 S	0.00 ± 0.02	0.00	0.00
2a Pt	1.54 ± 0.03	0.00	1.63 ± 0.04
2b Pt	1.54	1.41	-0.82
2c Pt	1.54	-1.41	-0.82
3 Pt	1.62 ± 0.04	0.00	-3.20
4 Pt	3.80 ± 0.05	2.77	-1.60
5a Pt	3.88 ± 0.04	0.00	-1.60 ± 0.06
5b Pt	3.88	1.38	0.80
5c Pt	3.88	-1.38	0.80
Bulk repeat vector			
	2.2650	0.0000	1.6016
2D repeat vectors			
		2.7740	4.8048
		2.7740	-4.8048

Table 5.5 Optimal atomic coordinates (in Å) for the Pt(111)- ($\sqrt{3}x\sqrt{3}$)R30° -S fcc hollow site model with an *Rp*-factor of 0.18. *X* coordinate is defined as positive towards the bulk. *Y* and *Z* are coordinates parallel to the surface. The "Atom" numbers correspond to inequivalent atoms labeled in Figures 5.3(a) and 3(b). Error bars are given for each set of equivalent atoms.

Atom	*X*	*Y*	*Z*
1 S	0.00 ± 0.02	0.00	0.00
2a Pt	1.55 ± 0.03	0.00	1.63 ± 0.04
2b Pt	1.55	1.42	-0.82
2c Pt	1.55	-1.42	-0.82
3a Pt	3.83 ± 0.03	0.00	-1.61 ± 0.05
3b Pt	3.83	1.39	0.81
3c Pt	3.83	-1.39	0.81
Bulk repeat vector			
	2.2650	0.0000	1.6016
2D repeat vectors			
		4.1610	2.4024
		0.0000	-4.8047

5.4.2. Final ($\sqrt{3}$x$\sqrt{3}$)R30° Structure

The final structure obtained for the Pt(111)-($\sqrt{3}$x$\sqrt{3}$)R30°-S has S atoms adsorbed in fcc hollow sites with an R_p-factor of 0.18. Details of this final structure can be found in Table 5.5, and a comparison of final theoretical and experimental I-V curves in Figure 5.6. Sulfur induces a probable expansion of 0.01 ± 0.04 Å in the first metal-metal interlayer spacing and a possible small contraction of 0.02 ± 0.05 Å in the second. A metal-sulfur bond length of 2.25 Å was found. Lateral displacements consistent with the three-fold rotational and mirror plane symmetries yield a possible small lateral expansion of the triangle of three metal atoms directly bonded to the sulfur. This expansion is within error bars of the bulk positions.

5.5 Discussion

From LEED studies of the (2x2) and the ($\sqrt{3}$x$\sqrt{3}$)R30° overlayers, we find a very close similarity in the local bonding of S atoms on Pt(111). The adsorption site, fcc-hollow, is the same. The metal-sulfur bond lengths are practically identical. Examining the metal-to-metal interlayer spacings, we again find similarity: a small expansion of the first and subsequent contraction of the second for each system. The lateral expansions of the triangle of three atoms under the adsorbate (R_1 in Figures 5.2(a) and 5.3(a)) are within error bars the same for both systems. Our structural results for Pt are qualitatively similar to what was found for the (2x2) and ($\sqrt{3}$x$\sqrt{3}$)R30° overlayers on Ru(0001) [29] and for

the (2x2) overlayer on Re(0001) [22] with the exception that, on these hcp metal surfaces, the sulfur is found in the hcp-hollow site. As is the case for other fcc(111) surfaces [4, 14, 36, 37], we find an fcc hollow site for sulfur adsorption. The Pt-S bond lengths of 2.24 Å for the (2x2) overlayer and 2.25 Å for the (√3x√3)R30° overlayer are also within the range of metal-S bond lengths found on other metal surfaces. Our bond lengths are a little shorter than the values found for the (√3x√3)R30° overlayers on Ir (2.28 Å) [4], but are larger than the values for Ni (2.10 Å) [11, 37] Pd (2.23 Å) [14], and Rh (2.18 Å) [36]. The Pt-S height found in our analysis is shorter by 0.02 Å than the value found by Hayek et al. [20], however our R_p-factor is less than half of theirs. For both overlayers, our Pt-S bond lengths are shorter than the value 2.32 Å of the PtS compound [38].

Table 5.6 Comparison of various geometrical parameters (in Å) for the (2x2) and the (√3x√3)R30° sulfur structures on Pt(111). The (2x2) parameters are shown in Figures 5.2(a) and 5.2(b), while the (√3x√3)R30° parameters are illustrated in Figures 5.3(a) and 5.3(b). Because there are no relaxations of the metal surface for the (√3x√3)R30° overlayer, the parameters B_1 and B_2 apply only to the (2x2) overlayer.

	(2x2)	(√3x√3)R30°
D_{01}	1.54 ± 0.02	1.55 ± 0.02
D_{12}	2.30 ± 0.03	2.28 ± 0.03
B_1	0.08 ± 0.04	N/A
D_{23}	2.25 ± 0.05	2.24 ± 0.03
B_2	0.08 ± 0.05	N/A
R_1	0.03 ± 0.04	0.01 ± 0.04
R_2	0.02 ± 0.06	0.02 ± 0.05

The lower coordination number (C.N.) of adsorbed sulfur on Pt surface (C.N.=3) with respect to the PtS compound (C.N.=4) is in agreement with the idea that lower coordination numbers can be associated with a shortening of the bond length [39].One difference between our two structures is the lack of buckling in the (√3x√3)R30° structure: buckling is symmetry-forbidden in the (√3x√3)R30° structure, but allowed in the (2x2) structure. Comparison of structural parameters for the (2x2) and (√3x√3)R30° structures are presented in Table 5.6.

5.6 Conclusions

We studied three ordered overlayers of sulfur on Pt(111) using LEED. The best agreement with calculated LEED *I-V* curves was obtained for the fcc site models for the (2x2) and the (√3x√3)R30° overlayers. Comparing the (2x2) and the (√3x√3)R30° overlayers, we find similarity in the local bonding of the S atom with almost identical Pt-S bond distances; 2.24 Å for the (2x2) overlayer and 2.25 Å for the (√3x√3)R30° overlayer. Also it was observed that there is a small expansion of the first layer Pt atoms adjacent to adsorbed sulfur atom and subsequent contraction of the second layer for each system. However, the buckling of substrate atoms was only observed in the (2x2) structure; it is symmetry-forbidden in the (√3x√3)R30° structure.

Chapter 5 References

1. H. Ohtani, C.-T. Kao, M.A.V. Hove, and G.A. Somorjai, Progress in Surf. Sci., 1986. **23**: p. 155.
2. P.R. Watson, M.A. Van Hove, and K. Hermann, *NIST Surface Structure Database ver. 2.0,*. NIST Standard Reference Data Program. 1995, Gaithersburg, MD.
3. G. Rouida and F. Pratesi, Surf. Sci., 1981. **104**: p. 609.
4. C.M. Chan and W.H. Weinberg, J. Chem. Phys., 1979. **71**: p. 3988.
5. M.D. Craper, C.E. Riley, P.J.J. Sweeney, C.F. McConville, D.P. Woodruff, and R.G. Jones, Surf. Sci., 1987. **182**(213).
6. K. Motai, T. Hashizume, H. Lu, D. Jeon, T. Sakurai, and H.W. Pickering, Appl. Surf. Sci., 1993. **67**: p. 246.
7. J.L. Domange and J. Oudar, Surf. Sci., 1968. **11**: p. 124.
8. N.P. Prince, D.L. Seymour, M.J. Ashwin, C.F. McConville, D.P. Woodruff, and R.G. Jones, Surf. Sci., 1990. **230**: p. 13.
9. J.M. Wilson, Surf. Sci., 1976. **59**: p. 315.
10. M. Perdereau and J. Oudar, Surf. Sci., 1970. **20**: p. 80.
11. Y.K. Wu and K.A.R. Mitchell, Can. J. Chem., 1975. **67**: p. 89.
12. P. Delescluse and A. Masson, Surf. Sci., 1980. **100**: p. 423.
13. L. Ruan, I. Stensgaard, F. Besenbacher, and E. Lægsgaard, .
14. M.E. Grillo, C. Stempfl, and W. Berndt, Surf. Sci., 1994. **317**: p. 84.
15. J.G. Forbes, A.J. Gellman, J.C. Dunphy, and M. Salmeron, Surf. Sci., 1992. **279**: p. 68.

16. P. Marcus, A. Teissier, and J. Oudar, Surf. Sci., 1983. **129**: p. 43.

17. Y. Berthier, M. Perdereau, and J. Oudar, Surf. Sci., 1973. **36**: p. 225.

18. W. Heegemann, K.H. Meister, E. Bechtold, and K. Hayek, Surf. Sci., 1975. **49**: p. 161.

19. K. Hayek, H. Glassl, A. Gutmann, H. Leonhard, M. Prutton, S. Tear, and M. Welton-Cook, Surf. Sci., 1985. **172/173**: p. 419.

20. K. Hayek, H. Glassl, A. Gutmann, H. Leonhard, M. Prutton, S.P. Tear, and M.R. Welton-Cook, Surf. Sci., 1986. **175**: p. 535.

21. D.J. Kelly, A.J. Gellman, M. Salmeron, G.A. Somorjai, V. Maurice, M. Hueber, and J. Oudar, Phys. Rev. B, 1988. **44**: p. 1914.

22. A. Barbieri, D. Jentz, N. Materer, G. Held, J.C. Dunphy, D.F. Ogletree, P. Sautet, M. Salmeron, and G.A. Somorjai, Surf. Sci., 1994. **312**: p. 10.

23. D.F. Ogletree, R.Q. Hwang, D.M. Zeglinski, A.L. Vazquez-de-Parga, G.A. Somorjai, and M. Salmeron, J. Vac. Sci. Technol. B, 1991. **9**: p. 886.

24. J.S. Foord and A.E. Reynolds, Surf. Sci., 1985. **152/153**: p. 426.

25. K.C. Wong, W. Liu, M. Saidy, and K.A.R. Mitchell, Surf. Sci., 1996. **345**: p. 101.

26. H.A. Yoon, M. Salmeron, and G.A. Somorjai, Langmuir, 1996.

27. S.R. Kelemen and T.E. Fischer, Surf. Sci., 1979. **87**: p. 53.

28. R. Dennert, M. Solokowski, and H. Pfnür, Surf. Sci., 1992. **271**: p. 1.

29. D. Jürgens, G. Held, and H. Pfnür, Surf. Sci., 1994. **303**: p. 77.

30. D. Heuer, T. Müller, H. Pfnür, and U. Kohler, Surf. Sci., 1993. **297**: p. L61.

31. C. Wagner, J. Chem. Phys., 1953. **21**: p. 1819.

32. M.A. Van Hove, W. Moritz, H. Over, P.J. Rous, A. Wander, A. Barbieri, N. Materer, U. Starke, D. Jentz, J.M. Powers, G. Held, and G.A. Somorjai, Surf. Sci. Rep., 1993. **19**: p. 191.

33. N. Materer, U. Starke, A. Barbieri, R. Döll, K. Heinz, M.A. Van Hove, and G.A. Somorjai, Surf. Sci., 1995. **325**: p. 207.

34. J.B. Pendry, J. Phys. C, 1980. **13**: p. 937.

35. N. Materer, A. Barbieri, D. Gardin, U. Starke, J.D. Batteas, M.A. Van Hove, and G.A. Somorjai, Surf. Sci., 1994. **303**: p. 319.

36. P.C. Wong, M.Y. Zhou, K.C. Hui, and K.A.R. Mitchell, Surf. Sci., 1985. **163**: p. 172.

37. J.E. Demuth, P.M. Marcus, and D.W. Jepsen, Phys. Rev. Lett., 1974. **32**: p. 1182.

38. Wyckoff, *Crystal Structures*. Vol. 1. 1963, New York: Wiley.

39. K.A.R. Mitchel, Surf. Sci., 1980. **100**: p. 225.

Chapter 6

Coverage dependency of overlayer structures:

I. Surface structures of sulfur overlayers on Pt(111)

6.1 Introduction

Many surface structures have been determined by LEED in considerable detail [1], as discussed in the previous chapter. However, the information obtained from LEED is an average over many equivalent atoms, often ignoring the involvement of local defects. Also, for complex structures, LEED does not provide a direct identification of the model that solves the surface structure. By contrast, STM images single atoms and defects as well as ordered structures, and can in favorable cases directly indicate the structural model, or at least set severe restrictions on possible structural models [2]. In addition, with computational modeling of STM images (analogous to LEED modeling of LEED intensities), one may extract more detailed structural information as well [3, 4]. In this study, the (2x2) and the $(\sqrt{3}x\sqrt{3})R30^{o}$ structures were imaged with STM, and the

findings from the LEED study were applied to elucidate the more complex high-coverage c(7x$\sqrt{3}$)rect structure by using STM.

STM has been applied to study sulfur overlayers on numerous metal substrates: Cu(111) [5], Mo(100) [6], Pd(111) [7], Ni(111) [8], Pd(100) [2], Pt(111) [9], Re(0001) [10], and Ru(0001) [11]. Each sulfur atom appears to always produce a maximum in topography in these images at low coverage. However there are apparent disagreements in some structures formed at high coverage. In the case of c(4x2)-3S on Mo(100), one sees only one maximum per unit cell in the image, while from both coverage and LEED analysis it is clear that there are two more sulfur atoms, at a slightly lower height on the surface which do not appear in the STM images. This is due to destructive interference in the tunneling amplitude where the tip is located over the low lying S atom [4]. Other effects of high coverage are the possible restructuring of the substrate (compound formation) and occupation of lower energy sites by sulfur due to overcrowding. In the case of the ($\sqrt{7}$x$\sqrt{7}$)R19.1^{o}-3S on Cu(111) [5], only one protrusion could be imaged and a model with reconstruction in the substrate was suggested. Forbes et al. [7] performed STM studies on Pd(111)-($\sqrt{7}$x$\sqrt{7}$)R19.1^{o}-3S proposing that some sulfur atoms penetrate the subsurface. Recently, occupation of both hcp- and fcc-hollow sites was reported for sulfur on Ru(0001). When sulfur was added to the Ru(0001)-($\sqrt{3}$x$\sqrt{3}$)R30° overlayer, it first results in domain wall formation, and then in a c(4x2) structure with equal numbers of fcc- and hcp-hollow site occupation [12].

On Pt(111), three ordered overlayers -(2x2), ($\sqrt{3}$x$\sqrt{3}$)R30° and c($\sqrt{3}$x7)rect - are observed depending on the sulfur coverage as described in the previous chapter. In this

chapter, the images of the (2x2) and ($\sqrt{3}$x$\sqrt{3}$)R30° structures are discussed, followed by the adsorption site determination for c($\sqrt{3}$x7)rect structure by STM.

6.2 Experiments

The procedure for forming the different ordered overlayers of sulfur is the same as for the LEED study as discussed in the previous chapter. However, for the STM experiments, the sample is kept at room temperature during deposition of sulfur. After the sulfur was deposited, then sample was annealed to 500 to 800 K to get the desired ordered LEED pattern. After annealing, the sample was allowed to cool down to room temperature to minimize the thermal drift in the STM. All of the STM experiments were carried out at room temperature with a sample bias from - 50 to 100 mV and a tunneling current varying from 1.0 to 2.0 nA in topographic mode.

6.3 STM Analysis

STM images of (2x2) and ($\sqrt{3}$x$\sqrt{3}$)R30° structures were taken after corresponding LEED patterns were obtained. Images of the (2x2) sulfur structure taken at 1 nA and 30 mV exhibit one protrusion per unit cell with a corrugation of 0.2 Å, as shown in Figure 6.1(a). Each maximum was assigned to a sulfur atom based on the previous studies of sulfur on Pt(111) [9], and other metals (Mo(001) [6], Re(0001) [10]) at lower coverage limit (< 0.33 ML). The images calculated based on theory suggest that sulfur is always imaged as protrusion [13]. Changes in bias voltage produced similar images. Topographic images of the ($\sqrt{3}$x$\sqrt{3}$)R30° structure as shown in Figure 6.1(b), for 1.0 nA and 100 mV, also show features similar to the (2x2) case. The protrusions have a 0.3 Å corrugation and one protrusion per unit cell was imaged. These STM results confirm the previous AES and LEED studies which indicate that there is only one sulfur atom in the unit cell for both overlayer structures. When the coverage of sulfur is less than the 0.25 ML needed to form a complete (2x2) overlayer, an image such as in Figure 6.2 was obtained. This 120 Å x 115 Å image was taken at 2 nA and 100 mV. In this image, an ordered domain of (2x2) sulfur structure is visible, surrounded by diffuse background. The surrounding area is probably covered with sulfur as well, however, these atoms may diffuse on the surface faster than the scanning rate of the tip. In these experiments, a low scanning rate, about 100 ms/line (corresponding to 400 Å/s), was used to produce the topographic images. In this larger area image, individual atoms were not well-resolved, rather rows of sulfur atoms were visible. The poor resolution in one direction is probably due to an asymmetric tip.

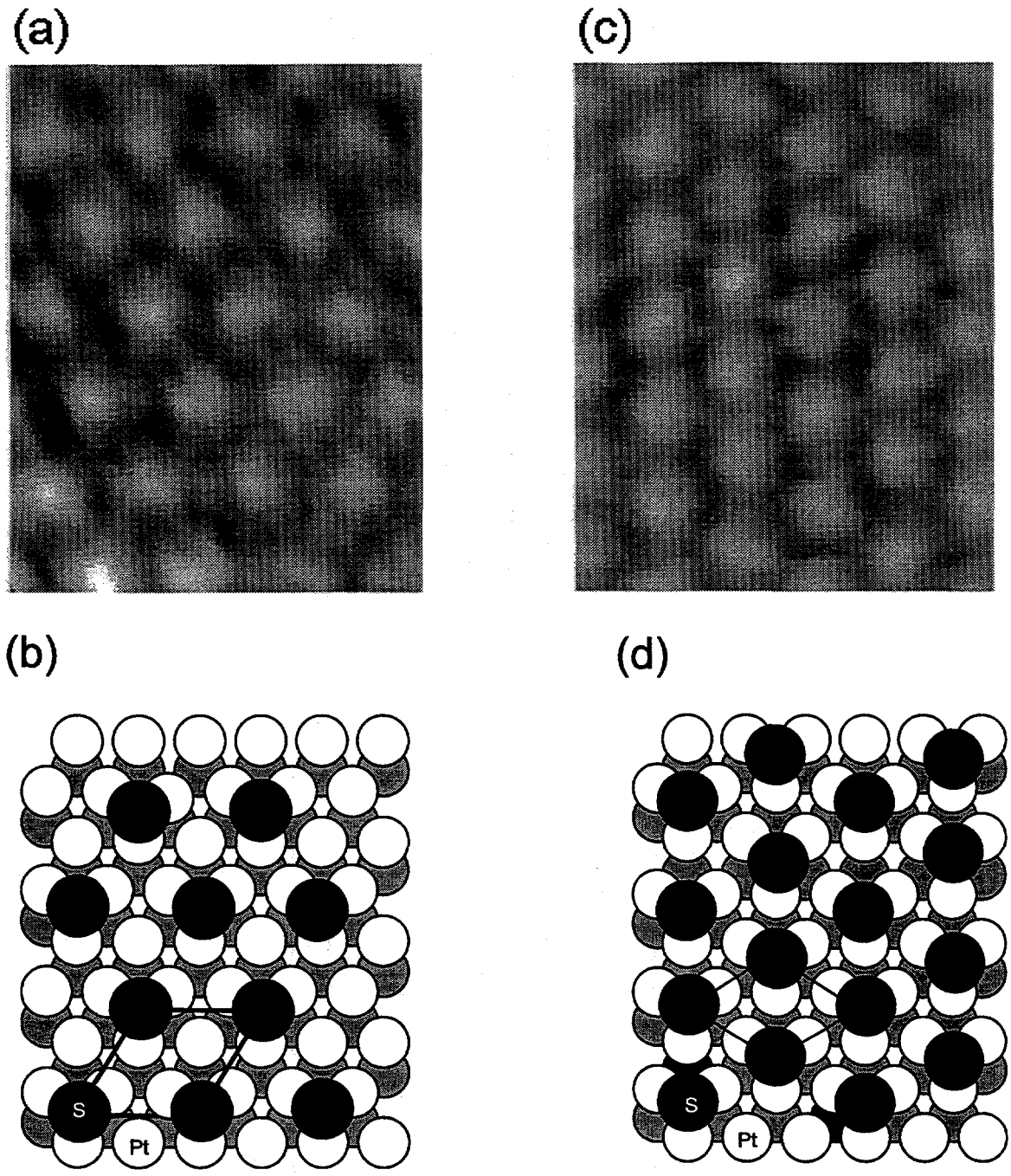

Figure 6.1 Topographic image (23 Å x 30 Å) at 1 nA and 30 mV (a) and its model (b) of (2x2) sulfur overlayer on Pt(111). Topographic image taken at 1 nA and 100 mV (20 Å x 25 Å) (c) and its model (d) of the ($\sqrt{3}$x$\sqrt{3}$)R30° sulfur overlayer

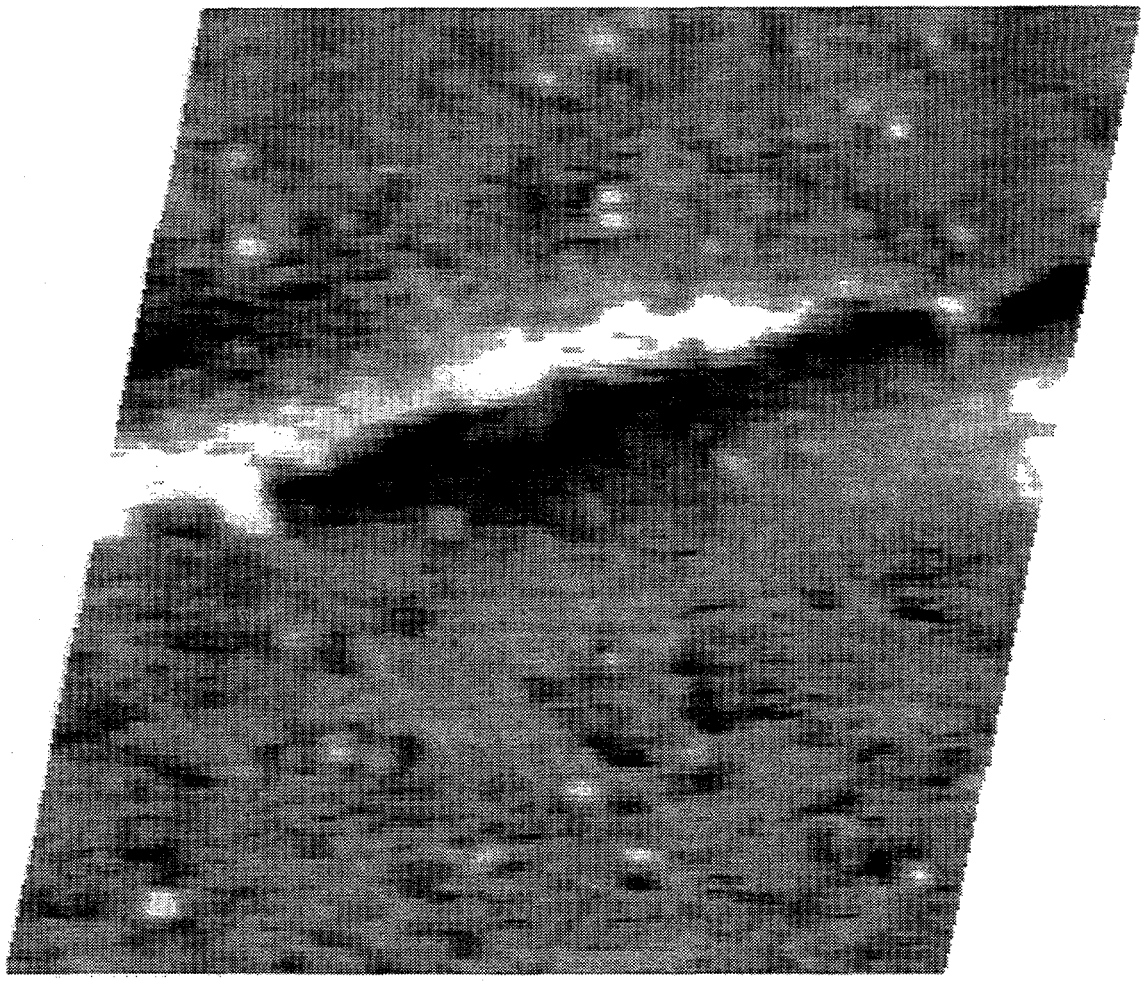

Figure 6.2 Low resolution topographic image (120 Å x 115 Å) of the surface with less than 0.25 ML of sulfur. A domain with row-like features is visible.

When the coverage of sulfur increases over 1/3 ML, a c(7x$\sqrt{3}$)rect LEED pattern was obtained. A typical topographic image of c(7x$\sqrt{3}$)rect overlayer, taken at -50 mV and 1 nA, is shown in Figure 6.3(a). We assign the bright spots as sulfur, based on the fact that point defects due to missing sulfur atoms are imaged as minima in the image. From such an image, three sulfur atoms can be imaged in the unit cell. Two different types of sulfur atoms in the unit cell can be seen in this image. The bright one appears 0.15 Å higher than the other two, under the tunneling condition used. This STM image shows that there are three atoms per unit cell confirming the AES results carried out by Heegemann et al [14]. Since the substrate is three-fold symmetric, three rotational domains can exist for the c(7x$\sqrt{3}$)rect-3S overlayer on Pt(111). In Figure 6.3(b), two domain orientation separated by a step can be seen. This image has been processed to remove the step to improve the clarity of these two domains. Rows of c(7x$\sqrt{3}$)rect-3S surface overlayer are visible on both terraces. The symmetry in the LEED pattern must be due then to domain averaging.

When the coverage of sulfur is just below that needed to form a complete c(7x$\sqrt{3}$)rect-3S overlayer, a mixed overlayer with both c(7x$\sqrt{3}$)rect-3S and ($\sqrt{3}$x$\sqrt{3}$)R30° can be seen. In Figure 6.4, two different overlayer structures could be imaged. At the top of the image, a c(7x$\sqrt{3}$)rect-3S overlayer structure is visible, while at the left bottom of the image corresponding to sulfur forming a ($\sqrt{3}$x$\sqrt{3}$)R30° overlayer structure are observed. Based on the fcc-hollow adsorption site for sulfur in the ($\sqrt{3}$x$\sqrt{3}$)R30° structure, (1x1) grid is superimposed on the image, as shown in Figure 6.4(b). The corners of the triangles are positioned at the maxima in the ($\sqrt{3}$x$\sqrt{3}$)R30° structure, which represent fcc-hollow sites. In the c(7x$\sqrt{3}$)rect structure region, two sulfur adsorption sites

are observed. The less bright maxima are positioned at the corners of the triangles (fcc-hollow sites) while the brighter maxima are positioned in the middle of rhombus (hcp-hollow sites). Images taken with different sample bias voltages (from 0.05 to 1.0 V) while keeping the tunneling current constant show that in all cases, the sulfur atom on the hcp-hollow sites appear higher (brighter) than those in the fcc-hollow sites. A model of the c(7x$\sqrt{3}$)rect-3S structure is illustrated in Figure 6.5, based on our STM experiments.

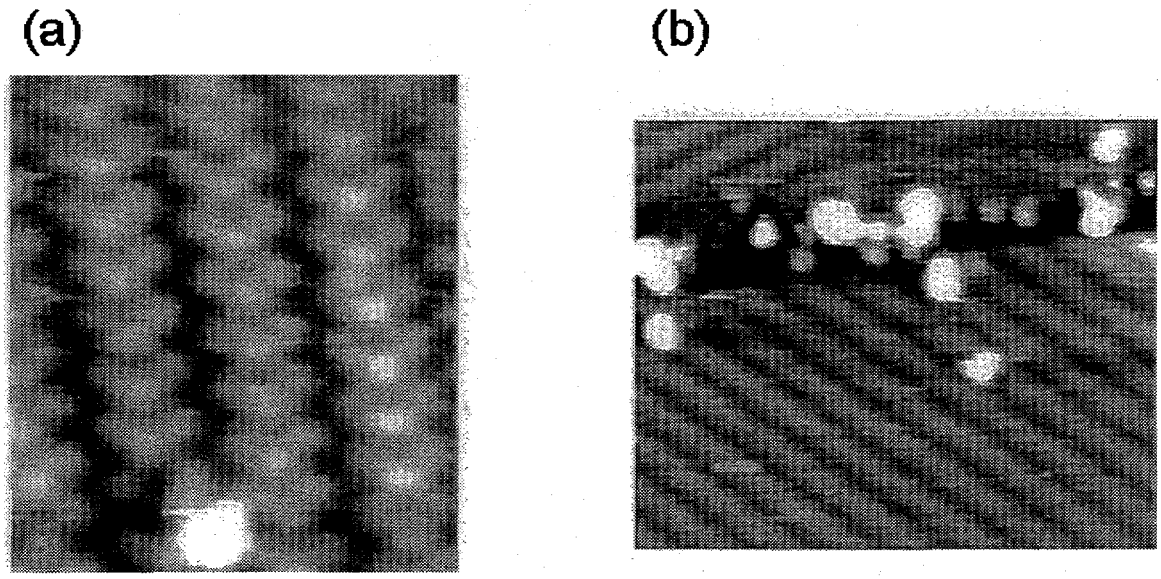

Figure 6.3 (a) Topographic image of c(7x$\sqrt{3}$)rect -3S structure taken at -50 mV and 1 nA (35 Å x 40 Å). A point defect is imaged as missing protrusion in the image suggesting that each protrusion is due to a sulfur atom. Three sulfur atoms can be seen in the unit cell. (b) Larger area (160 Å x 130 Å) image of the c(7x$\sqrt{3}$)rect-3S structure. Rows of c(7x$\sqrt{3}$)rect-3S overlayer are visible. Two different domain orientations of this c(7x$\sqrt{3}$)rect-3S separated by the step can be observed. This image has been processed to remove the step from the image to clarify two domains.

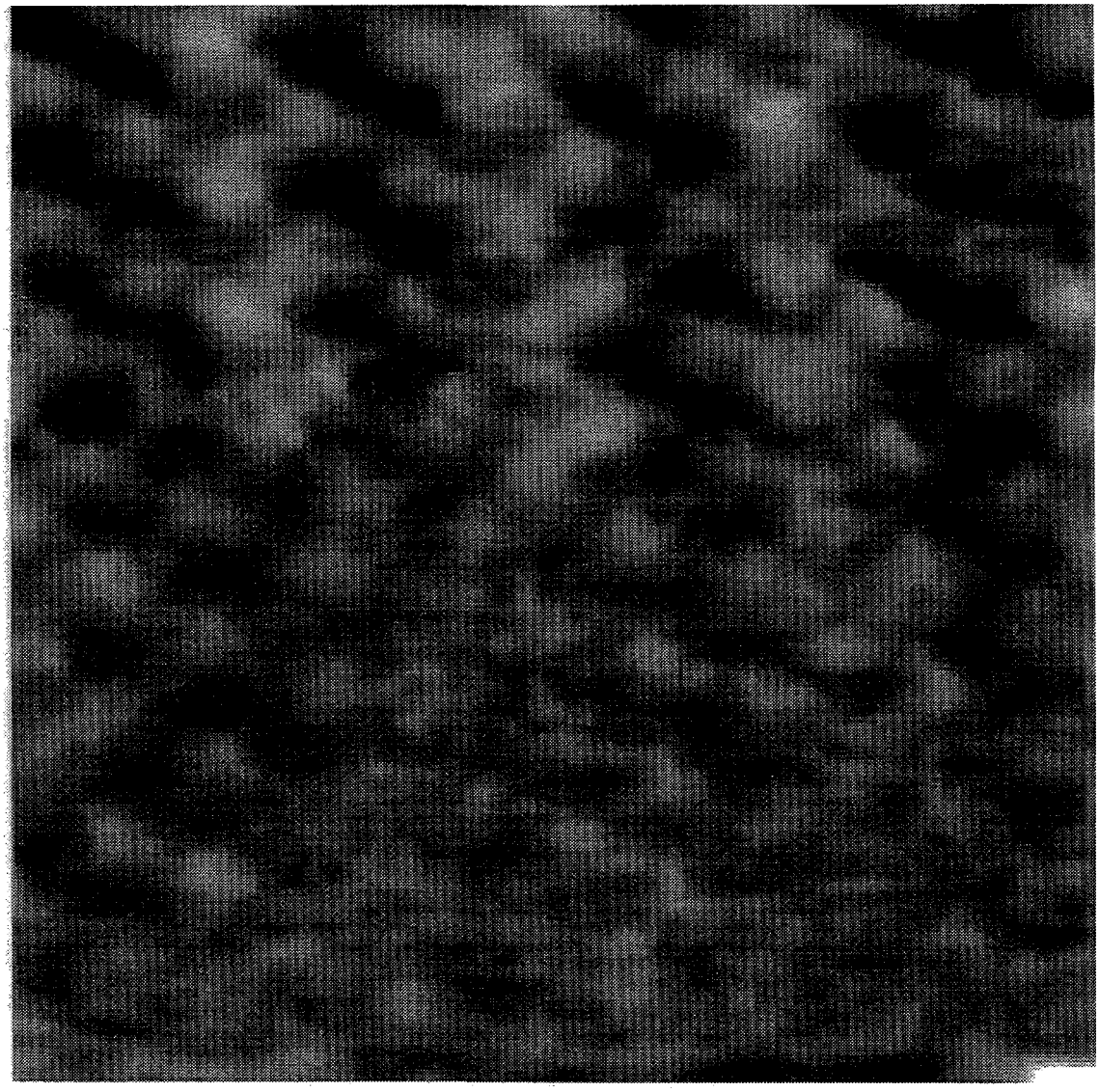

Figure 6.4 (a) Topographic image of the surface with both c(7x√3)rect-3S and (√3x√3)R30° structures. The domains of c(7x√3)rect-3S is visible at the top of the image while small domain of (√3x√3)R30° structure is observed at left side of the image.

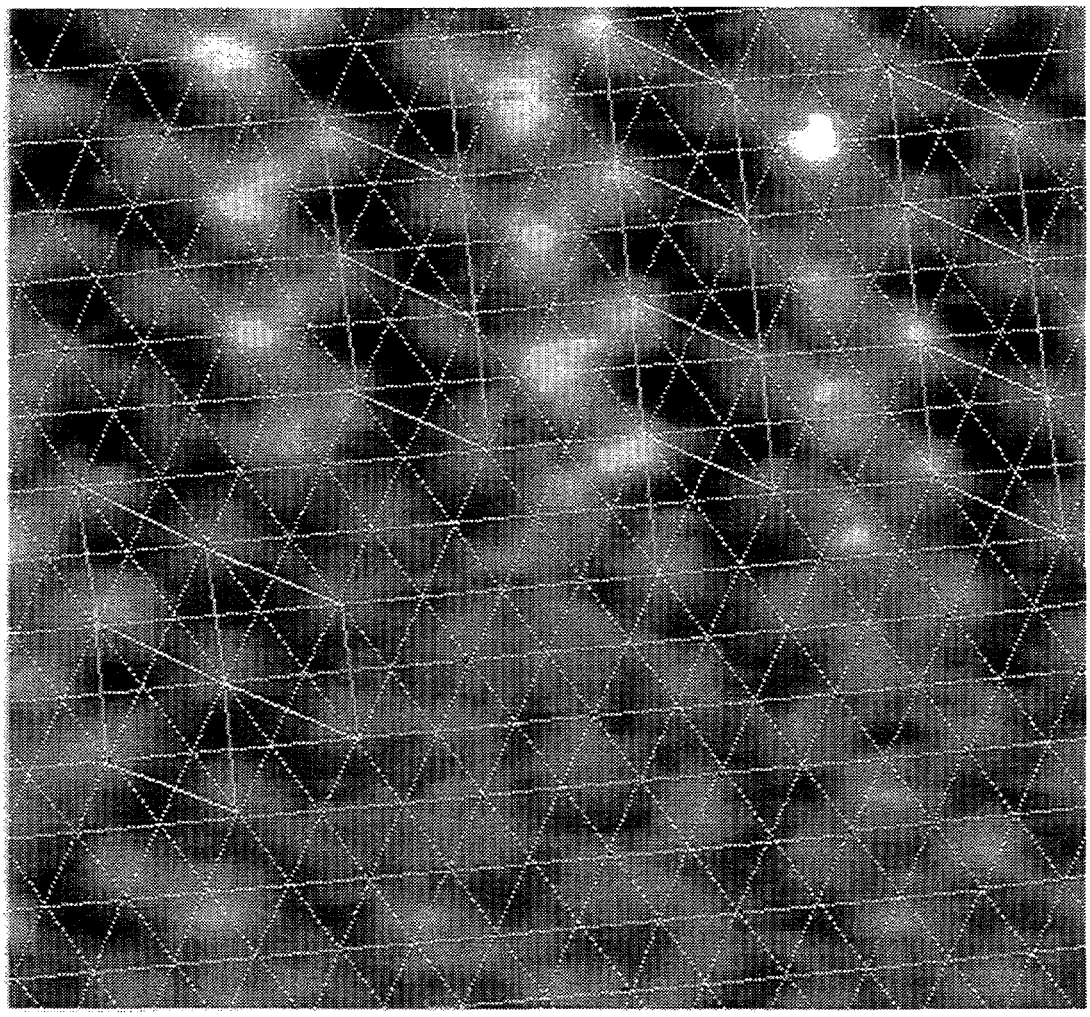

Figure 6.4 (b) (1x1) grid was superimposed on the same image as Figure 6.3(a). Based on the fcc-hollow adsorption site for sulfur in the ($\sqrt{3}$x$\sqrt{3}$)R30° structure, all the fcc-hollow sites are marked as the corners of the triangles. Thereby, it is possible to extrapolate the adsorption site for sulfur atoms in the c(7x$\sqrt{3}$)rect-3S structure. One sulfur atom with the highest corrugation has the hcp-hollow adsorption site, while two other sulfur atoms sit in the fcc-hollow site. Sulfur atoms in fcc sites form rows of ($\sqrt{3}$x$\sqrt{3}$)R30° overlayer structure

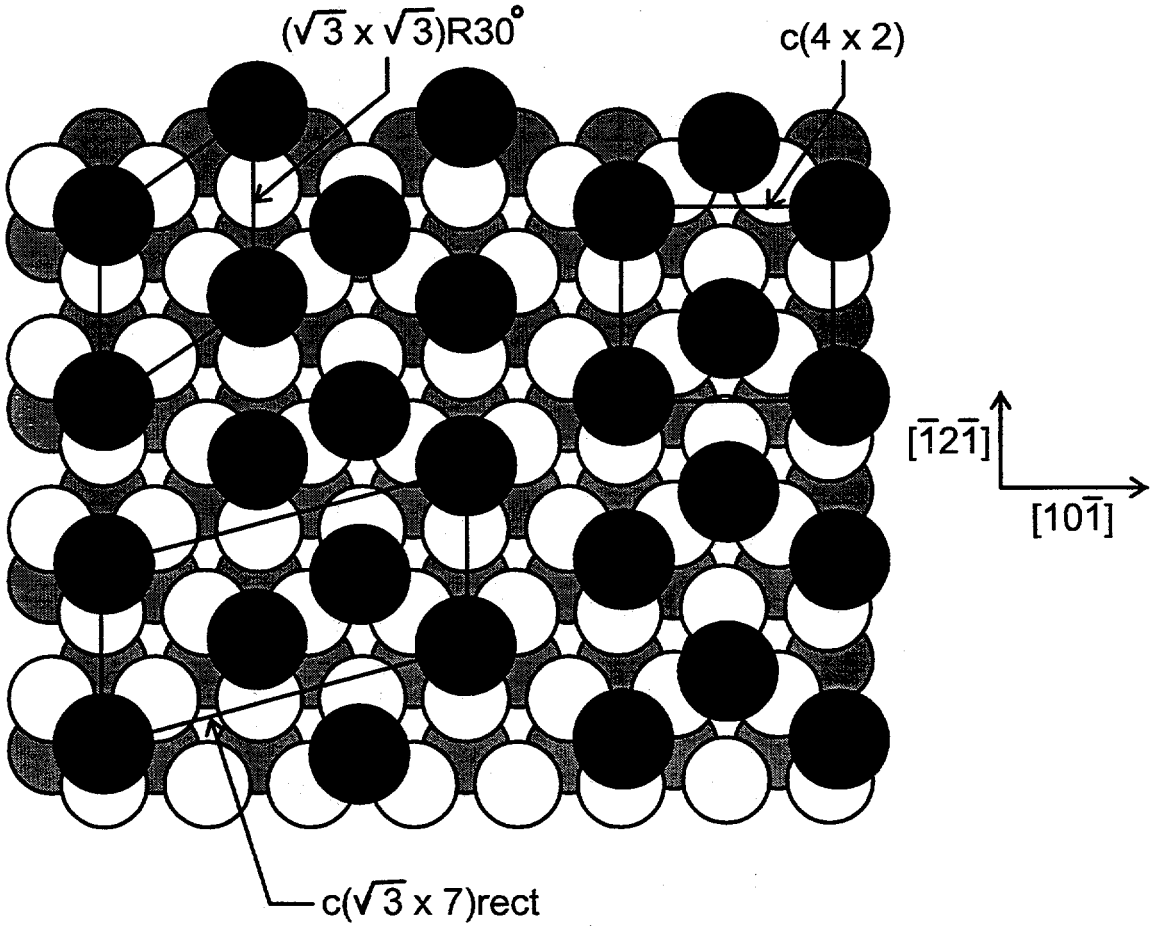

Figure 6.5 Proposed model for both c(7x√3)rect-3S structure based on our STM experiment. There are two sulfur atoms in the fcc-hollow sites and one in the hcp-hollow site. Several unit cells are outlined.

6.4 Discussion

Our STM images for the structure with less than 0.25 ML of sulfur indicate the formation of (2x2) islands surrounded by possibly mobile sulfur atoms, as shown in Figure 6.2. This suggests that sulfur atoms spaced by twice the Pt lattice parameter attract each other, results also found by Dunphy et al. for sulfur on the Re(0001) surface [15]. One maximum for each sulfur atom was observed for both the (2x2) and ($\sqrt{3}$x$\sqrt{3}$)R30° structures (as shown in Figures 6.1(a) and 6.1(b)). Topographic images for the c(7x$\sqrt{3}$)rect-3S overlayer indicate that both the fcc- and hcp-hollow sites are occupied by sulfur atoms. Under our experimental conditions, sulfur atoms in the hcp-hollow sites are always brighter (higher) in the topographic images than the those in the fcc-hollow site. This could be due to an actual height difference for the adatoms in the fcc- and the hcp-hollow sites as in the case of Ru(0001)+c(4x2)-2S, where LEED analysis finds S at the fcc-hollow site sits 0.04 Å higher than the hcp-hollow site. However, it could be due to an electronic effect, as observed for Rh(111)+c(4x2)-2S [16], in which case no height difference between S at fcc- and hcp-hollow sites was found by LEED [17]. While (2x2) and ($\sqrt{3}$x$\sqrt{3}$)R30° structures are quite common for S overlayers on fcc(111) and hcp(0001) metal surfaces at 1/4 and 1/3 ML, respectively, there is a great variety of structures at higher coverages, depending on the substrate metal. One factor that may be important is the degree to which hollow sites of an other type can be occupied (e.g. hcp-hollow sites on an fcc surface). Thus, on Re(0001) only hcp-hollow sites are occupied in several structures up to the maximum coverage of 1/2 ML (in fact, on this surface clustering into trimers, tetramers and hexamers occur). On Rh(111) [17, 18] and

Ru(0001) [19], a c(4x2) structure forms at 1/2 ML with a 1:1 occupation of fcc- and hcp-hollow sites. On Pt(111), as we report here, a c(7x$\sqrt{3}$)rect structure forms at 3/7 ML (0.43 ML) with a 2:1 occupation of fcc- and hcp-hollow sites. In fact, in this case, if one requires an ordered structure at about this coverage with about this ratio of site occupations, only the c(7x$\sqrt{3}$)rect arrangement is possible; other arrangements lead to much different coverages or different relative site occupations. Moreover, as Figure 6.4 shows, the c(7x$\sqrt{3}$)rect can be viewed as a combination of ($\sqrt{3}$x$\sqrt{3}$)R30° and c(4x2) unit cells, which are relatively simple structures at lower (1/3 ML) and higher (1/2 ML) coverages: the c(4x2) regions thus form heavy domain walls between lower-density ($\sqrt{3}$x$\sqrt{3}$)R30° regions (a heavy domain wall is viewed as having a higher density than can be accounted for only a mismatch between domains). The formation of heavy domain walls have been also found in sulfur on Ru(0001) surface [12]. Adsorption of additional sulfur atoms to the ($\sqrt{3}$x$\sqrt{3}$)R30° phase results in the formation of domain walls. These walls repel each other at coverages $0.33 < \theta < 0.5$ ML and form a long range ordered phase of striped heavy domain walls. At 0.43 ML coverage, the distance between these domain walls is the 3.5 times the lattice distance, in which sulfur atoms in hcp-hollow sites forms ($\sqrt{3}$x$\sqrt{3}$)R30° phase and it is separated by fcc-hollow site sulfur atoms forming heavy domain walls. This structure is analogous to our c(7x$\sqrt{3}$)rect structure. In the case of Pt(111), the coverage only goes up to 0.43 ML, while on Ru(0001) the coverage of sulfur can exceed over 0.43 ML to form a c(4x2) overlayer.

6.5 Conclusions

We studied three ordered overlayers of sulfur on Pt(111) using STM. Our STM studies at low coverage indicate that there is an attractive interaction between adsorbed sulfur atoms on the surface when separated by twice the Pt lattice parameter. As the coverage of the sulfur atoms increases above 0.33 ML, sulfur starts to occupy hcp-hollow sites. In the c(7x$\sqrt{3}$)rect-3S overlayer, there is one sulfur in the hcp-hollow site and two sulfur atoms on the fcc-hollow sites in the unit cell.

Chapter 6 References

1. P.R. Watson, M.A. Van Hove, and K. Hermann, *NIST Surface Structure Database ver. 2.0,*. NIST Standard Reference Data Program. 1995, Gaithersburg, MD.
2. D. Bürgler, G. Tarrach, T. Schaub, R. Wiesendanger, and H.-J. Güntherodt, Phys. Rev. B, 1993. **47**: p. 9963.
3. P. Sautet, J. Dunphy, D.F. Ogletree, and M. Salmeron, Surf. Sci., 1993. **295**: p. 347.
4. P. Sautet and M.-L. Bocquet, Surf. Sci. Lett., 1994. **304**: p. L445.
5. K. Motai, T. Hashizume, H. Lu, D. Jeon, T. Sakurai, and H.W. Pickering, Appl. Surf. Sci., 1993. **67**: p. 246.
6. J.C. Dunphy, P. Sautet, D.F. Ogletree, and M.B. Salmeron, J. Vac. Sci. Technol. A, 1993. **11**: p. 1975.
7. J.G. Forbes, A.J. Gellman, J.C. Dunphy, and M. Salmeron, Surf. Sci., 1992. **279**: p. 68.
8. L. Ruan, I. Stensgaard, F. Besenbacher, and E. Lægsgaard, .
9. B.J. McIntyre, P. Sautet, J.C. Dunphy, M. Salmeron, and G.A. Somorjai, J. Vac. Sci. Technol. B, 1994. **12(3)**: p. 1751.
10. D.F. Ogletree, R.Q. Hwang, D.M. Zeglinski, A.L. Vazquez-de-Parga, G.A. Somorjai, and M. Salmeron, J. Vac. Sci. Technol. B, 1991. **9**: p. 886.
11. D. Heuer, T. Müller, H. Pfnür, and U. Kohler, Surf. Sci., 1993. **297**: p. L61.
12. T. Müller, D. Heuer, H. Pfnür, and U. Kohler, Surf. Sci., 1996. **347**: p. 80.

13. J.C. Dunphy, P. Sautet, D.F. Ogletree, and M.B. Salmeron, J. Vac. Sci. Technol. A, 1993. **11**: p. 2145.

14. W. Heegemann, K.H. Meister, E. Bechtold, and K. Hayek, Surf. Sci., 1975. **49**: p. 161.

15. J.C. Dunphy, P. Sautet, D.F. Ogletree, O. Dabbousi, and M.B. Salmeron, Phys. Rev. B, 1993. **47**: p. 2320.

16. J. Cerdá, H.A. Yoon, G.A. Somorjai, M.A. Van Hove, and M. Salmeron, to be published.

17. K.C. Wong, W. Liu, M. Saidy, and K.A.R. Mitchell, Surf. Sci., 1996. **345**: p. 101.

18. P.C. Wong, M.Y. Zhou, K.C. Hui, and K.A.R. Mitchell, Surf. Sci., 1985. **163**: p. 172.

19. C. Schwennicke, D. Jürgens, G. Held, and H. Pfnür, Surf. Sci., 1994. **316**: p. 81.

Chapter 7

Coverage dependency of overlayer structures:

II. Surface structures of sulfur on Rh(111)

7.1 Introduction

The coverage and structures of sulfur on Rh(111) has been investigated earlier by low energy electron diffraction where four ordered LEED patterns were observed [1]. The detailed structures of the ($\sqrt{3}$x$\sqrt{3}$)R30°-S and the c(4x2)-2S have been also carried out using tensor LEED analysis [2, 3]. However, the detailed phase diagram of the sulfur on Rh(111) is still unknown as well as the structures for the (4x4) and (7x7) surface overlayers. In this study, we carried out AES, LEED and STM experiments to elucidate the sulfur-sulfur as well as the sulfur-rhodium interactions thorough the change in overlayer structures due to overcrowding of sulfur. We report here the phase diagram of sulfur on Rh(111) surface with AES and LEED, and propose the model structures for ($\sqrt{3}$x$\sqrt{3}$)R30°-S, c($\sqrt{3}$x7)rect-3S, c(4x2)-2S, (4x4)-8S and (7x7)-35S surface overlayers based on out coverage measurements and STM experiments.

7.2 Experiments

The sample was cleaned by repeated cycles of argon ion bombardment and annealing in oxygen or in vacuum until no impurities could be detected by AES. The sample was heated with electron bombardment heater and the temperature was measured with pyrometer (IRCOM) calibrated against type K thermocouple.

A solid-state electrochemical source was utilized for sulfur deposition [4]. Sulfur was deposited at room temperature, then the sample was heated up to 1300 K to produce the ordered structures as seen by LEED patterns in Figure 7.1. The peak-to-peak height of sulfur at 152 eV and rhodium at 304 eV were compared to get the relative coverage of sulfur on Rh(111) surface. The STM experiments were performed after obtaining the desired LEED patterns associated with ($\sqrt{3}$x$\sqrt{3}$)R30°, c(4x2), (4x4) and (7x7) surface overlayers.

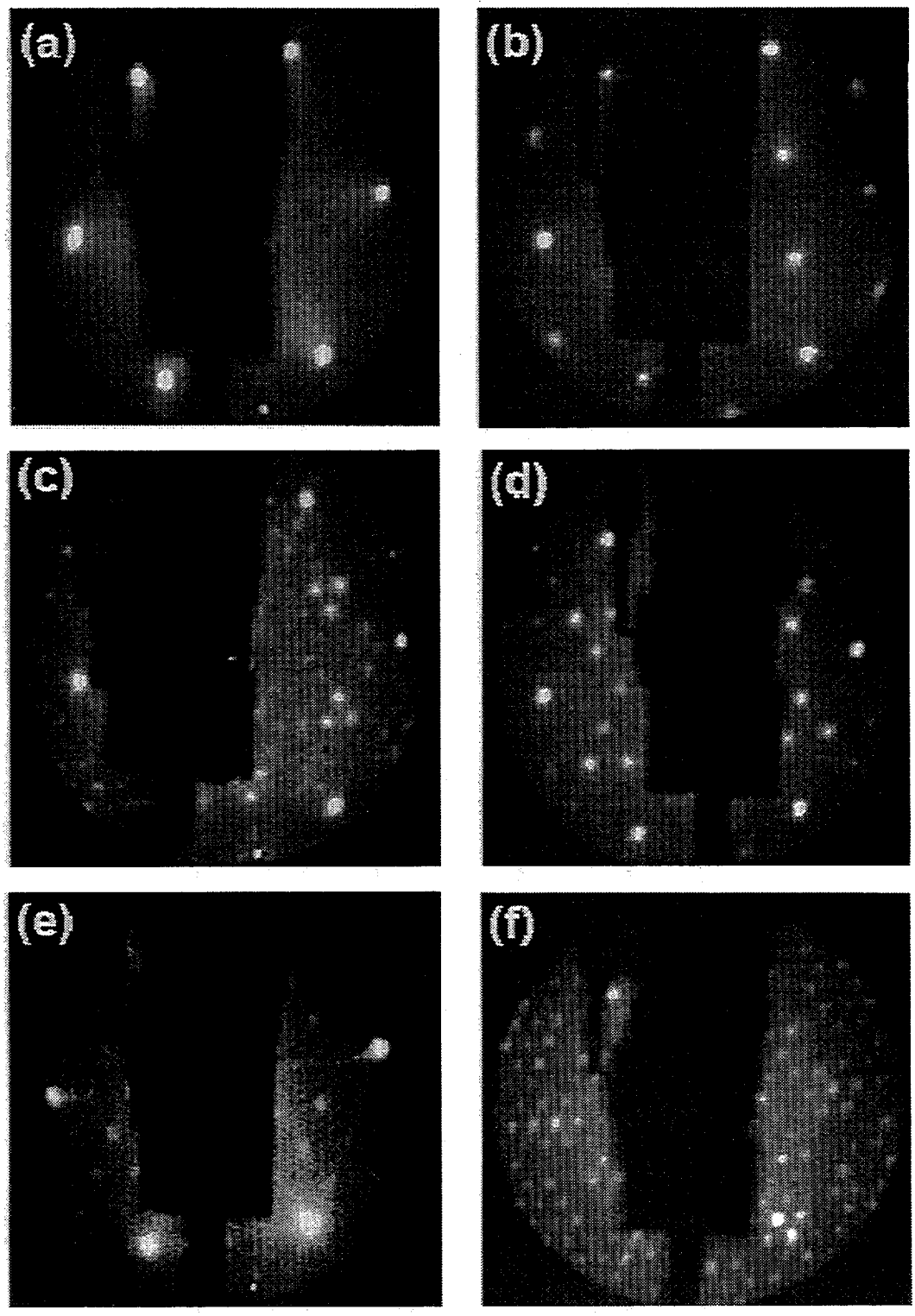

Figure 7.1 The LEED patterns of clean and different ordered sulfur overlayer taken at incident energy of 132 eV: (a) clean Rh(111); (b) ($\sqrt{3}$x$\sqrt{3}$)R30°; (c) c($\sqrt{3}$x7)rect; (d) c(4x2); (e) (4x4) ; and (f) (7x7) overlayers

7.3 AES and LEED analysis

When sulfur was deposited on Rh(111) surface at room temperature, no apparent sharp ordered LEED pattern is observed. Upon the annealing of the sample, sharp LEED patterns of ($\sqrt{3}$x$\sqrt{3}$)R30°, c($\sqrt{3}$x7)rect, c(4x2), (4x4) and (7x7) were produced. Auger electron spectroscopy was taken with electron beam at glancing angle. Incident energy of 2 keV was used and Auger signal was collected with a retarding field analyzer. The highest coverage (7x7) structure can be formed either by adsorbing excess sulfur which forms disordered overlayer then anneal at the temperature up to 750 K or by adsorbing more sulfur to ($\sqrt{3}$x$\sqrt{3}$)R30° or c(4x2) overlayers followed by annealing. The sulfur source we use mainly produces S_2, thus further annealing is needed to dissociate S_2 for atomic sulfur to chemisorb on the surface. From the disordered phase or (7x7) overlayer, other structures can be produced upon annealing of the sample. When the excess sulfur desorbs with gentle annealing (below 900 K), the c(4x2) ordered overlayer is formed. When the sample was heated to 1000 K, the (4x4) ordering can be observed. The relative Auger intensity of sulfur into rhodium in the (4x4) overlayer does not change from that of the c(4x2) overlayer. This indicates that these two ordered structures have thermodynamically the same energy level, but separated by some kinetic barrier. The c(4x2) structure can also be made by adsorbing sulfur on c($\sqrt{3}$x7)rect or ($\sqrt{3}$x$\sqrt{3}$)R30° overlayer. The c($\sqrt{3}$x7)rect structure is found when sulfur desorbs from the c(4x2) or adsorbs on the ($\sqrt{3}$x$\sqrt{3}$)R30° overlayer. The ($\sqrt{3}$x$\sqrt{3}$)R30° structure is most stable, formed over the temperature range of 650 to 1250 K. The ($\sqrt{3}$x$\sqrt{3}$)R30° structure is

formed by adsorbing sulfur to clean Rh(111) surface followed by annealing or by desorbing sulfur from any of the structures with higher sulfur concentration. The formation of each structure is summarized in Figure 7.2. The + S_2 indicates adsorbing S_2 to the surface, and A denotes the annealing of the sample. Arrows indicate the direction of the reaction. Series of Auger electron spectra were taken as a function of sulfur coverage. Figure 7.3 is a Auger electron spectrum corresponding to Rh(111)+($\sqrt{3}$x$\sqrt{3}$)R30° overlayer. The phase diagram was made based on the relative Auger intensities of sulfur 152 eV peak to rhodium 304 eV peak and the annealing temperature as illustrated in Figure 7.4. Based on the coverage of ($\sqrt{3}$x$\sqrt{3}$)R30° overlayer (1/3 ML) determined by the previous tensor LEED analysis, the coverage of sulfur on the other ordered overlayer can de obtained, assuming linear response of Auger intensity. The c($\sqrt{3}$x7)rect structure is produced at 3/7 ML (monolayer, defined as the number of sulfur atoms per (1x1) unit cell of rhodium substrate). The c(4x2) and the (4x4) structures are formed at ½ ML and the (7x7) overlayer has 5/7 ML coverage of sulfur.

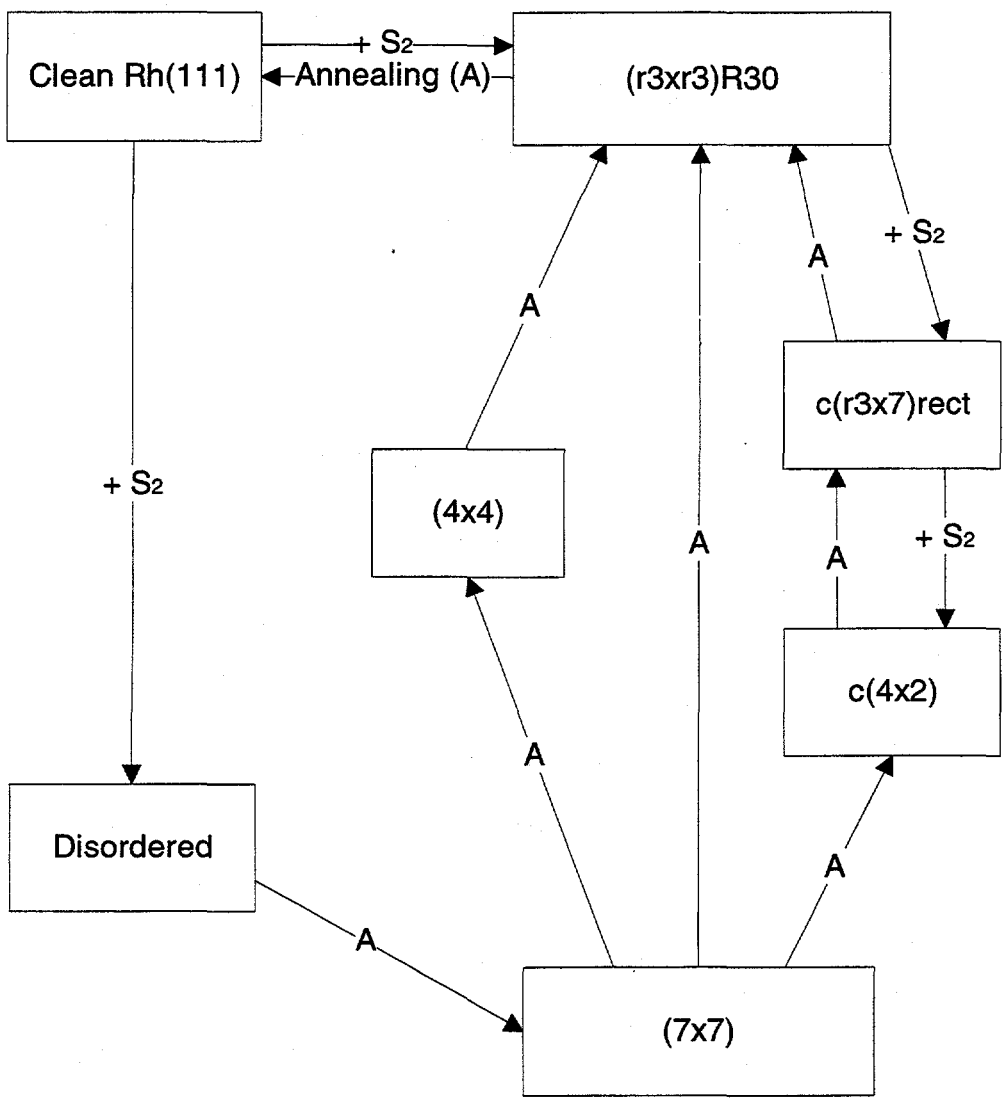

Figure 7.2 Flow-chart diagram of the formation of the different ordered overlayer of sulfur on Rh(111). S_2 denotes the adsorbing of S_2 to the surface and A (anealing) indicates the annealing of the sample to desorb sulfur.

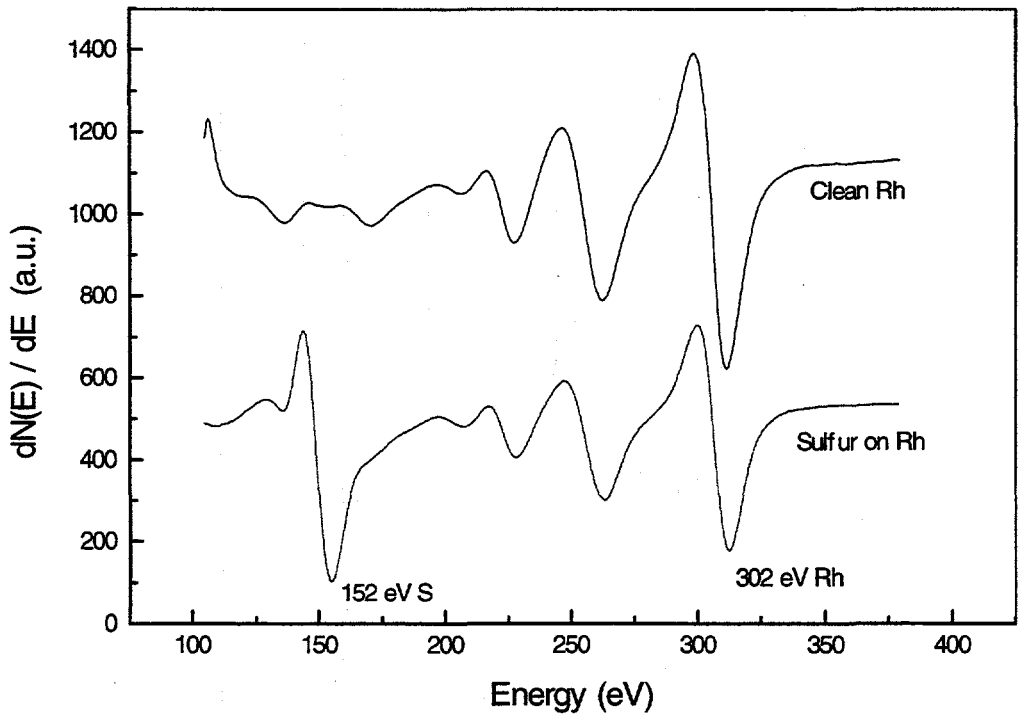

Figure 7.3 Auger Electron Spectra of clean Rh surface and Rh surface with sulfur forming ($\sqrt{3}x\sqrt{3}$)R30°-S structure.

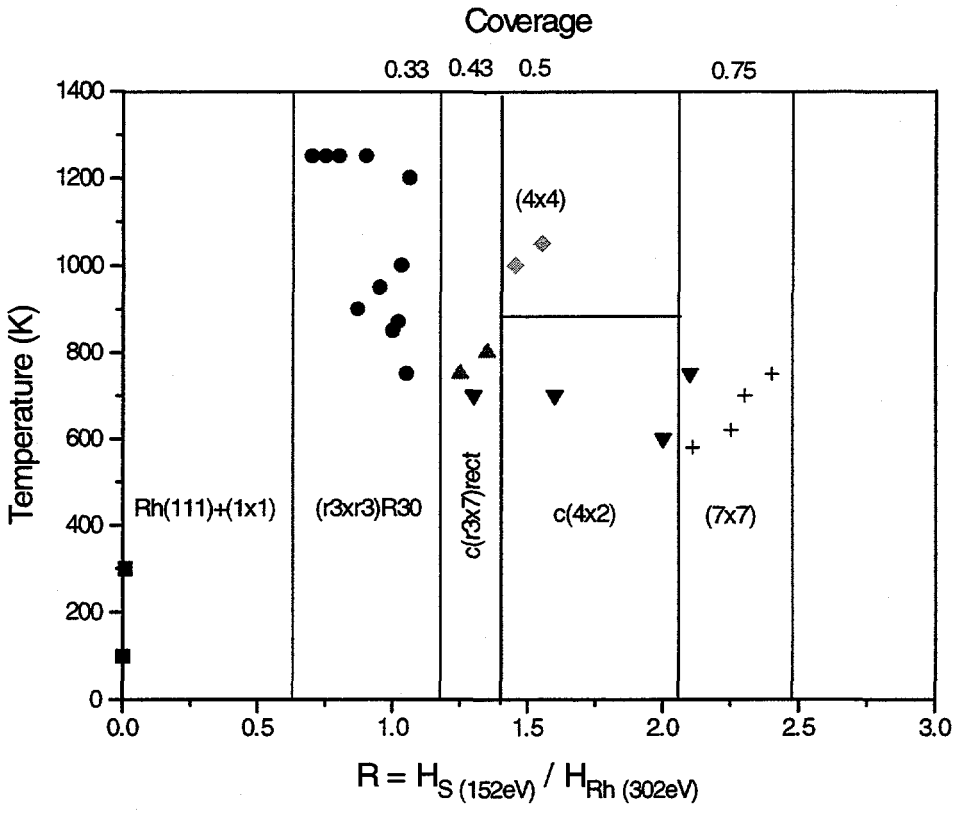

Figure 7.4 Phase diagram of sulfur on Rh(111) based on Auger intensity analysis.

7.4 STM analysis

7.4.1 The ($\sqrt{3}$x$\sqrt{3}$)R30° Structure

When the sharp LEED pattern was formed, the sample was then transferred to the STM. Current mode images are shown in Figure 7.5. These were taken at a sample bias of 50 mV and a tunneling current set point varying from 3.23 nA to 8.20 nA. The bright spots are assigned as sulfur, based on the existence of single atom vacancies in the images. The corrugation of the sulfur atoms in the image is about 1.8 nA. No significant differences in the images were observed with change in the gap resistance. Images taken at the different tunneling current have the same spherical shape of sulfur with slight different corrugation (the corrugation of sulfur varies from 0.9 to 2.3 nA). The structure of the ($\sqrt{3}$x$\sqrt{3}$)R30° overlayer is obtained from the previous tensor LEED analysis and our STM analysis as shown in Figure 7.6.

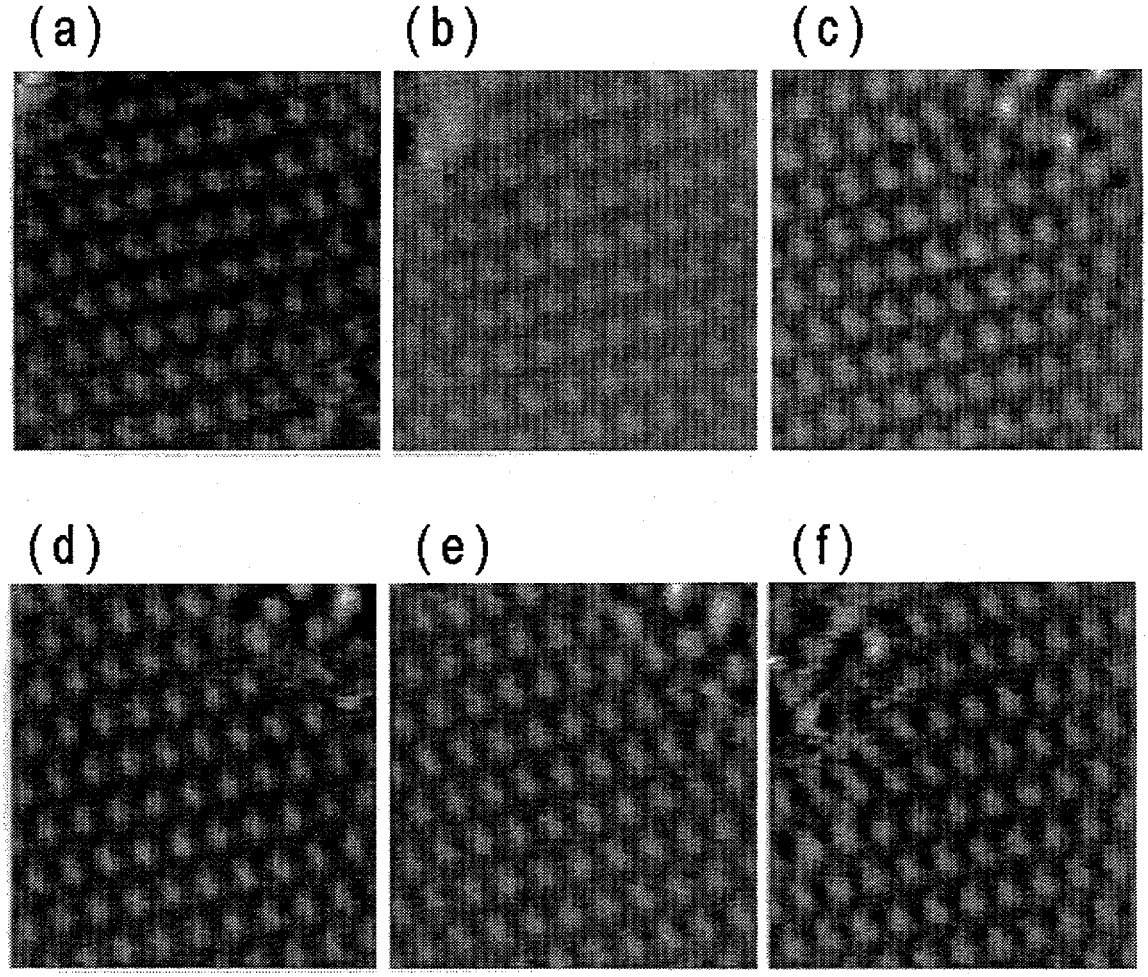

Figure 7.5 STM images of Rh(111)-($\sqrt{3}$x$\sqrt{3}$)R30° overlayer at different current set-points in current mode. These images were taken at 50 mV of bias while the gap resistance was changed from 15.1 to 5.95 MΩ. (a) 15.1 (b) 11.8 (c) 9.39 (d) 8.58 (e) 7.80 (f) 5.95 MΩ.

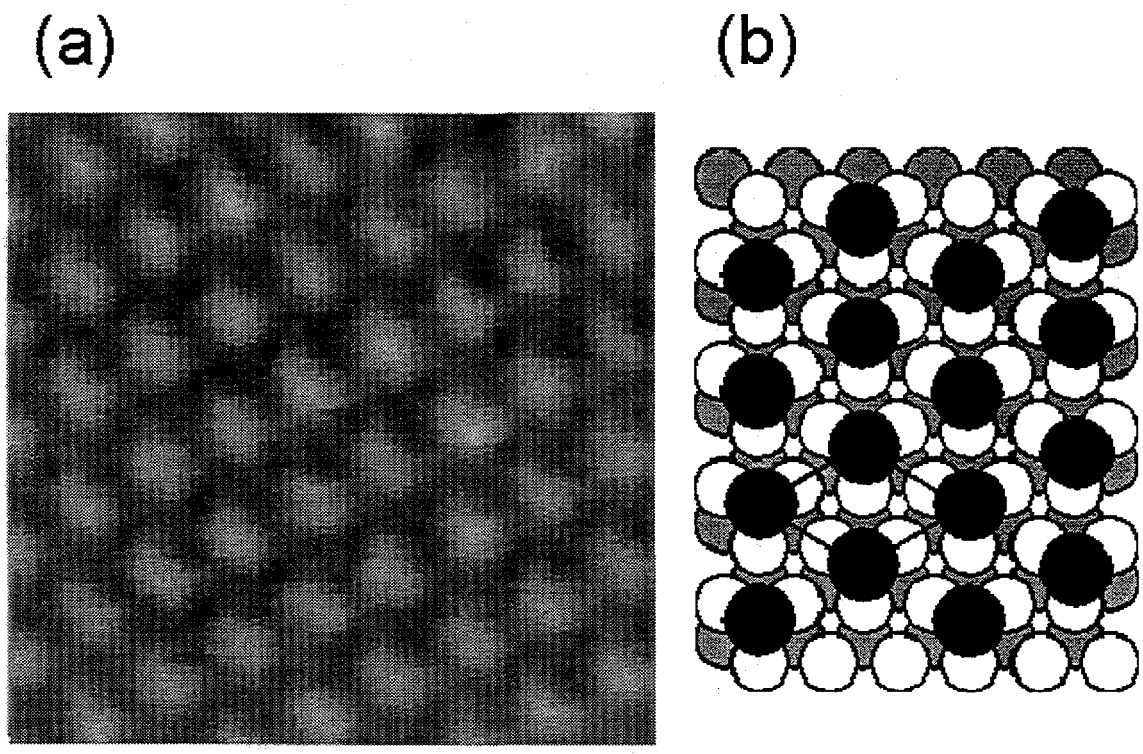

Figure 7.6 An STM image of Rh(111)-($\sqrt{3}$x$\sqrt{3}$)R30° overlayer (a) and its model structure (b). Sulfur has been assigned to the fcc-hollow sites based on the previous tensor LEED analysis.

7.4.2 The c(4x2) Structure

The c(4x2) overlayer structure is imaged in topographic mode. Figure 7.7 is the image taken at 1 nA and the sample bias voltage varying from -200 mV to +250 mV. Single atom vacancies are also observed (i.e. bottom corner in Figure 7.8(f)). We assign each protrusion to the sulfur atom. Two sulfur atoms imaged in the unit cell with different height. The difference is between 0.2 to 0.4 Å depending on the sample bias voltage. The difference in the height of the two sulfur atoms is clearly shown in the three dimensional STM image of c(4x2) overlayer as shown in Figure 7.7. Series of topographic images with different gap resistance are shown in Figure 7.8. Since the fcc sites are most stable in low coverage structures, we have assigned one of two protrusions as the sulfur adsorbed on the fcc sites. The (1x1) grid is superimposed on Figure 7.9 where the corrugation difference is largest. The corners of triangle indicates the fcc-hollow sites. When we extrapolate the site, the sulfur atoms with higher corrugation do not fit onto the (1x1) grid. Rather, these sulfur atoms lie in the middle of rhombus suggesting hcp-hollow site adsorption. It is not clear from our experiments which sulfur atom (hcp or fcc) has higher corrugation in the images. The suggested model for c(4x2) structure with sulfur atoms in both fcc- and hcp-hollow sites as shown in Figure 7.10.

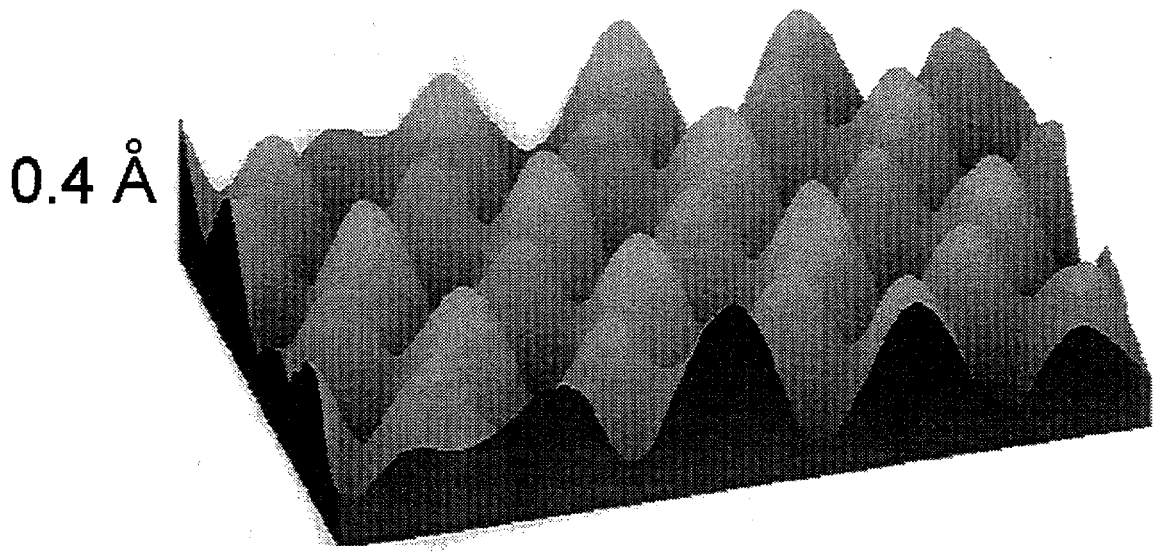

Figure 7.7 The 3 dimensional (3D) image of c(4x2) structure. The total corrugation of the image is 0.4Å, the height difference between two sulfur atoms in 0.15 Å.

Figure 7.8 (following page) Series of topographic images of c(4x2) sulfur overlayer. These images were taken at 1 nA of current with varying bias voltage. A point defect can be seen at the bottom corner of (f).
The bias voltages are; (a) -200 mV, (b) -150 mV, (c) 100 mV, (d) 120 mV, (e) 140 mV and (f) 250 mV

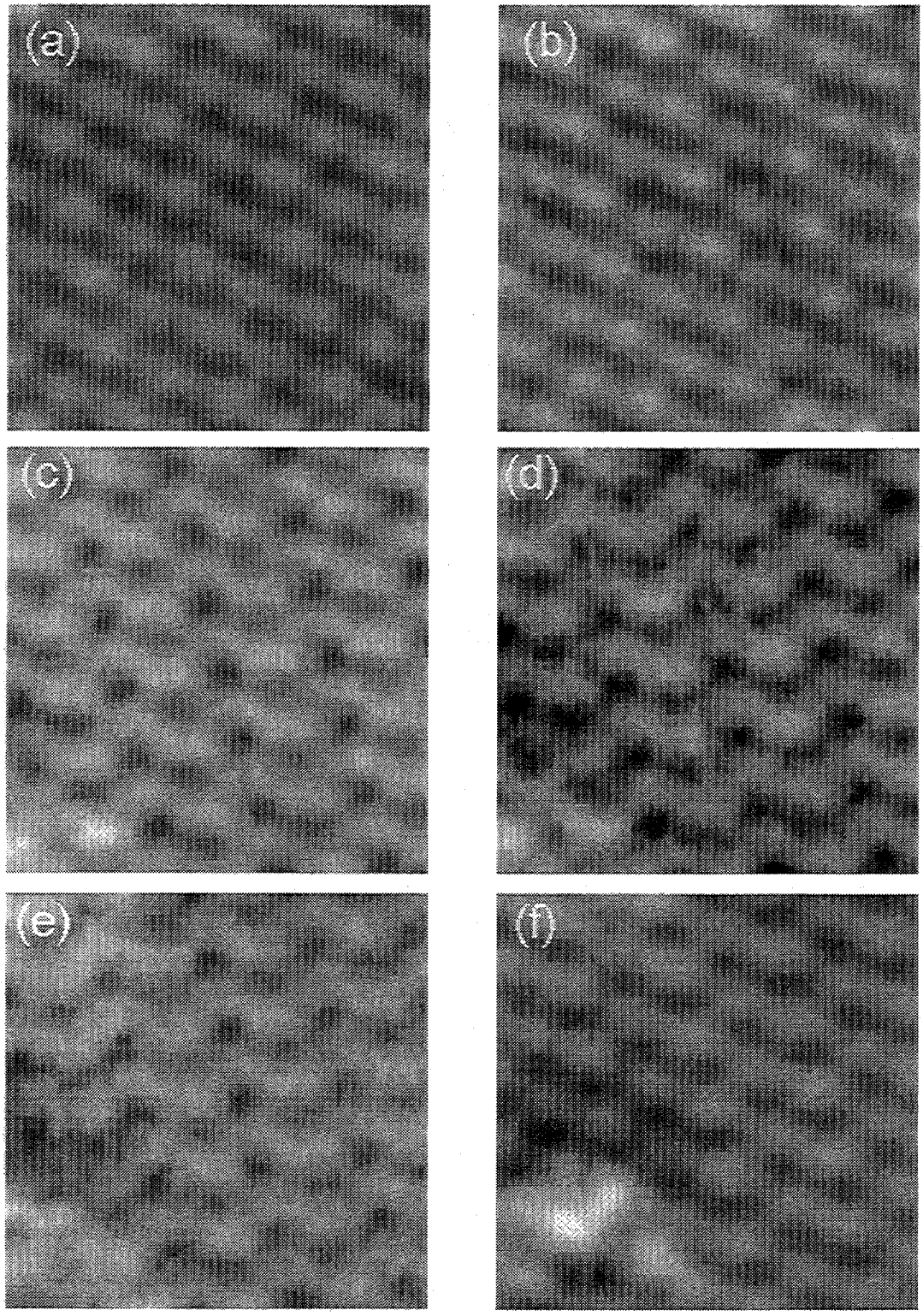
(a)
(b)
(c)
(d)
(e)
(f)

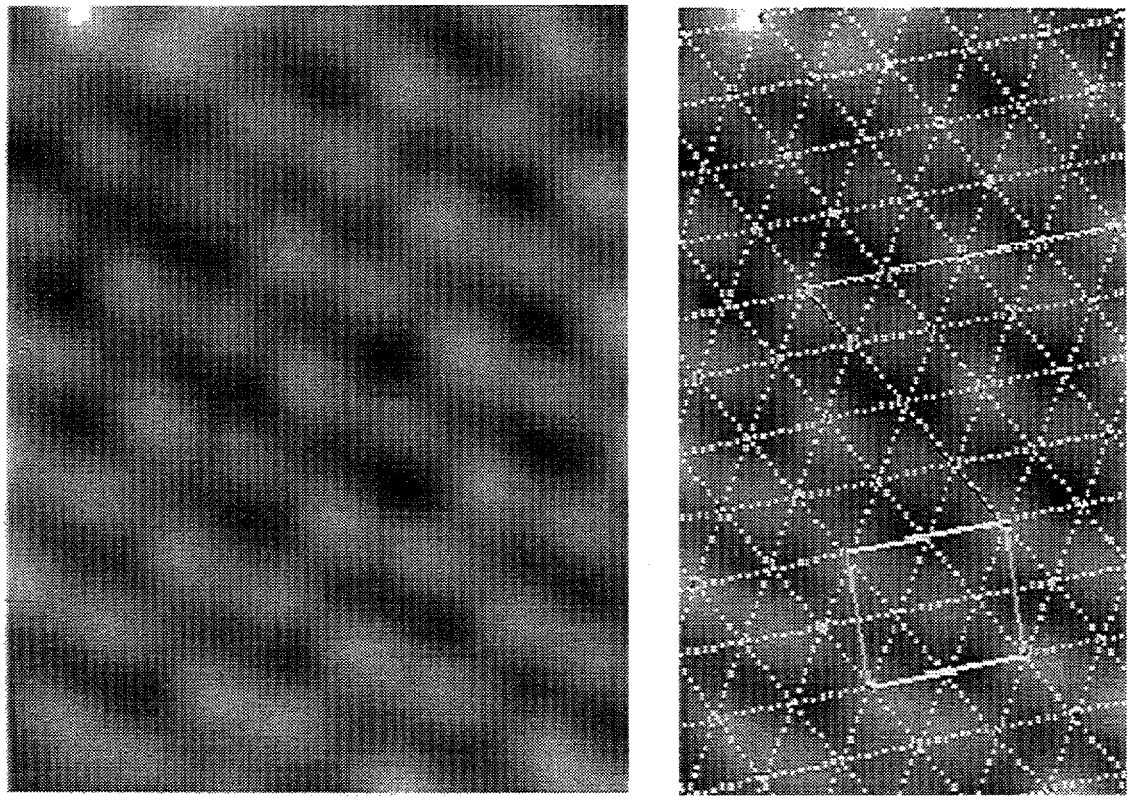

Figure 7.9 A topographic image of c(4x2) overlayer taken at 1 nA and 200 mV, and (1x1) grid is superimposed on the section of this image, assuming the sulfur atom with the higher corrugation as the sulfur on fcc-hollow site. The other sulfur atom does not fit to the (1x1) grid. The other sulfur atom was determined to be adsorbed on the hcp-hollow site.

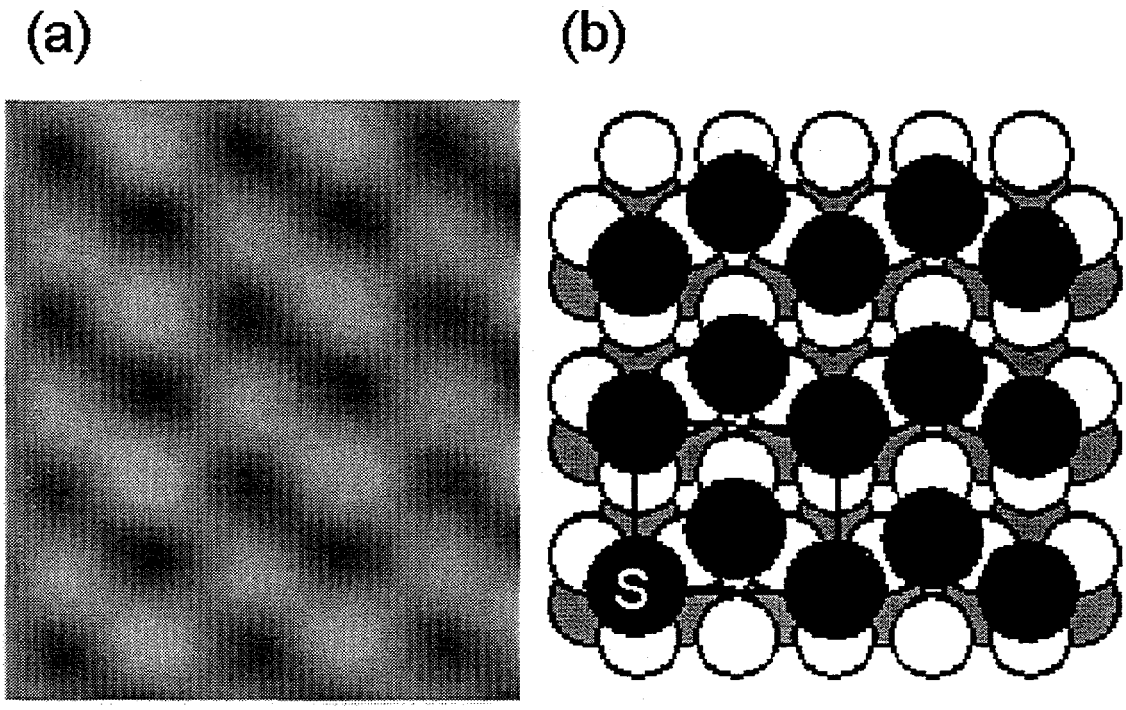

Figure 7.10 A topographic image of c(4x2) overlayer (a) and its model structure. In the model, there is one sulfur atom in the fcc-hollow site and the other atom in the hcp-hollow site. The STM image clearly shows the difference in the corrugation between these two sulfur atoms. However, from this image alone, it is not possible to distinguish the difference in the adsorption sites of these two sulfur atoms.

7.4.3 The (4x4) Structure

The (4x4) overlayer was formed when the sulfur covered surface was annealed to 700 K. The images were taken in current mode with the sample bias varying from 0.7 to150 mV as seen in Figures 7.11 and 7.12. In these images, the sulfur atoms are also imaged as protrusions. Images have two-fold symmetry with two mirror planes. Figure 12(a) is a current image taken at 0.7 mV with tunneling current of 5.91 nA. There are 8 sulfur atoms imaged in a unit cell, making the coverage of 0.5 ML, which is in good agreement with Auger electron spectroscopy results shown earlier. When we overlay the 1x1 grid over this image with the cross to the isolated sulfur atom, all the sulfur atoms are located on the grid as shown in Figure 7.12 (b). This indicates that all the sulfur atoms in the unit cell have the same adsorption sites. Since it was shown that the fcc sites are favored for sulfur atom on fcc metal surfaces, the model for the (4x4) structure is proposed with all the sulfur atoms adsorbed on the fcc sites as shown in Figure 13.

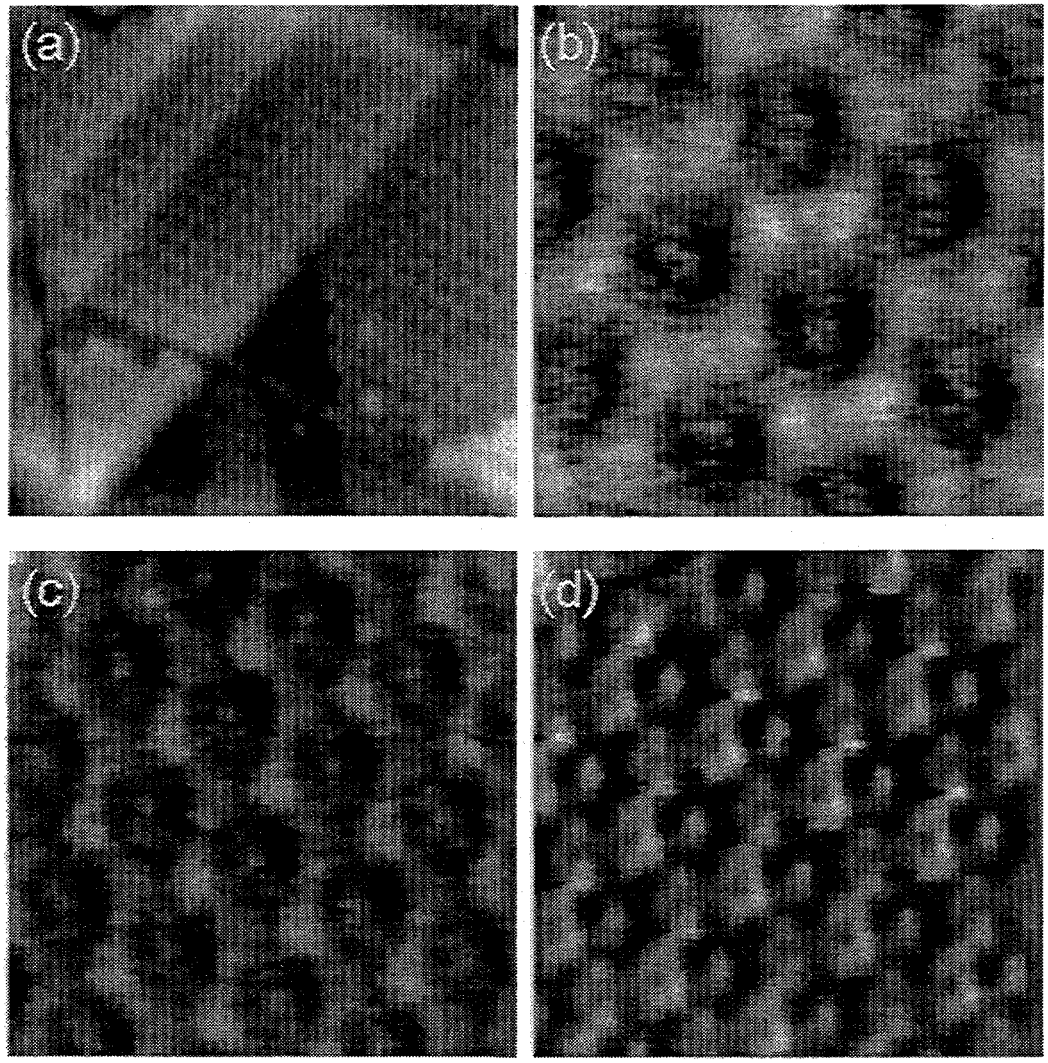

Figure 7.11 Current mode images of Rh(111)+(4x4) sulfur overlayer. (a) 180 Å x 180 Å area image taken at 1 nA and 180 mV of bias. The surface is uniformly covered with honeycomb structures. (b) An image (30 Å x 30 Å) taken at 1 nA and 400 mV of bias showing honeycomb details. (c) 40 Å x 40 Å area image taken at 4.0 nA and 150 mV of bias. The structure of the honeycomb is resolved. (d) 40 Å x 40 Å area image taken at 5.9 nA and 0.7 mV of bias. Now all the details in the honeycombs are resolved. The image appears to have two-fold symmetry.

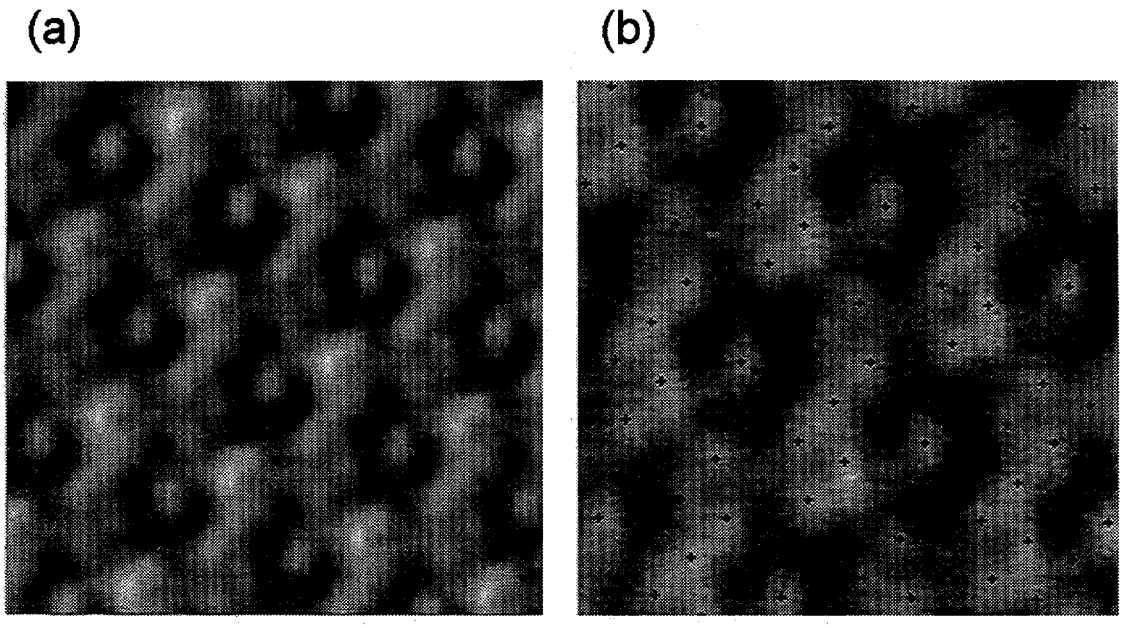

Figure 7.12 (a) A current image of (4x4) overlayer with high resolution. This image was taken at 5 nA of current and 0.7 mV of bias. (b) A section of (a) with (1x1) grid superimposed on the image. There are 8 sulfur atoms imaged and all the sulfur atoms have the same adsorption site.

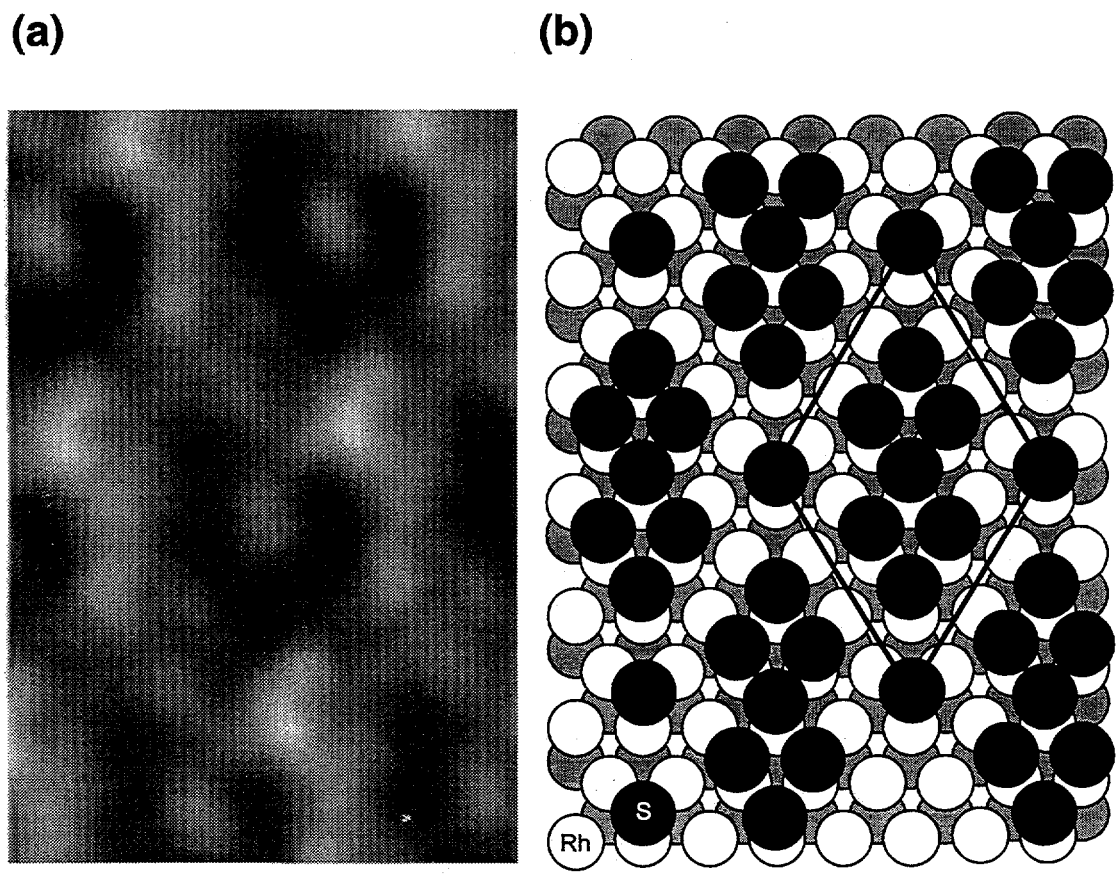

Figure 7.13 The STM image (a) and the model structure (b) of Rh(111)+(4x4)-8S overlayer base on the STM images. Notice the spacing between sulfur atoms in the $[\bar{1}2\bar{1}]$ direction is $\sqrt{3}$ times the substrate lattice.

7.4.4 The (7x7) Structure

With the highest coverage of sulfur, the (7x7) ordered overlayer is imaged in topographic mode. Figure 7.14 (a) is taken at 1 nA tunneling current and 100 mV sample bias voltage. This image shows the surface was uniformly covered with (7x7) overlayer. The small area image shows the honey comb features as shown in Figure 7.14 (b). Figures 7.14 (c) and (d) were taken at higher tunneling current (the tip scans closer to the surface). An image taken at a lower gap resistance (Figure 7.14 (b)) shows lower contrast than those taken at higher gap resistance. The features in the honey comb are more visible as shown in Figures 7.14(c) and (d). In the middle of the Figure 7.14 (c), a couple of vacancies were imaged. When the sample bias voltage was varied from -50 mV to +80 mV, no change in the image is observed as seen in Figures 7.15 (a), (b) and (c). This could indicate that when the tunneling gap increases the overlap between the tip and the surface is weakened. At higher sample bias voltage (± 150 mV) images also lose contrast. When the tip is brought closer to the surface, the tip may push the sulfur atoms around thus lowering the contrast of the image. Based on our AES analysis, the coverage of sulfur is close to 5/7 ML in the (7x7) overlayer. This suggests multiple adsorption sites for sulfur or the formation of surface sulfide. We examined three known rhodium sulfides- RhS_2, $Rh_{17}S_{15}$ and Rh_4S_3. However, the detailed structure of the (7x7) overlayer of sulfur on Rh(111) has not been

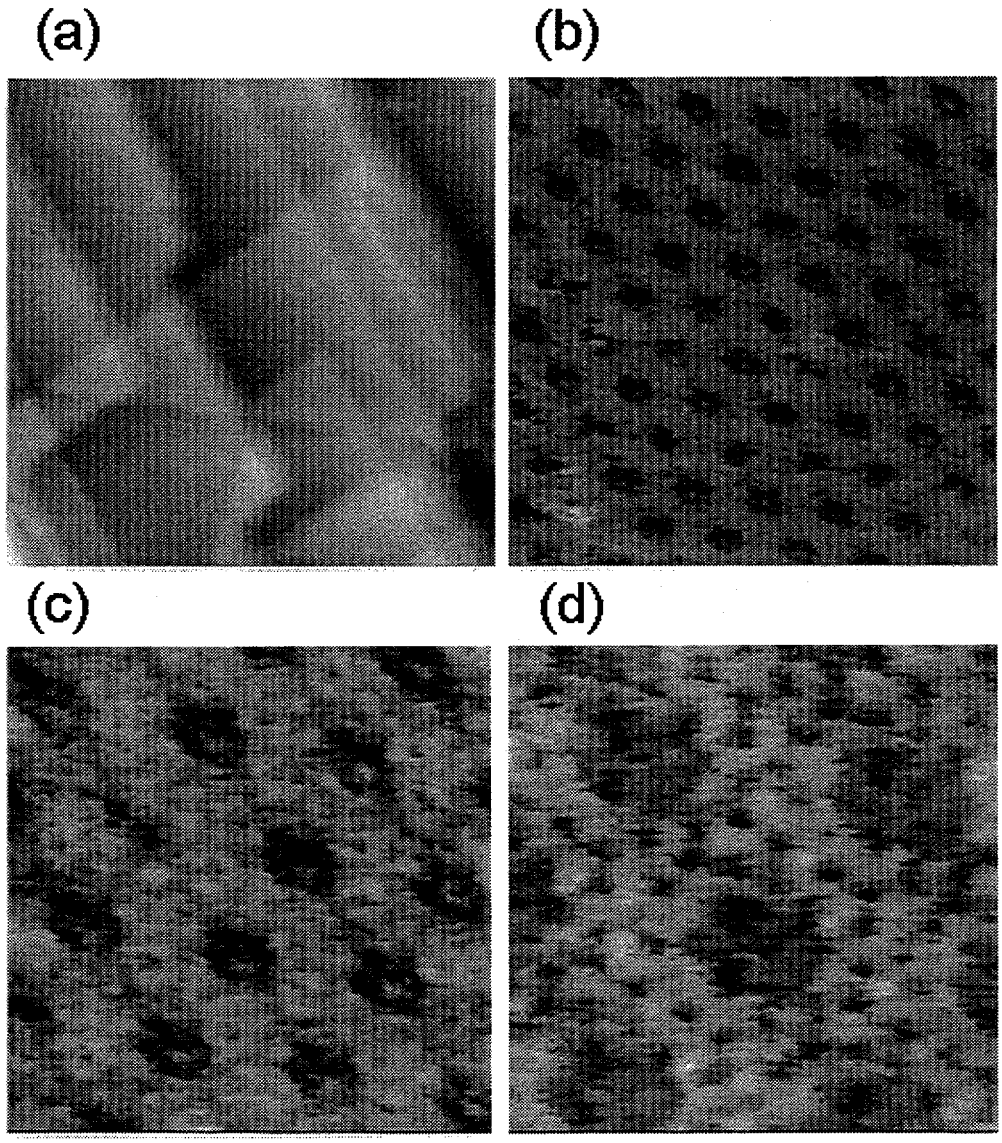

Figure 7.14 Topographic images of Rh(111)+(7x7) overlayer. (a) 400 Å x 400 Å image taken at 100 mV, 1 nA; (b) 130 Å x 130 Å image taken at 150 mV, 1 nA; (c) 60 Å x 60 Å image taken at 150 mV, 1 nA; (d) 30 Å x 30 Å image taken at 75 mV, 1 nA

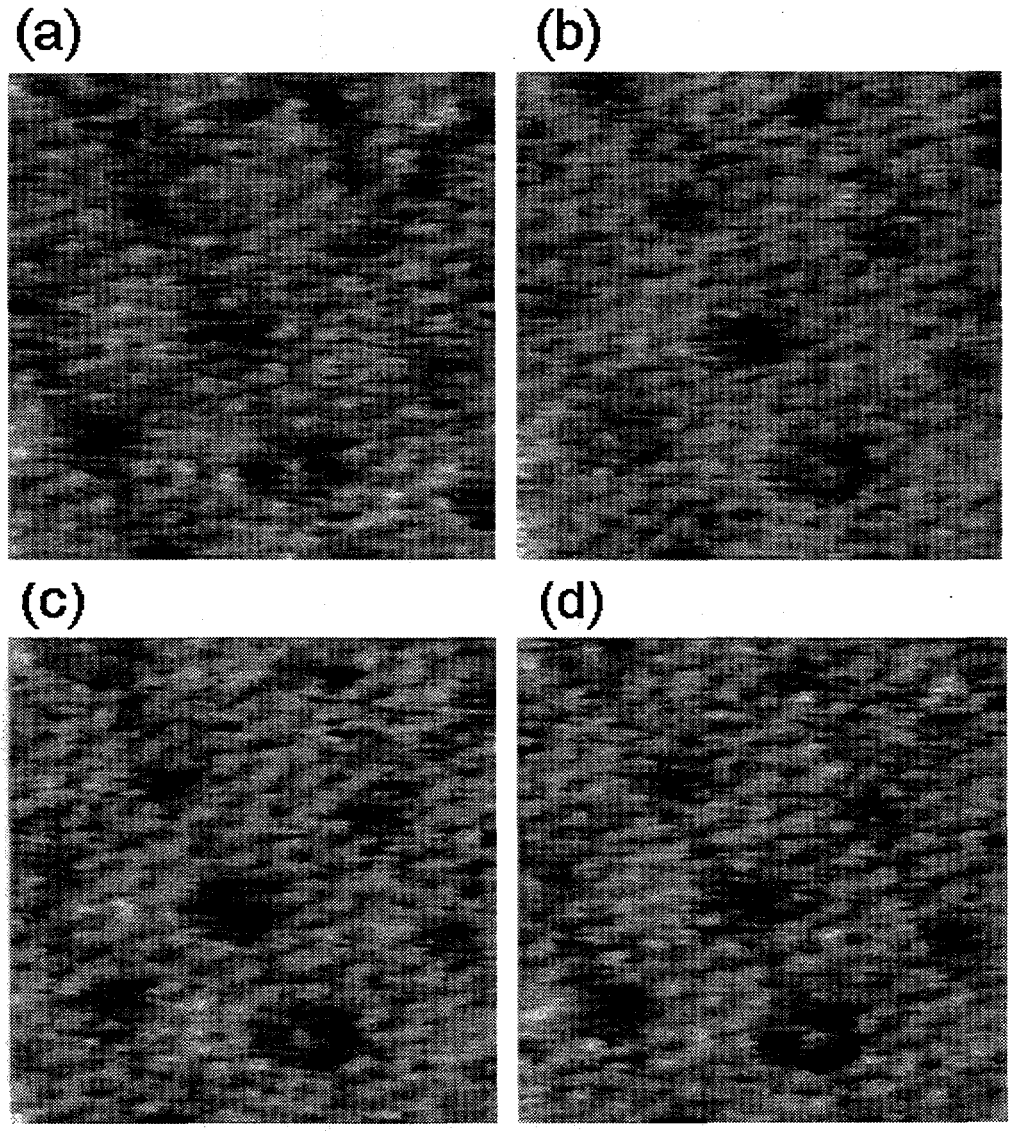

Figure 7.15 (a) Topographic images (60 Å x 60 Å) of (7x7) overlayer taken at 100 mV and 1 nA; Series of topographic image (42 Å X 42Å) taken at 1 nA and -50 mV (b), 50 mV (c) and 80 mV (d).

7.5 Discussion

Five different ordered overlayers of sulfur have been observed. AES and LEED analysis shows that these ordered overlayers form at different sulfur coverages. Based on the previous LEED [3, 5] and AES [1] experiments, which clearly indicate 1/3 ML for $(\sqrt{3}x\sqrt{3})R30°$ structure, we can extrapolate the coverage for the other ordered overlayers. For $c(\sqrt{3}x7)$rect structure, the coverage is close to 0.43 (3/7) ML, and for c(4x2) and (4x4) overlayers, the sulfur coverage turns out to be 0.5 ML. Unlike Pt(111) on which the sulfur coverage does not exceed 0.43 ML, the sulfur coverage on Rh(111) exceeds 0.5 ML. For (7x7) overlayer, the coverage of sulfur is found to be about 0.75 ML.

Our STM images show one maximum for each sulfur atom for the $(\sqrt{3}x\sqrt{3})R30°$ and c(4x2) structures (as shown in Figures 7.6(a) and 7.10(a)). Topographic images for the c(4x2)-2S overlayer indicate that both fcc- and hcp-hollow sites are occupied by sulfur atoms. Under our experimental conditions, we could not distinguish which sulfur atoms adsorb in the hcp-hollow sites. The height difference between these sulfur atoms in fcc- and hcp-hollow sites varies from 0.2 to 0.4 Å depending on the bias voltage. This could be due to an actual height difference for the adatoms in the fcc- and the hcp-hollow sites or an electronic effect. The tensor LEED calculation on this system (Rh(111)-c(4x2)-2S) indicates that no height difference between S at fcc- and hcp-hollow sites. This is indicative of an electronic effect on the height difference for sulfur adatoms in different adsorption sites. The STM calculation based on EQSC theory has been carried

out for Rh(111)+c(4x2)-2S structure, and shows that the sulfur atom in the hcp-hollow site is imaged higher than that adsorbed in the fcc site [6].

Both ($\sqrt{3}$x$\sqrt{3}$)R30° and c(4x2) structures are quite common for S overlayers on fcc(111) and hcp(0001) metal surfaces at 1/3 and 1/2 ML, respectively. We have reported earlier that on Pt(111) surface, sulfur forms a c($\sqrt{3}$x7)rect structure when sulfur is added to ($\sqrt{3}$x$\sqrt{3}$)R30° overlayer. The LEED pattern associated with the c($\sqrt{3}$x7)rect structure is also observed on Rh(111) surface with 0.43 ML. The coverage of sulfur on c($\sqrt{3}$x7)rect structures on Pt(111) and Rh(111) is identical (3 sulfur atoms in unit cell of 7 substrate atoms). The c($\sqrt{3}$x7)rect-3S structure can be viewed as a mixture of ($\sqrt{3}$x$\sqrt{3}$)R30° and c(4x2) structures. Since we have observed the c(4x2)-2S overlayer on Rh(111) surface with 0.5 ML sulfur coverage, it is very likely that this c($\sqrt{3}$x7)rect-3S structure is the transient ordered structure between the ($\sqrt{3}$x$\sqrt{3}$)R30°-S and the c(4x2)-2S structures. When the sulfur coverage increases on the ($\sqrt{3}$x$\sqrt{3}$)R30°-S overlayer, a 'heavy' domain wall is formed. A heavy domain wall is viewed as having a higher density of sulfur than can be accounted for by only a mismatch between domains. As the sulfur coverage increases further, the number of heavy domain walls also increases. At a certain coverage, the distance between heavy domain walls becomes uniform resulting a formation of c($\sqrt{3}$x7)rect-3S structure. When the sulfur coverage reaches 0.5 ML, the surface is saturated with these heavy domain walls forming the c(4x2) structure. From our STM experiments, sulfur adsorbs both in the fcc- and hcp-hollow site. The model for this transition from the ($\sqrt{3}$x$\sqrt{3}$)R30° structure to c(4x2) structure is illustrated in Figure 7.16. The formation of heavy domain walls have been also found in sulfur on Ru(0001)

surface [7] on which adsorption of additional sulfur atoms to the ($\sqrt{3}$x$\sqrt{3}$)R30° phase results in the formation of domain walls. These walls repel each other at coverages 0.33 $< \theta <$ 0.5 ML and form a long range ordered phase of striped heavy domain walls. At 0.43 ML coverage, the distance between these domain walls is 3.5 times the lattice distance, in which sulfur atoms in hcp-hollow sites forms ($\sqrt{3}$x$\sqrt{3}$)R30°, and at 0.5 ML sulfur atoms occupy both hcp and fcc sites forming c(4x2) overlayer.

The occupation of hcp sites by the S atoms on Rh(111) shows how the overlayer overcomes the repulsive interaction between sulfur atoms due to overcrowding. At low coverage, sulfur prefers to adsorb in the fcc site where it is energetically most favorable. When the sulfur atoms are forced to adsorb exceeding the coverage at which all sulfur atoms occupy the fcc sites, the sulfur atoms start to repel each other. This repulsive interaction is relieved by sulfur adsorption in the hcp-hollow site. Sulfur adsorption in the hcp site is not most favorable, but this hcp adsorption maximizes the distance between the sulfur atoms on the surface. This type of site mixing has been also observed on Ru(0001) [7] and Pt(111) [8]

Our AES experiments show that both c(4x2) and (4x4) overlayers have the same sulfur coverage. This is in disagreement with the previous LEED and AES analysis performed by Foord et. al.. However, their suggested model of RhS formation does not fit to our STM result at all. Rather, STM results confirms our AES results, where 8 sulfur atoms are imaged per unit cell. The sulfur coverage for the (4x4) structure is found to be the same as the c(4x2) overlayer. We have suggested that the repulsive interaction can be relieved by a hcp site adsorption which maximizes the sulfur-sulfur distance on the surface. However, in the case of (4x4)-8S structure, we found that the sulfur atoms are all

adsorbed in fcc sites, and some sulfur-sulfur distance is the same as the substrate lattice spacing. STM images of the Rh(111)+(4x4)-8S show the possible formation of sulfur clusters. The cluster formation of sulfur has been observed on Re(0001) surface. On this surface, sulfur forms clusters of trimers, tetramers and hexamers as the sulfur coverage increases. We conclude from these examples that cluster formation can also lower the repulsive interaction due to overcrowding of sulfur.

Figure 7.17 (Next two pages) Suggested model for transition from the ($\sqrt{3}$x$\sqrt{3}$)R30° structure to c(4x2) structure. When sulfur is added to ($\sqrt{3}$x$\sqrt{3}$)R30° structure (a), the heavy domain wall is formed (b). The sulfur atoms in the heavy domain wall occupy the hcp site. As the sulfur coverage further increases, the number of heavy domain wall also increase. At 0.43 ML, it forms c($\sqrt{3}$x7)rect-3S overlayer (c), and at 0.5 ML it forms c(4x2) overlayer on which there are equal number of sulfur atoms in the hcp site as the fcc site.

(a)

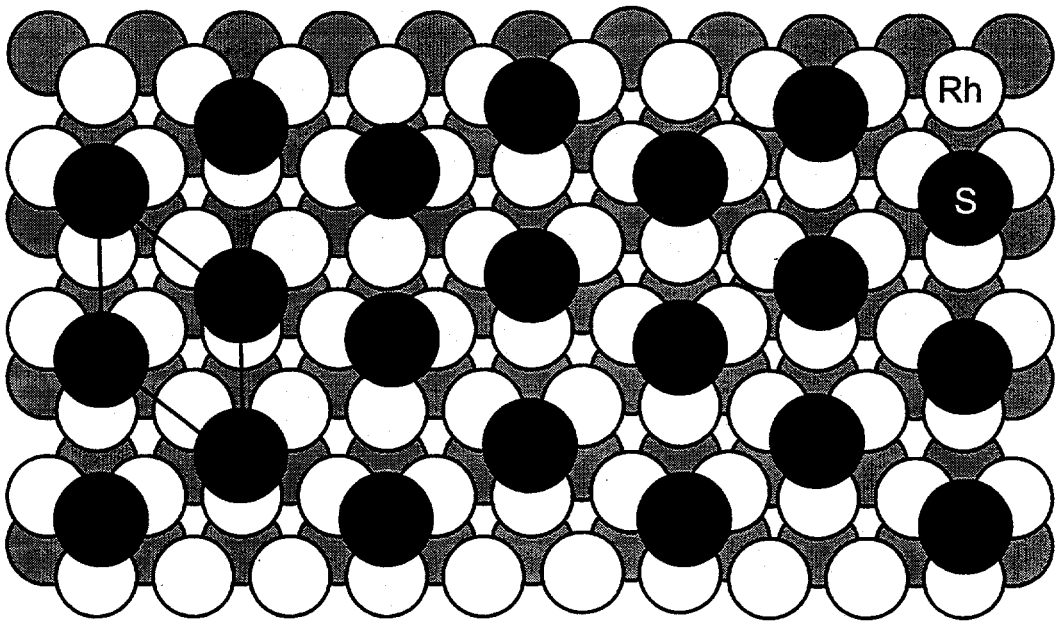

(b)

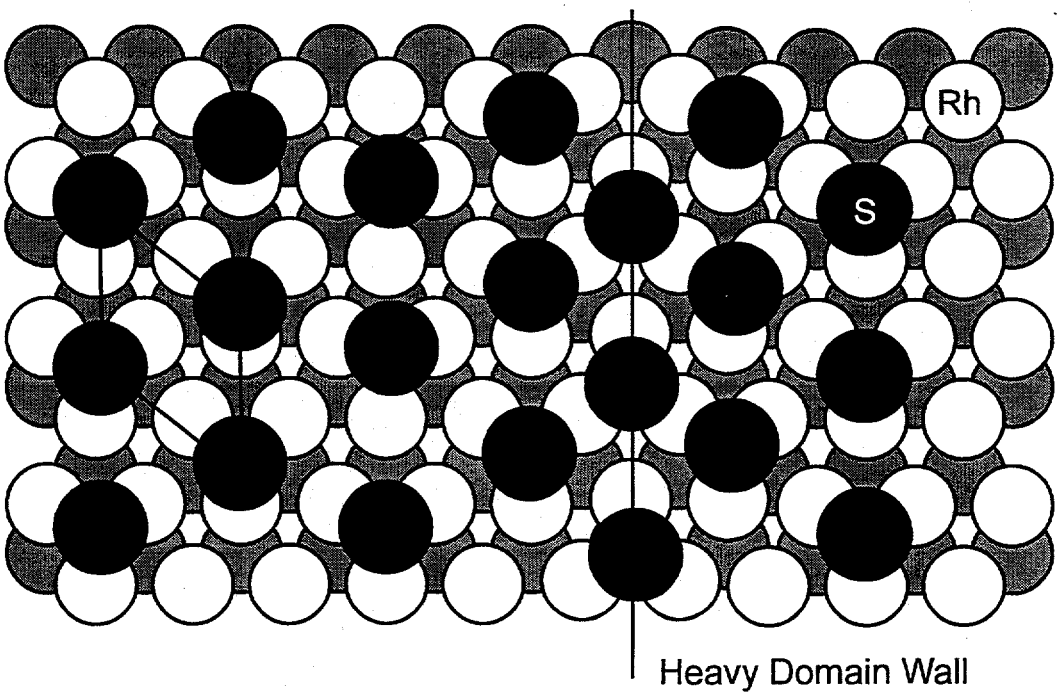

(c)

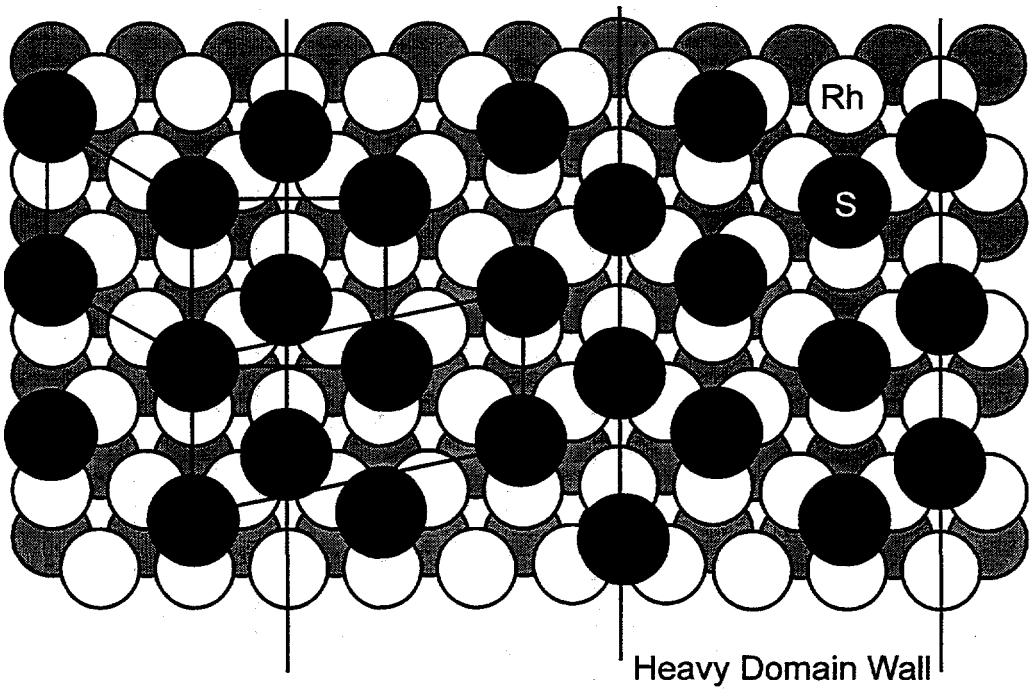

(d)

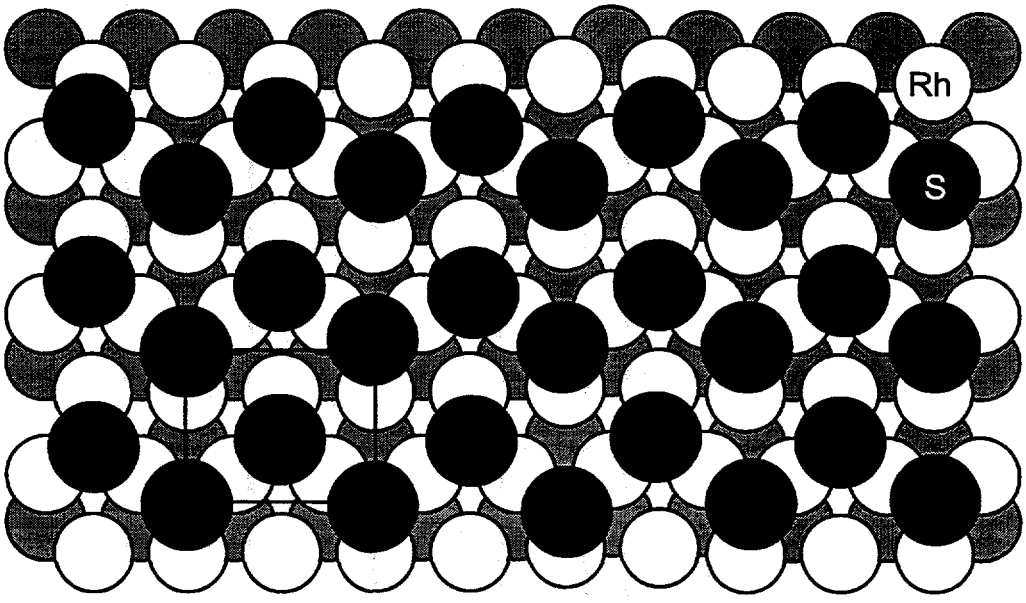

7.6 Conclusions

We have studied the sulfur overlayer on Rh(111) surface with AES, LEED and STM. Auger electron spectroscopy and LEED show that there are five ordered overlayers of sulfur. We have proposed a model for each ordered overlayer. As seen in Pt(111), sulfur adsorbs on the fcc-hollow site in the $(\sqrt{3}x\sqrt{3})R30°$ overlayer. As the coverage increases, sulfur starts to occupy the hcp-hollow site. In $c(\sqrt{3}x7)$rect structure, sulfur adsorbs in both the fcc and the hcp sites with 2:1 occupation. In the c(4x2) overlayer, there are equal occupation of adsorption between the fcc- and hcp-hollow sites. The possible transition from the $(\sqrt{3}x\sqrt{3})R30°$ to c(4x2) overlayer was proposed as the formation of heavy domain wall based on the observation of $c(7x\sqrt{3})$rect overlayer. The formation of surface clusters was observed in case of (4x4)-8S overlayer at ½ ML and the surface sulfide formation was proposed for the (7x7) overlayer.

Chapter 7 References

1. J.S. Foord and A.E. Reynolds, Surf. Sci., 1985. **152/153**: p. 426.
2. K.C. Wong and K.A.R. Mitchell, Surf. Sci. Letters, 1994. **304**: p. L481.
3. K.C. Wong, W. Liu, M. Saidy, and K.A.R. Mitchell, Surf. Sci., 1996. **345**: p. 101.
4. C. Wagner, J. Chem. Phys., 1953. **21**: p. 1819.
5. P.C. Wong, M.Y. Zhou, K.C. Hui, and K.A.R. Mitchell, Surf. Sci., 1985. **163**: p. 172.
6. J. Cérda, H. A. Yoon, M. A. Van Hove, M. Salmeron, submitted
7. T. Müller, D. Heuer, H. Pfnür, and U. Kohler, Surf. Sci., 1996. **347**: p. 80.
8. H.A. Yoon, N. Materer, M. Salmeron, M.A. Van Hove, and G.A. Somorjai, Surf. Sci., 1996. to be published.

Chapter 8

STM studies of carbon monoxide on Rh(111)

8.1 Introduction

The surface structures of carbon monoxide on Rh (111) surfaces have been extensively studied [1-4]. It was found that carbon monoxide forms the $(\sqrt{3}x\sqrt{3})R30°$ at 1/3 ML then forms (2x2) overlayer at ¾ ML. The HREELS experiments indicate that at low coverages, CO adsorbs only on the top site based on the frequency of the C-O stretching. As the coverage of CO increases, another vibrational peak shows up, which corresponds to the CO adsorption on the bridge site. LEED analysis was based on the HREELS data, and the structure with mixed adsorption sites of CO made. In this model, there are two CO on the top site ('near' top site) and one CO molecule in the bridge site. Overall, these three CO molecules form a hexagonal overlayer to minimize the repulsion as explained by extended Huckel calculation [5]. Recently, another model for the ¾ ML

CO overlayer was published based on X-ray scattering experiments. In these studies, CO was found to have three-fold hollow site adsorption. The low coverage CO structure at ¼ ML has been reported but no detailed structural information is available.

For STM experiments, carbon monoxide presents a great challenge. Carbon monoxide is found to be very mobile on the surface at room temperature, thus it is not easy to image. On Pt(111), and Pd(111), isolated CO molecules were imaged as sombrero-like features at cryogenic temperature [6]. In these cases, the CO molecule is frozen to the surface such that the STM can image the CO molecule. At room temperature, it is still not an easy task. The solution was suggested to decrease the CO diffusion at room temperature by forcing CO molecules to saturate the surface in such a way that no vacant site is present. It was shown that this method of overcrowding the surface with CO could be performed in an electrochemical cell. By applying voltage to the sample, one can force a high coverage of CO to stabilize on the Pt(111) electrode [7].

In our experiments, the overcrowding of CO molecules on the surface was achieved by constantly re-adsorbing CO molecules to the surface such that the number of vacant sites for CO diffusion is minimized. It was found from these experiments, one can 'slow' the diffusion by establishing the dynamic equilibrium between desorption and adsorption of CO molecules on the surface. Two different (2x2) overlayer structures were observed at different coverages as the background pressure of CO differs.

8.2 Experiments

The experiments were carried out in a UHV chamber with a base pressure of 2 x 10^{-10} torr. The sample was cleaned by repeated cycles of argon ion bombardment, followed by annealing in 5.0 x 10^{-8} torr of oxygen, or in vacuum, until no impurities could be detected by Auger electron spectroscopy.

In order to prevent the surface diffusion, CO was introduced into the chamber as the background gas, in the batch mode (closed system). Prior to exposure, the sample was flashed to 1000 K to desorb any contaminant from the surface. The CO background pressure was varied from 5 x 10^{-9} to 5 x 10^{-5} torr. LEED patterns were recorded at a fixed background of CO or while the pressure of CO was increased or decreased. The arrival rate of CO to the sample is 2 x 10^{16} molecules $cm^{-2}s^{-1}$ at 5 x 10^{-5} torr of CO and 2 x 10^{13} molecules $cm^{-2}s^{-1}$ at 5 x 10^{-8} torr of CO. LEED experiments show that there are no changes in the quality of LEED patterns at a fixed CO partial pressure for at least 30 minutes.

STM images were taken after the desired LEED pattern was observed. Figure 8.1 shows the LEED pattern of (2x2) CO overlayer formed at 5 x 10^{-5} torr of CO. STM images start to degrade after 45 minutes of keeping CO as the background gas.

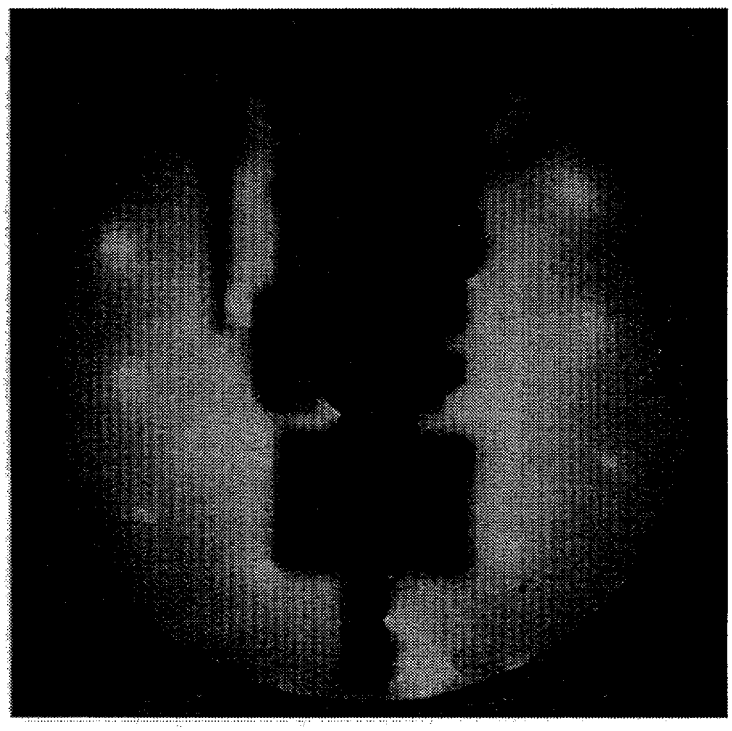

Figure 8.1 A LEED pattern corresponding to (2x2) overlayer at 98 eV. The (2x2) pattern was formed at 5 x 10^{-5} torr of CO partial pressure. The LEED pattern shows no change for at least 30 minutes, then the back ground intensities start to increase.

8.3 STM results

8.3.1 'Low' Pressure structure of CO

When the (2x2) LEED pattern is observed at 5 x 10^{-8} torr of CO, the sample was transferred to the microscope for imaging. The label 'Low' indicates the CO background pressure between 5 x 10^{-9} torr and 1 x 10^{-7} torr. The topographic images taken at 5 x 10^{-8} torr of CO are shown in Figure 8.2. Figure 8.2 (a) is a large scan area image (100 Å x

100 Å) taken at 1 nA and 100 mV. There are areas with less densely packed features can be seen. The protrusion in the image was assigned to the adsorbed CO molecule. The image shows a good ordering of CO molecules on the surface which is in agreement with sharp LEED pattern observed. A 65 Å x 90 Å area image was taken at 1 nA of current and 100 mV of bias as shown in figure 8.2 (b). The image also shows well ordered CO overlayers in (2x2) periodicity. This low coverage (2x2) structure can be imaged from 5 x 10^{-9} to 1 x 10^{-7} torr of background CO. Images start to be unstable after about 45 minutes of imaging.

As the CO partial pressure exceeds 1 x 10^{-7} torr, the image becomes very unstable. No features that can be related to the chemisorbed CO are visible, and the image fluctuates from one scan to the next. Sometimes during our STM experiment, the image becomes very unstable and produces images such as seen in Figure 8.3. Since the tip is made out of Pt/Rh some of the CO molecules will also adsorb on the tip resulting in a very unstable tip. Two images in Figure 8.3 were taken within 10 seconds, but show very dramatic changes in the image. Figures labeled 1 through 5 are zoomed images from Figures 8.3 (a) and 8.3 (b). Figures such as 2 and 4 show spherical features with very low corrugation (~ 0.1 Å), while Figure 3 shows triangular shaped features with very high corrugation of 0.5 Å. Figures 1 and 5 show asymmetric features suggesting the contamination of the tip.

The STM images clearly indicate that there is only one CO molecule per unit cell making the coverage ¼ ML. Figure 8.4 is the model for the Rh(111)-(2x2)-CO structure based on our STM experiments for coverage and the previous HREELS experiments for the adsorption site assignment.

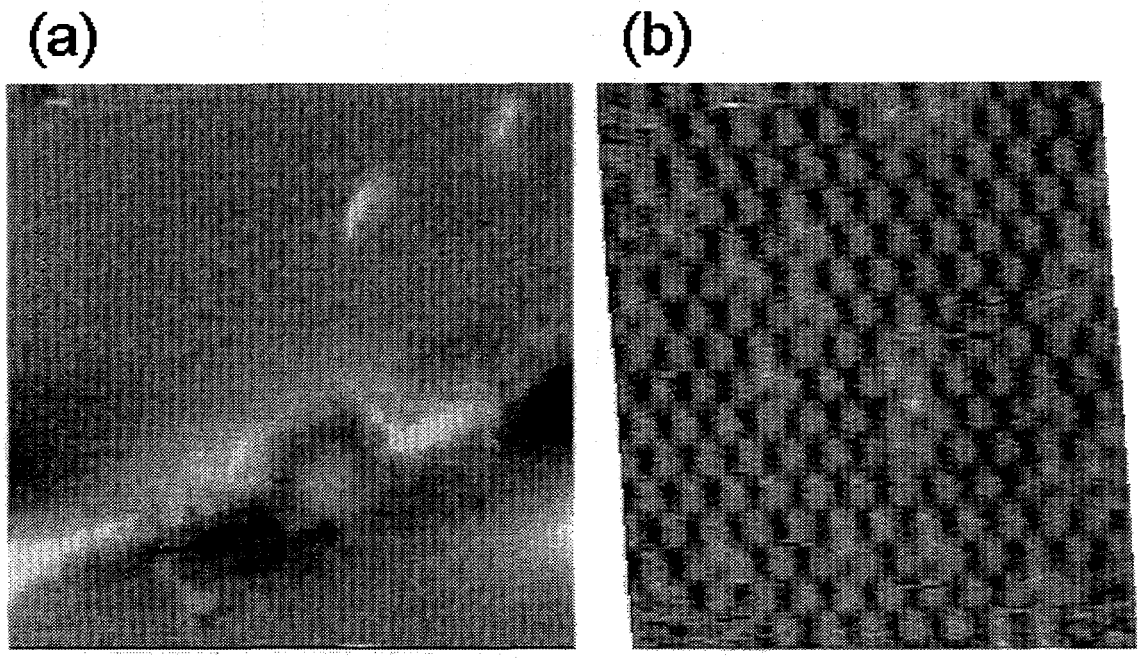

Figure 8.2 Topographic images of CO overlayer taken at 1 nA of current and 100 mV bias. (a) 100 Å x 100 Å scan area, (b)65 Å x 75 Å scan area. Both images show well ordered overlayer of CO in 2x2 periodicity.

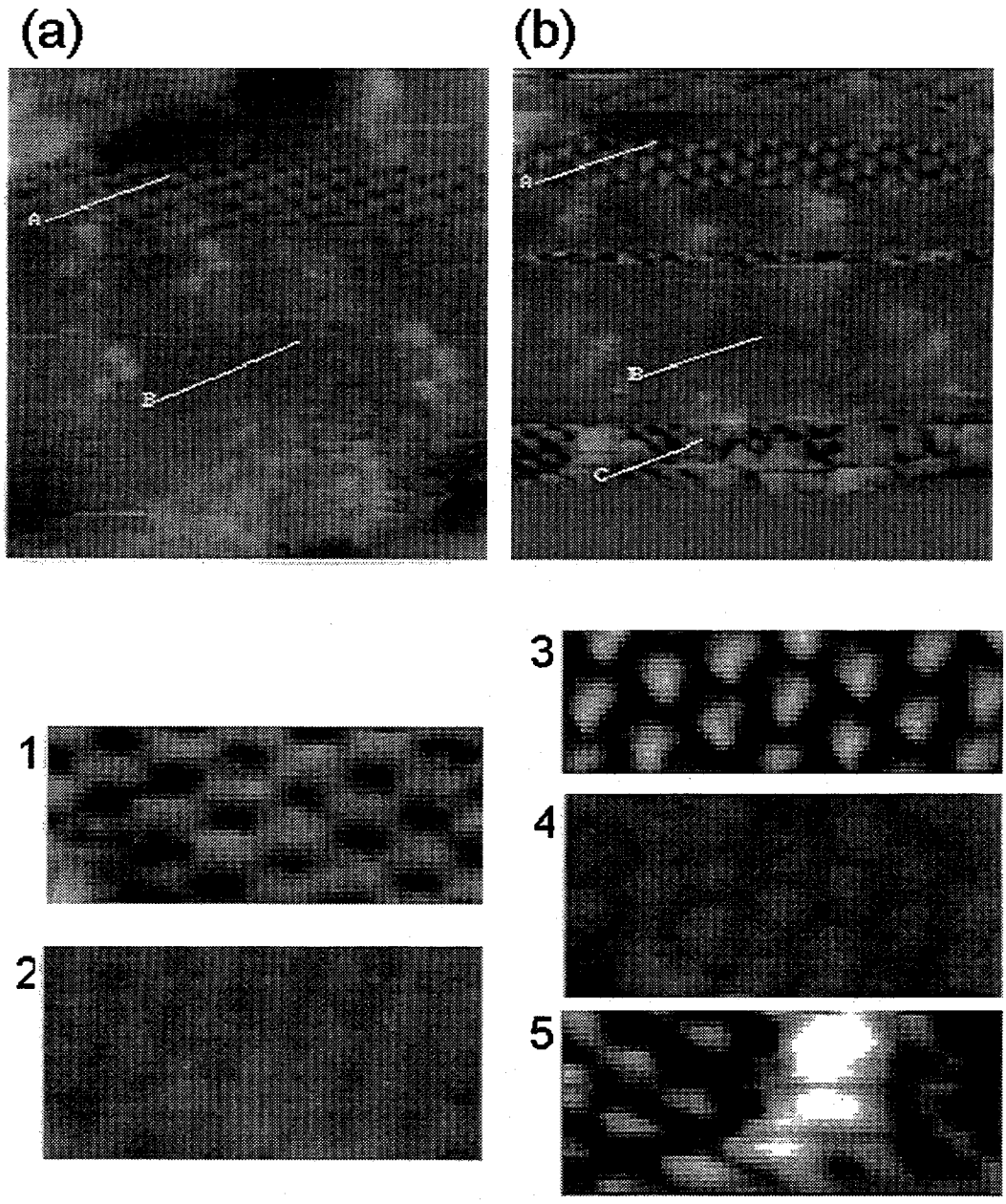

Figure 8.3 Two images taken consecutively with 10 seconds. The change within the image is observed and contributed as the change in the tip. The zoomed images of each tip change are also shown. The shape and the corrugation changes drastically. Figures 2 and 4 show spherical features with very low corrugation of 0.1 Å, while Figure 4 shows triangular features with 0.5 Å corrugation. Figures 1 and 5 show asymmetric features.

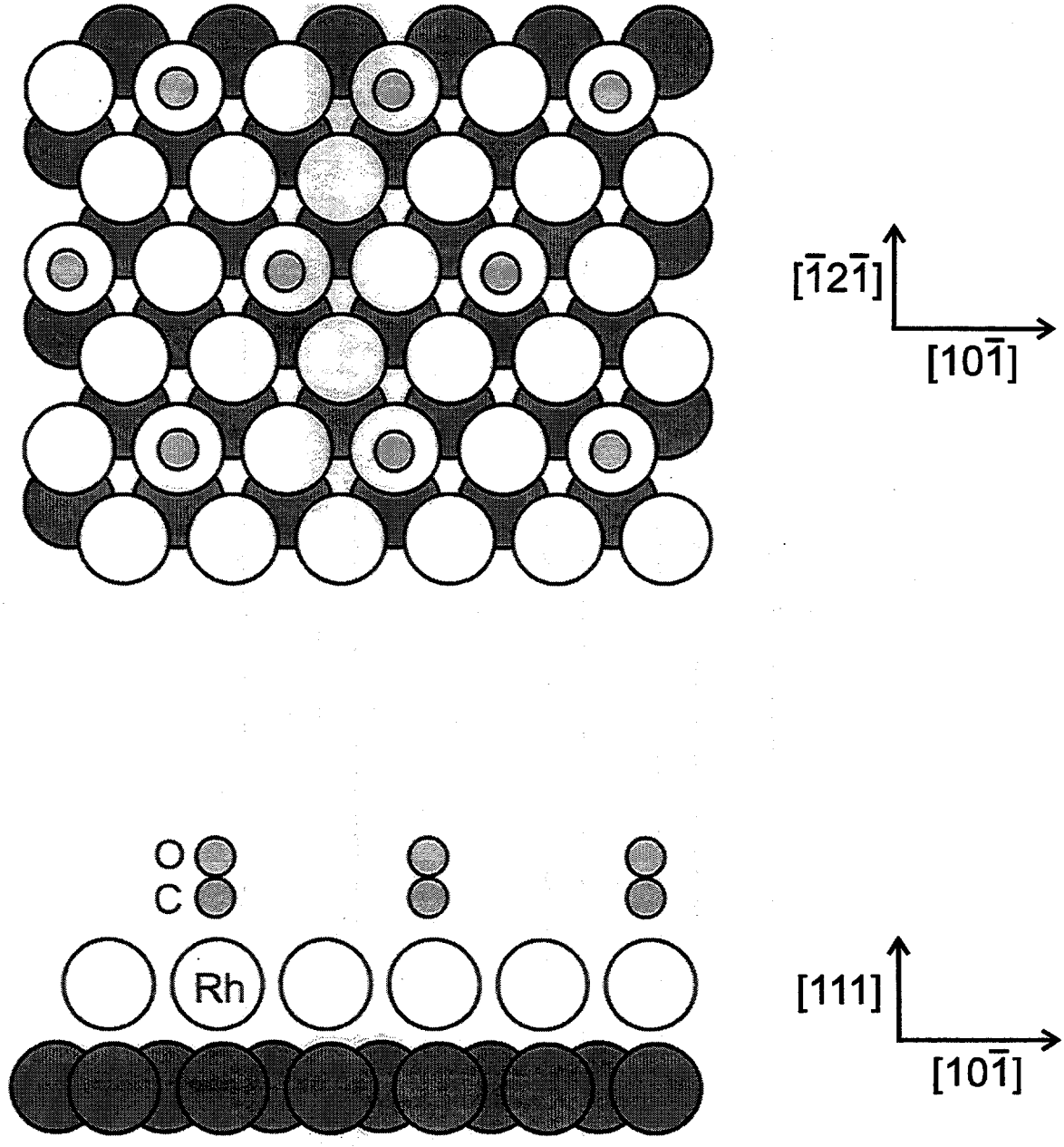

Figure 8.4 Proposed model structure of Rh(111)-(2x2)-CO based on the STM results and the previous HREELS results. There is one CO molecule per unit cell and each CO molecule adsorbs on the top-site.

8.3.2 'High' Pressure structure of CO

As the partial pressure of CO increased to 5 x 10^{-5} torr, a new (2x2) LEED pattern is observed. From the previous LEED and HREELS experiments, this (2x2) structure corresponds to a ¾ ML overlayer. STM images were obtained with this structure. The images of this 'high' pressure CO overlayer are not stable, but at certain moments, a good image can be obtained. Topographic images of this (2x2) overlayer are shown in Figure 8.5. These two images were taken consecutively at 1 nA and 100 mV. Even though, one image takes about 20 seconds to acquire, the two images are not alike. This means there is rapid change in the structure, perhaps due to the tip interaction or the high pressure of CO disturbing the structure. Three features are imaged in the unit cell and they appear to form clusters on the surface. The spacing between each feature in the cluster is about the lattice parameter of the substrate. The size of these three-leaf clover like features suggests that these are not a tip artifact. From these images we proposed the carbonyl cluster model of the surface as shown in Figure 8.6.

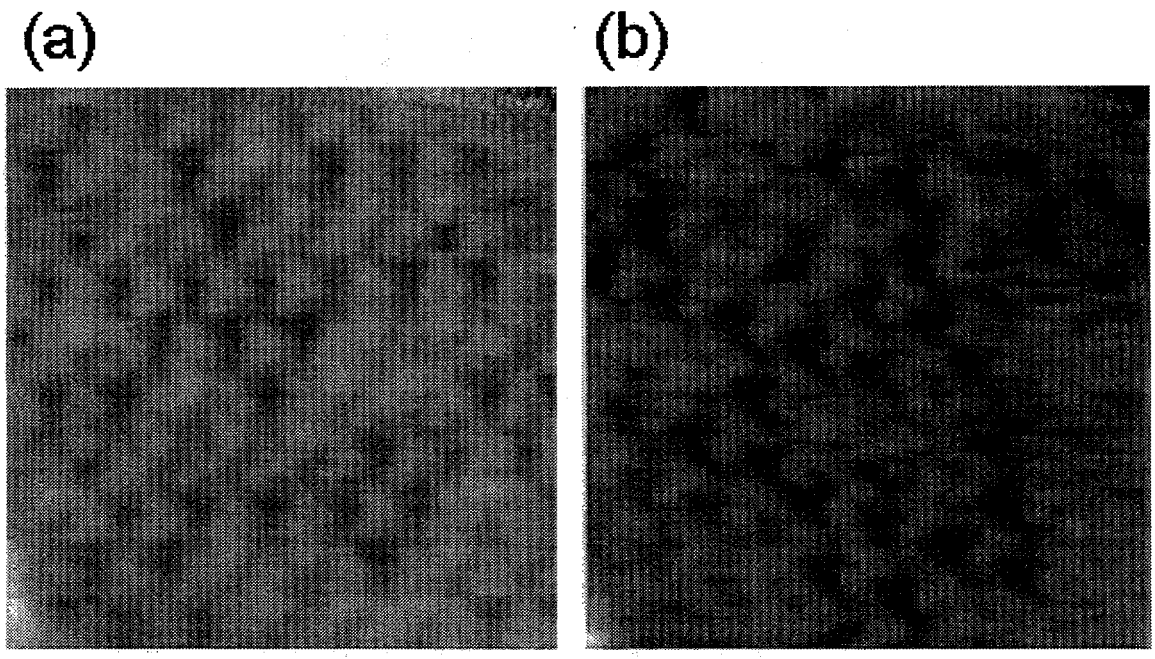

Figure 8.5 Topographic images of 'high' pressure CO overlayer. Three-leaf clover like features are visible. The spacing between these features is twice the lattice parameter of the substrate. The formation of surface carbonyl cluster is suggested.

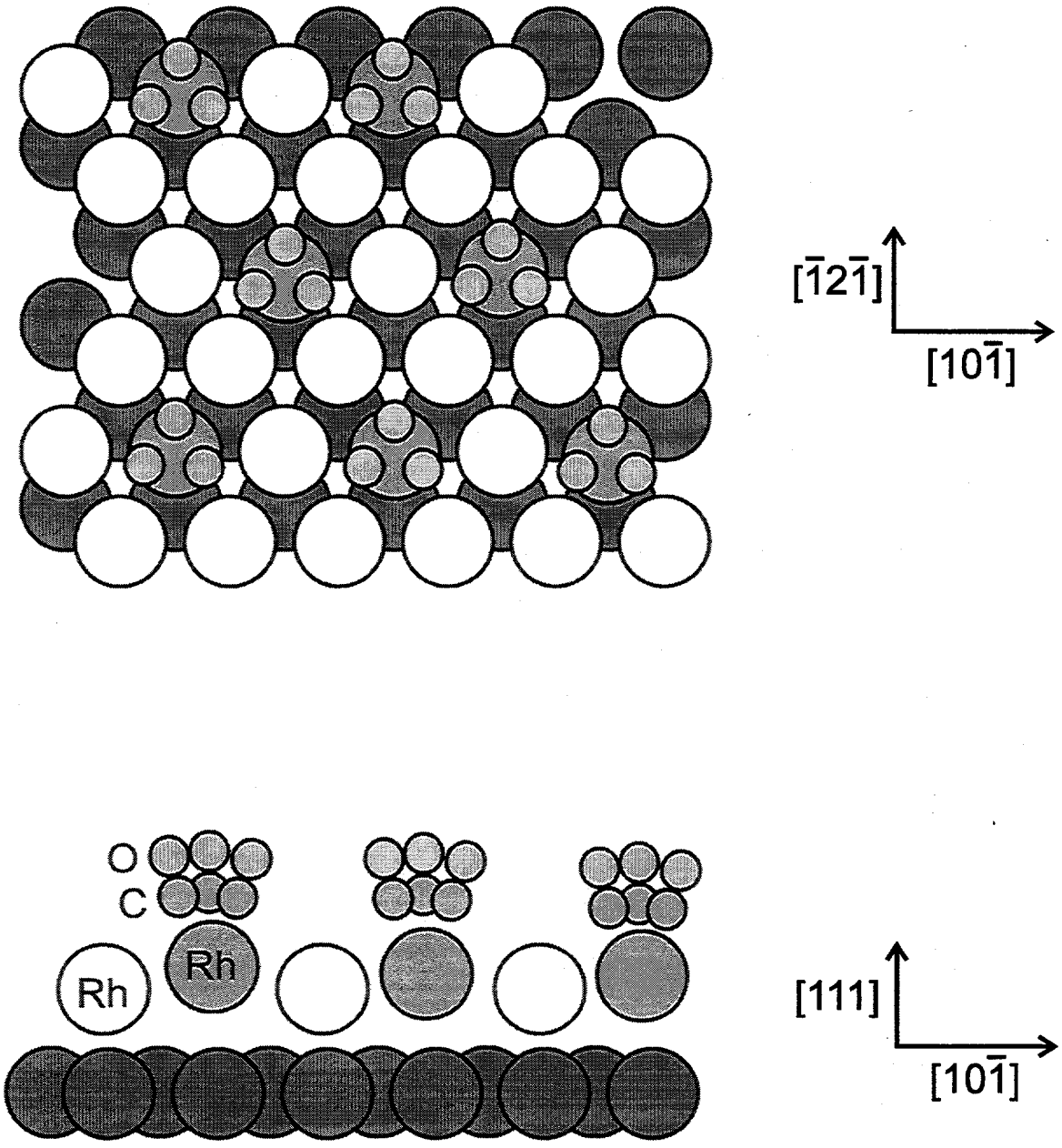

Figure 8.6 Proposed model structure of Rh(111)-(2x2)-3CO based on the STM results. Three CO molecules are imaged per unit cell and CO molecules are imaged as three-leaf clover like features. The formation of surface carbonyl clusters is proposed in this model.

8.4 Discussion

The structure of carbon monoxide has been extensively studied due to its importance in CO-oxidation and syn-gas reactions. On the Rh(111) surface, only the $(\sqrt{3}x\sqrt{3})R30°$ structure and the high coverage of (2x2)-3CO had been observed previously [2-4]. The structures determined by LEED calculation were in agreement with HREELS experiments [8]. CO molecules adsorbing at low coverages were observed to have a single adsorption site in HREELS study. As the coverage of CO increases, the second peak due to stretching of the CO molecule adsorbed on a different site was observed. It was concluded in this study that the adsorption site at low coverage occurs at the atop site, and at mixed top and bridge sites for the high coverage. LEED analysis was carried out for both low coverage and high coverage structures, and confirmed what was known by HREELS study. However, there is little discussion about the ¼ ML CO structure. Thiel et al observed evolution of [½,½] LEED spot with SPLEED, and suggested that there is an ordered overlayer of sulfur at ¼ ML. Recently, another model for the high coverage structure was proposed, and the structure of these overlayers became controversial.

We carried out the STM studies to elucidate the structures of CO on Rh(111) as the background pressure of CO was maintained to establish the dynamic equilibrium between desorption and re-adsorption of CO molecules. This method blocks diffusion of CO molecules on the surface such that STM can be used to image the surface. At 'low ' pressure of CO (below 1 x 10^{-7} torr), a (2x2) overlayer of CO was imaged. Only one feature that can be assigned to CO molecules per unit cell, making the total coverage of

CO to be ¼ ML. We propose the model structure for Rh(111)-(2x2)-CO overlayer to be one CO molecule per unit cell and top adsorption site based on our STM experiments and the previous HREELS results.

Since the tip is made out of essentially the same material as the sample, we expect that the tip would be also covered with CO. A contaminated tip has been shown to produce big changes in the image [9, 10]. Images vary from spherical features with very low corrugation to triangular shaped features with high corrugation. Also, the asymmetric features can be seen. We believe that the spherical features with low corrugation is an image with the tip relatively free of contamination as shown in both STM experiments and theoretical work. In some cases the atomic contaminants at the apex of the tip can enhance the corrugation of the image as shown by experiments [9] and confirmed by theoretical work [10-13]. This would explain the rest of the images. The triangular and asymmetric shaped features must be due to a contaminated tips.

When the CO background pressure was increased to 5 x 10^{-5} torr, the 'high' pressure images can be seen. Our STM experiments show that there are three maxima per unit cell confirming the previous HREELS and LEED results. However, the images suggest the formation of surface clusters which is in disagreement with LEED analysis. It could be argued that the images we see are due to the contamination of the tip as shown earlier. However, the size of the clusters is much larger than that of the triangular feature due to tip change in the Figure 8.3.4. Also the spacing between the maxima inside the cluster is about the lattice parameter of the substrate. The model based on our STM experiments is proposed. In this model, some relaxation in the first substrate layer is proposed.

8.5 Conclusion

We have successfully imaged the different CO ordered overlayers on a Rh(111) surface. Our STM images indicates that at low pressure of CO, it forms the ¼ ML (2x2) structure and at high pressure of CO the formation (2x2) overlayer with ¾ ML coverage is observed. Based on our experiments, the models for these two different ordered overlayers were proposed. In the low pressure structure, the CO adsorption on the atop site is proposed and the surface cluster formation is suggested in the high pressure structure. The high pressure CO structure is another example of lowering of the overall energy due to the overcrowding by the formation of a surface cluster.

Chapter 8 References

1. J.E. Crowell and G.A. Somorjai, Appl. Surf. Sci, 1984. **19**: p. 73.
2. M.A. Van Hove, R.J. Koestner, J.C. Frost, and G.A. Somorjai, Surf. Sci., 1983. **129**: p. 482.
3. M.A. Van Hove, R.J. Koestner, and G.A. Somorjai, Phys. Rev. Lett., 1983. **50**: p. 903.
4. R.J. Koestner, M.A. Van Hove, and G.A. Somorjai, Surf. Sci., 1981. **107**: p. 439.
5. E. Ruckenstein and T. Halachev, Surf. Sci., 1982. **122**: p. 422.
6. D.M. Eigler, Nature, 1993. **363**: p. 524.
7. I. Villegas and M.J. Weaver, J. Chem. Phys., 1994. **101**: p. 1648.
8. L.H. Dubois and G.A. Somorjai, Surf. Sci., 1980. **91**: p. 514.
9. B.J. McIntyre, P. Sautet, J.C. Dunphy, M. Salmeron, and G.A. Somorjai, J. Vac. Sci. Technol. B, 1994. **12(3)**: p. 1751.
10. P. Sautet, J.C. Dunphy, D.F. Ogletree, C. Joachim, and M. Salmeron, Surf. Sci., 1994. **315**: p. 127.
11. P. Sautet and C. Joachim, Chem. Phys. Lett., 1991. **185**: p. 23.
12. P. Sautet, J. Dunphy, D.F. Ogletree, and M. Salmeron, Surf. Sci., 1993. **295**: p. 347.
13. P. Sautet and M.-L. Bocquet, Surf. Sci. Lett., 1994. **304**: p. L445.

Chapter 9

STM study of benzene and its coadsorption with carbon monoxide on Rh(111)

9.1 Introduction

The formation of benzene overlayers, and of coadsorbed benzene and CO on Rh(111) has been studied using temperature programmed desorption (TPD) [1, 2], high resolution electron energy loss spectroscopy (HREELS) [1-3], low energy electron diffraction (LEED) [4-8], inverse photoemission spectroscopy [9], angle resolved ultraviolet photoelectron spectroscopy (ARUPS) [10, 11] and STM [12-14]. It was shown by HREELS [2, 3] that at 300 K, benzene adsorbs forming a π-bonded chemisorbed species with its ring parallel to the surface. LEED experiments revealed the evolution of different ordered structures as the amount of carbon monoxide coadsorbed with benzene increased. Dynamic LEED calculations for the c(2$\sqrt{3}$x4)rect and (3x3) surface structures show that the carbon ring is parallel to the surface and centered at hcp hollow sites while CO adsorbs

upright and also centered at hcp hollow sites [4, 5, 7, 8]. These results revealed also that there is one benzene and one CO molecule per unit cell in the c(2√3x4)rect structure, and one benzene and two CO molecules per unit cell in the (3x3) structure as sown in Figure 9.1.

Work function measurements on Rh(111) [15, 16] indicate that benzene is an electron donor, since adsorption reduces the work function of the substrate. Carbon monoxide, however, is an electron acceptor, as it increases the work function of the metal. The work function still decreases when the ratio of CO to benzene increases in coadsorbed systems, indicating that carbon monoxide remains an electron acceptor when coadsorbed with benzene.

The ordered c(2√3x4)rect and (3x3) coadsorption structures were imaged with STM at room temperature [12-14]. In these studies, benzene appeared as a ring-like feature in the images and domain boundaries were observed.

We investigated the benzene and benzene/CO coadsorption systems using STM to study the dynamics of ordering as a function of carbon monoxide coverage. We observed the time evolution of the surface structures both when CO is introduced onto the benzene covered surface and when benzene is introduced onto the CO covered surface. These dynamical studies of coadsorption should provide information for a molecular scale understanding of the surface reactions in catalysis, where more than one competing species are adsorbed. Since STM is a local probe technique, it is suitable to study the ordered as well as disordered surface structures.

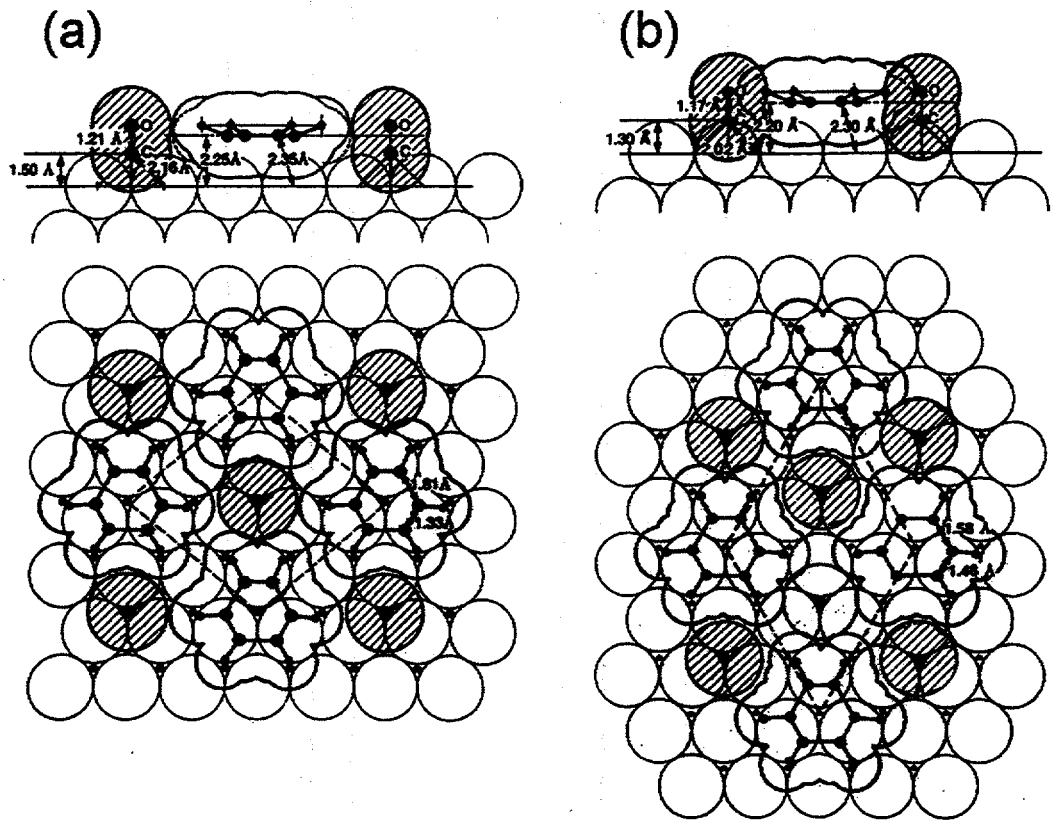

Figure 9.1 The structure of Rh(111) - c(2√3x4)rect - C_6H_6 + CO (a) and Rh(111) - (3x3) - C_6H_6 + 2CO (b) in the top view and side view including the van der Waals contours. CO molecules are shown with shade. The unit cell is outlined. (Ref. [5, 7, 8])

9.2 Experiment

The experiments were carried out in a UHV chamber with a base pressure of 7×10^{-11} torr. The sample was cleaned by repeated cycles of argon ion bombardment, followed by annealing in 5.0×10^{-8} torr of oxygen, or in vacuum, until no impurities could be detected by Auger electron spectroscopy.

Benzene was purified by several freeze-thaw cycles to remove water and other contaminants. Benzene and carbon monoxide were introduced into the UHV chamber through separate variable leak valves, connected to a tube doser that was positioned to within 1 cm from the sample surface. Separate leak valves were used to eliminate the cross contamination of the gases. Prior to exposure, the sample was flashed to 1000 K to desorb carbon monoxide. Exposures were in the range of 0.5 to 2 L at room temperature. AES shows that the height of carbon 272 eV peak does not increase any more after 1 L of benzene exposure. 2 L exposure was used to ensure the saturation coverage of benzene on the surface. The base pressure of the system raised to 2×10^{-10} torr after dosing, but returned to the initial base pressure of 7×10^{-11} torr after a few minutes. No further annealing was carried out after exposure.

9.3 Results

9.3.1 Benzene adsorption on clean Rh(111)

The adsorption of benzene on Rh(111) as a function of exposure was first examined by AES. We found that after 1 L of exposure (at 1 x 10^{-7} torr of pressure), the intensity of the 272 eV carbon peak did not show any further increase, indicating that maximum saturation of benzene had been reached. In subsequent experiments, 2 L of exposure was routinely used without further checking with AES.

A topographic image of the saturated overlayer at 300 K is shown in Figure 9.2. This 40 Å x 40 Å image was acquired at a tunneling current (i_t) of 1 nA and a sample bias voltage (V_s) of 100 mV. Benzene appears in this image in the form of ring-like structures with size of ~ 5 Å. Small domains of ordered molecules can be seen. However, no apparent long range order is visible for most of the molecules.

When the surface was exposed to 0.5 L of benzene, STM images like that in Figure 9.3(a) were obtained (110 Å x 110 Å). This image shows benzene at the top side of the step edges indicating preferential adsorption at these sites. Based on our AES calibration, the 0.5 L exposure corresponds to about 0.5 ML coverage. However, the number of benzene molecules visible in the images, corresponds to a coverage of about 0.2 ML. This indicates that many of the benzene molecules present on the surface are not imaged. This is most likely due to diffusion which is faster than the scanning rate (in these experiments the scanning rate was 40 Å/ms, corresponding to about 1 second per image).

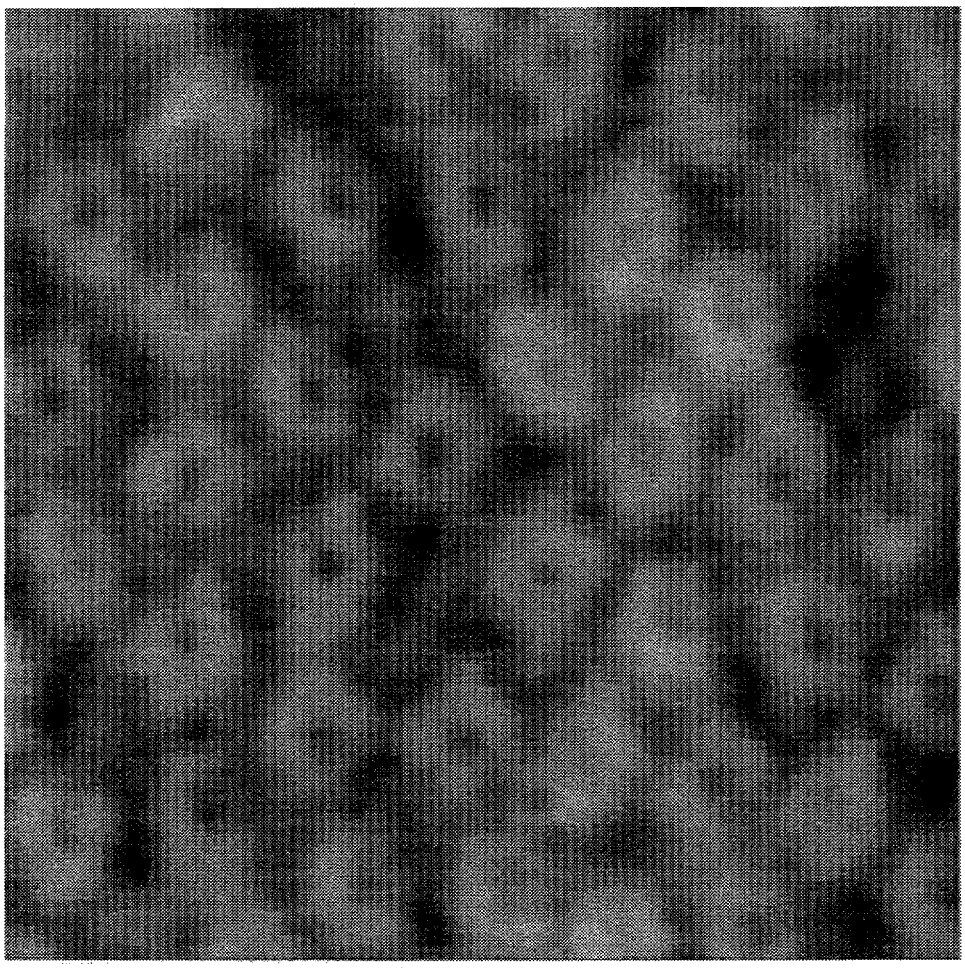

Figure 9.2 Topographic image of benzene at saturation coverage taken at sample bias of 100 mV and tunneling current of 1 nA (40 Å x 40 Å). No apparent long range order is observed despite of small domains of ordered benzene molecules.

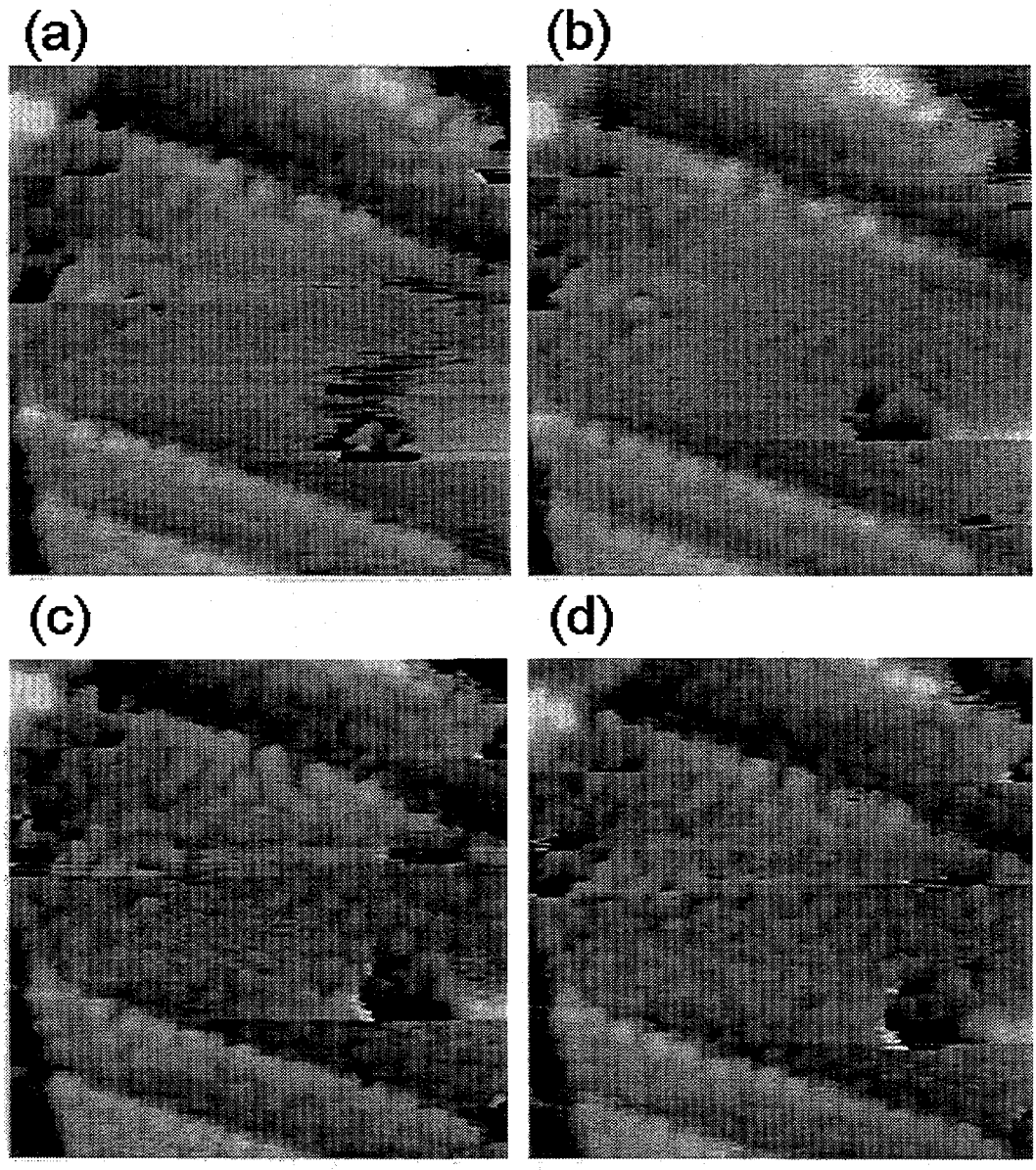

Figure 9.3 (a) Topographic image of benzene at 0.5 ML coverage. Benzene appears to decorate the top side of the step edges preferentially; (b) 2 minutes after CO is introduced at 5 x 10^{-8} torr, additional benzene molecules can be imaged, particularly around the defect sites (c) Image taken 5 minutes after CO dosing, revealing more benzene molecules as CO coverage increases. (d) After 7 minutes, the surface is covered with about 0.5 ML of benzene. Some ordering is observed in the middle of the image and it appears to be c(2√3x4)rect structure.

The presence of these invisible, mobile benzene molecules, could be verified by introducing a small amount of CO. Figure 9.3(b) was taken 2 minutes after CO introduction at 5 x 10^{-8} torr. Additional features associated with immobilized benzene molecules can be imaged around the defect sites. Although the ring-like internal structure of benzene was not resolved in these images, their shape and size (~5 Å) indicated that they were indeed due to benzene. This result confirms our assumption that benzene molecules on the terraces were not imaged because of their rapid diffusion in the absence of CO. The coadsorbed CO decreases the mobility of benzene such that it becomes visible to the STM. The additional benzene molecules are particularly visible around defect sites and at the bottom of the step edges. Figure 9.3(c), taken 4 minutes after CO dosing, shows the increased extent of CO-induced immobilization of benzene molecules. The number of benzene molecules imaged after this high CO exposure corresponds to about 0.5 ML coverage, as expected. Small ordered domains with c(2√3x4)rect structure are observed after 7 minutes of CO exposure, based on the detected distances and the angles between adsorbed benzene molecules as shown in Figure 9.3 (d). The CO molecules were not visible in these STM images.

9.3.2 Benzene adsorption on CO precovered Rh(111)

Even small amounts of preadsorbed carbon monoxide (< 0.1 L) had a dramatic effect on the ordering of benzene. Both the c(2√3x4)rect and (3x3) structures could be observed, depending on the amount of preadsorbed CO, which produced the LEED patterns shown in Figure 9.4(a) and 9.4(b). The STM images were taken after obtaining sharp LEED patterns.

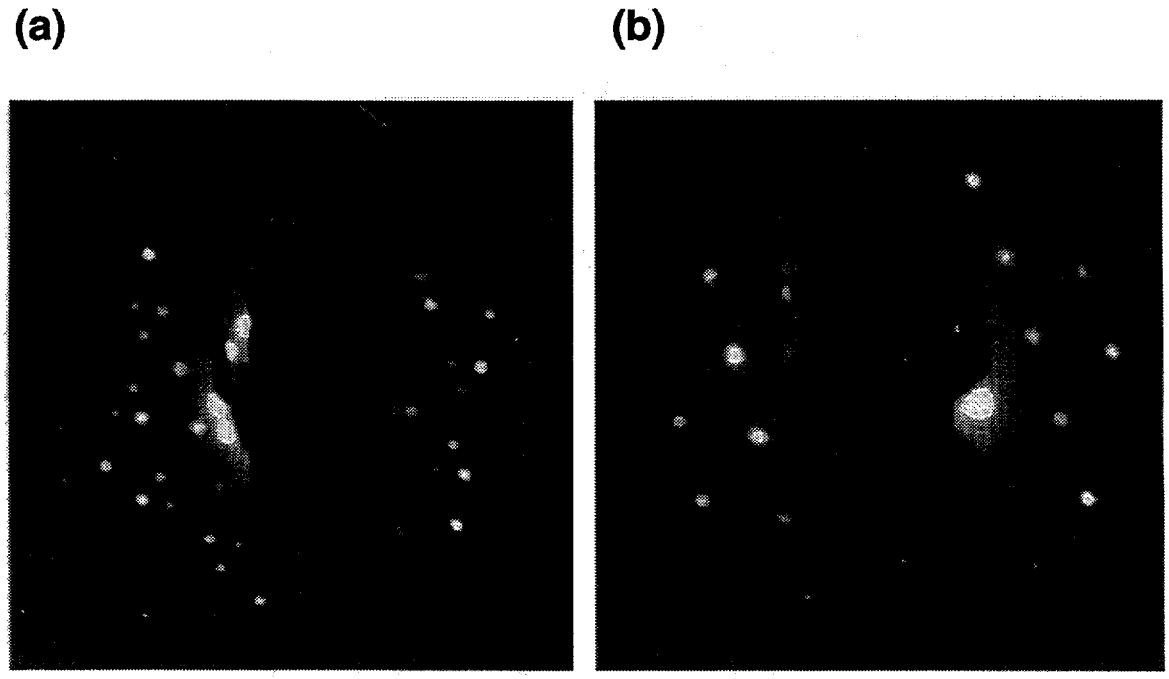

Figure 9.4 LEED patterns due to the ordered structures formed by coadsorbed benzene and carbon monoxide. The c(2√3x4)rect (a) and (3x3) (b) structures can both be observed as a function of increasing CO coadsorption.

The STM images also show well ordered layers, as shown in the 115 Å x 100 Å topographic image of Figure 9.5(a), corresponding to a c(2√3x4)rect benzene/CO structure. Since the substrate is three fold symmetric, three rotational domains can exist. In case of a c(2√3x4)rect benzene/CO overlayer, the close-packed direction of benzene does not coincide with the close-packed direction of the substrate. Thus angles between domains will be some angle other than 120°. The rotational domain boundary and translational boundary were observed in Figure 9.5(a).

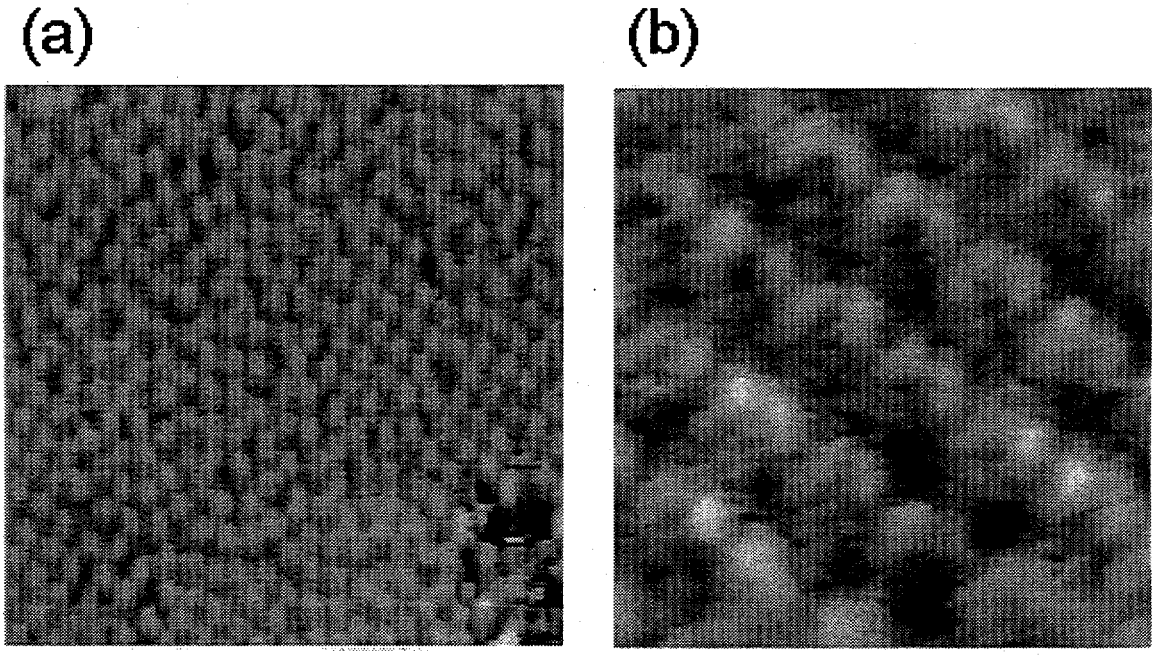

Figure 9.5 (a) 115 Å x 100 Å area image of c(2√3x4)rect benzene/CO structure. Only features associated with benzene can be imaged. Rotational and translational domain boundaries such as those marked by R and T are often observed.; (b) High resolution image of c(2√3x4)rect benzene/CO structure. Ring-like features of benzene molecules are visible under tunneling conditions of sample bias between 100 mV and -100 mV and tunneling current of 1 nA.

The existence of the rotational domain boundary, and the distances (7.1 Å) and angles (81.2 and 98.2 degrees) between benzene molecules confirm that the overlayer is indeed the c(2√3x4)rect benzene/CO overlayer. Under tunneling conditions of 1 nA and sample bias of 100 mV, only features associated with benzene could be imaged. The corrugation along the close packed direction of benzene is about 0.5 Å. Figure 9.5(b) is the smaller area (25 Å x 25 Å) topographic image which shows the ring-like features of benzene molecules.

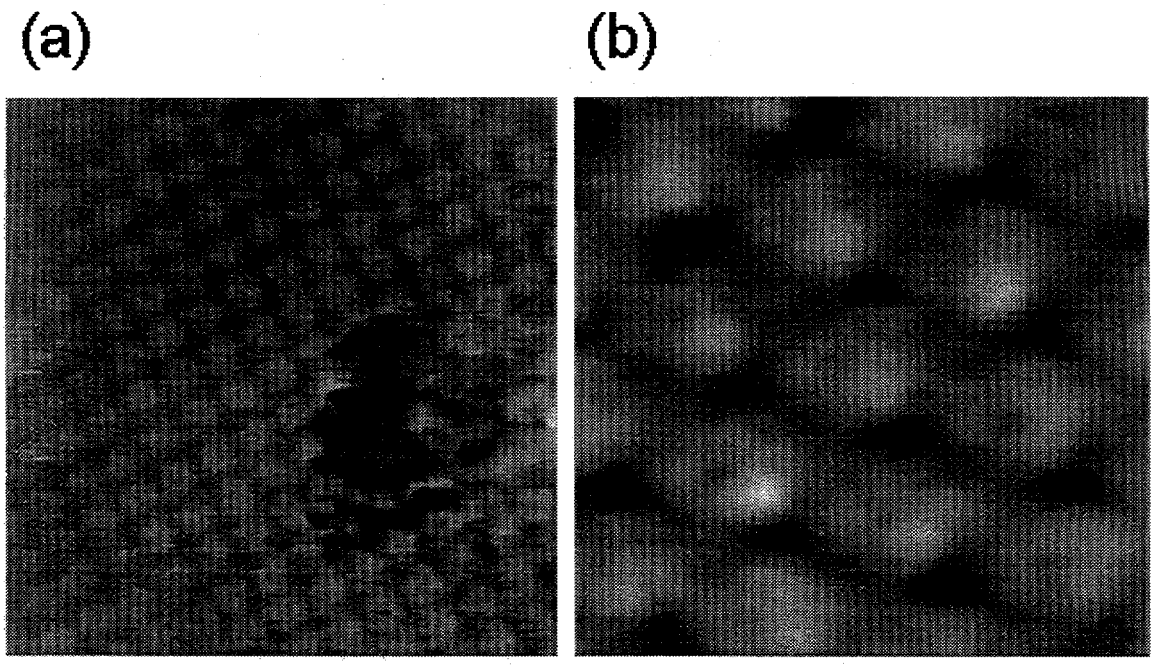

Figure 9.6 (a) Topographic image of an ordered (3x3) structure taken at a sample bias of +100 mV and tunneling current of 1 nA. It shows the ordered benzene molecules. No feature that can be associated with CO is imaged under this tunneling condition. (b) High resolution image of (3x3) benzene/2CO structure. Ring-like features of benzene molecules are visible under tunneling conditions of sample bias between 100 mV and -100 mV and tunneling current of 1 nA.

Figure 9.6(b) is a topographic image of an ordered (3x3)-benzene/2CO overlayer (85 Å x 85 Å). The corrugation of benzene molecules was 0.7 Å along the close-packed direction of benzene in this structure. As in the previous structure, no feature that could be associated with CO was imaged under similar tunneling conditions. We also studied the dependence of the image contrast on the tunneling gap parameters. To this effect, the sample bias voltage was varied from -0.5 to 1.0 V while maintaining the tunneling current

at 1 nA. For the well ordered (3x3) benzene/2CO structure, images with ring-like benzene features could be obtained with bias voltages within ± 100 mV, as shown in Figure 9.6(b). The apparent size of benzene ring was about 5 Å, and its corrugation was 0.5 Å, which was the same as the corrugation of benzene molecular features in Figure 9.6(a). However no CO features were observed in these conditions either.

We then studied the effect of higher CO coverage. To stabilize a 0.25 ML of carbon monoxide at room temperature, a background pressure of 5 x 10^{-8} torr of CO was necessary. The STM images of 80 Å x 80 Å show the appearance of rows of CO molecules as shown in Figure 9.7(a). After exposing this CO covered surface to 5.0 x 10^{-8} torr of benzene, a series of images were taken as a function of time. The images in Figures 9.7(b), (c)and (d) were obtained after 2, 4 and 7 minutes of benzene exposure, respectively. Again, even though the ring-like shape of the benzene features were not resolved, the new features could be assigned to benzene molecules based on their shape and size, which is consistent also with the observation that their number increases with benzene exposure. Benzene adsorption occurs in the middle of the terraces as seen in Figure 9.7(b). In these experiments we let the background CO pressure drop from its initial 5.0 x 10^{-8} torr value after the introduction of benzene. This caused the benzene coverage to increase while the features associated with carbon monoxide disappeared. This probably indicates that the CO in excess of that needed to form the stable ordered CO/benzene mixed structures is desorbing from the surface. Figure 9.7(b) shows the brighter, larger benzene features coexisting with smaller dimmer ones.

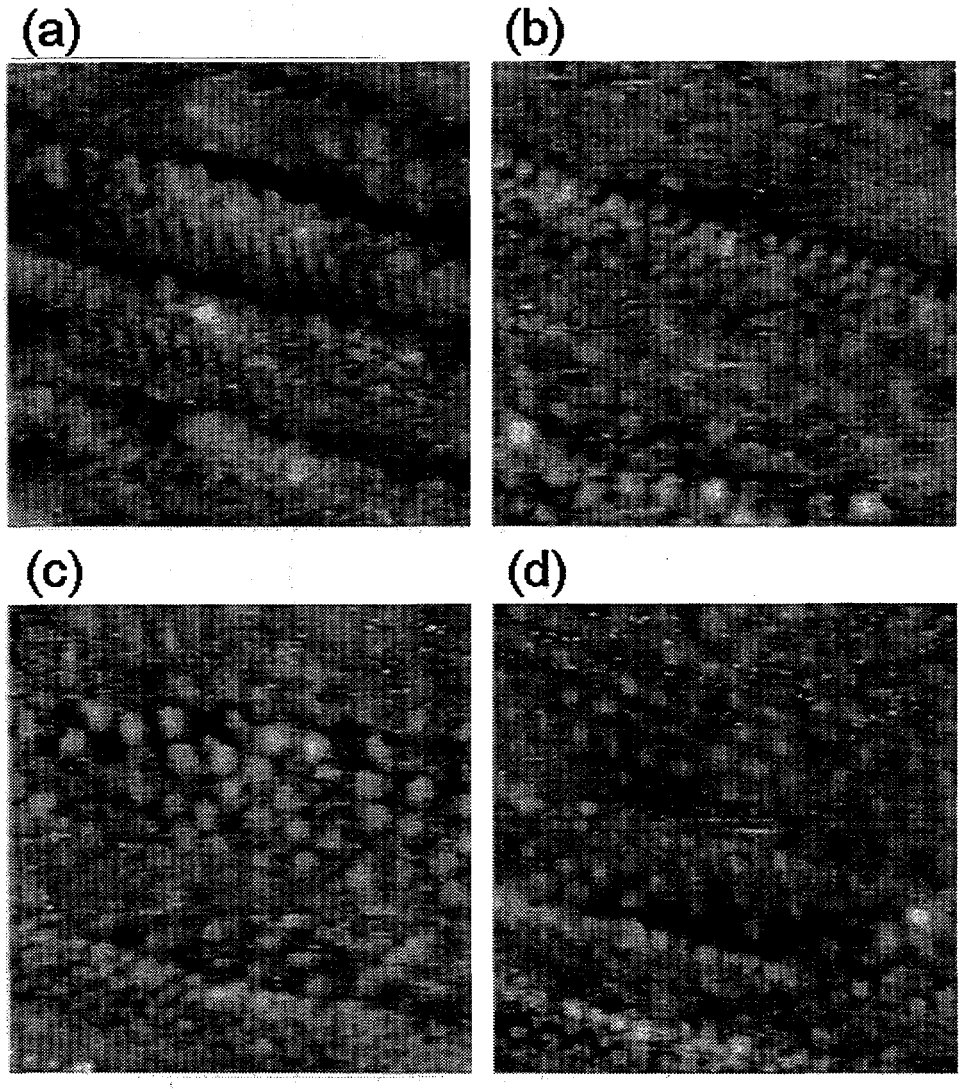

Figure 9.7 (a) Surface covered with carbon monoxide at 0.25 ML coverage (80 Å x 80 Å). Row-like features due to adsorbed CO are visible; (b) Image taken 2 minutes after the surface was exposed to 5 x 10^{-8} torr of benzene. The bright features associated with adsorbed benzene molecules are visible along with smaller features due to CO (c) As benzene coverage increases (4 minute) the row-like features associated with CO disappear indicating CO displacement from the surface, however a few remaining features associated with carbon monoxide are still visible at the bottom of the image.; (d) Image taken 7 minutes after benzene was introduced into the chamber. Most of the surface is now covered by the ordered (3x3)-C_6H_6+2CO structure.

These features are smaller than the features associated with adsorbed benzene and their spacing is close to 5.5 Å, which is comparable to that of the carbon monoxide features in Figure 9.7(a). Since the surface is still covered with carbon monoxide, these features are assigned to carbon monoxide. The increased ordering of adsorbed benzene and carbon monoxide forming a (3x3) surface structure on the terrace is seen in Figure 9.7(d).

9.4 Discussion

In our STM studies, when benzene was adsorbed at saturation coverage without carbon monoxide, no long range order was observed although some small domains of ordered benzene were visible. This is in agreement with the observations of Mate et. al [15, 16], using LEED and HREELS. These authors observed a high background intensity in the diffraction pattern of $(2\sqrt{3}x3)$rect overlayer when only benzene was adsorbed. Also, they observed two different frequencies for the out-of-plane C-H bending mode of the benzene molecules, which were attributed to benzene in two different adsorption sites, bridge in the ordered domains and three-fold hollow in the disordered regions.

At a coverage of 0.5 ML of benzene, only a small fraction of the molecules were imaged, those adsorbed on the top side of the step edges. Since benzene molecules are also present on the terraces, as known from the exposure and confirmed by the subsequent coadsorption of carbon monoxide, we must conclude that, when diluted, benzene on the terraces diffuses faster than the scanning time in STM and thus cannot be imaged. The lack of mobility of the benzene adsorbed at the step edges indicates a stronger binding at these

sites. This observation is in agreement with the electron donor character of benzene, which would favor adsorption on sites of lower electron density such as at the step edges. This type of preferential adsorption of benzene was also observed on Cu(111) [17]. In these experiments, additional ordered parallel lines of molecules were formed. The observations were explained by the preferential adsorption of benzene in the troughs of standing waves of charge density, which are due to reflections of the wavefunction of a surface state at the steps and other defects [18].

The increased binding of benzene in the presence of CO can be explained by the electron acceptor and donor characteristics of these two molecules, as determined by work function measurements [16]. The back donation of electrons from the metal to the CO will create sites of low electron density around these molecules which favor the adsorption of benzene in nearby sites. The more tightly bound benzene-CO complex is less mobile on the surface which then becomes visible in the STM images.

As seen by LEED studies [4, 5], the ordered overlayers can be formed by either coadsorbing benzene on CO precovered surfaces or coadsorbing CO on benzene precovered surfaces. In our STM studies, adsorption of carbon monoxide on benzene precovered surfaces produced a c(2$\sqrt{3}$x4)rect structure, while benzene adsorption on CO precovered surface yields a (3x3) overlayer structure. These results are easy to understand, as the c(2$\sqrt{3}$x4)rect contains only one CO molecule and should form preferably on benzene-rich surfaces, while the (3x3) structure contains two CO molecules per unit cell and we expect it to form more easily on CO-rich surfaces. The formation of these mixed benzene/CO structures contrasts with the segregation observed in the case of sulfur and CO on Pt(111) and Re(0001) surfaces [19]. These effects of intercalation of

benzene and carbon monoxide correlate with the opposite electron transfer behavior of these molecules in the present experiments, while in case of sulfur and carbon monoxide, their similar electron acceptor characteristics drive them into segregation on the surface.

9.5 Conclusion

We have studied the effect of coadsorption of benzene and carbon monoxide on the Rh(111) surface. At saturation coverage, benzene does not form an ordered overlayer. Benzene adsorbs preferentially at steps at low coverage where it is immobile and can be imaged by STM, while on the terraces it diffuses rapidly. Carbon monoxide inhibits benzene diffusion and enhances the ordering of mixed coadsorbed surface structures. The opposite direction of the charge transfer between adsorbate and substrate for CO and benzene, and the attractive dipole-dipole interaction between these two adsorbates, contributes to the inhibition of diffusion and enhances the formation of ordered overlayers.

Chapter 9 References

1. B.E. Koel, J.E. Crowell, C.M. Mate, and G.A. Somorjai, Journal of Physical Chemistry, 1984. **88**: p. 1988.
2. B.E. Koel, J.E. Crowell, B.E. Bent, C.M. Mate, and G.A. Somorjai, J. Phys. Chem., 1986. **90**: p. 2949.
3. B.E. Koel and G.A. Somorjai, Journal of Electron Spectroscopy and Related Phenomena, 1983. **29**: p. 287.
4. R.F. Lin, R.J. Koestner, M.A. Van Hove, and G.A. Somorjai, Surf. Sci., 1983. **134**: p. 161.
5. R.F. Lin, G.S. Blackman, M.A. Van Hove, and G.A. Somorjai, Acta Cryst., 1987. **B43**: p. 368.
6. E. Bertel, G. Rosina, and F.P. Netzer, Surf. Sci., 1986. **172**: p. L515.
7. M.A. Van Hove, R.F. Lin, and G.A. Somorjai, Journal of American Chemical Society, 1886. **108**: p. 2532.
8. A. Barbieri, M.A. Van Hove, and G.A. Somorjai, Surf. Sci., 1994. **306**: p. 261.
9. F.P. Netzer and K.H. Frank, Phys. Rev. B, 1989. **40**: p. 5225.
10. T. McCabe and D.R. Lloyd, Surf. Sci., 1995. **333**: p. 88.
11. M. Neuber, F. Schneider, C. Zubragel, and M. Neumann, J. Phys. Chem., 1995. **99**: p. 9160.
12. H. Ohtani, R.J. Wilson, S. Chiang, and C.M. Mate, Phys. Rev. Lett., 1988. **60**: p. 2398.

13. S. Chiang, R.J. Wilson, C.M. Mate, and H. Ohtani, J. Microsc., 1988. **152**: p. 567.

14. S. Chiang, R.J. Wilson, C.M. Mate, and H. Ohtani, Vacuum, 1990. **41**: p. 118.

15. C.M. Mate and G.A. Somorjai, Surf. Sci., 1985. **160**: p. 542.

16. C.M. Mate, C.-T. Kao, and G.A. Somorjai, Surf. Sci., 1988. **206**: p. 145.

17. S.J. Stranick, M.M. Kamna, and P.S. Weiss, Surf. Sci., 1995. **338**: p. 41.

18. M.F. Crommie, C.F. Lutz, and D.M. Eigler, Nature, 1993. **363**: p. 524.

19. J.C. Dunphy, B.J. McIntyre, J. Gomez, D.F. Ogletree, G.A. Somorjai, and M. Salmeron, J. Chem. Phys., 1994. **100**: p. 6092.

Chapter 10

STM study of para- and meta-xylene and their coadsorption with carbon monoxide on Rh(111)

10.1 Introduction

In previous chapter, benzene and its coadsorption with carbon monoxide was studied with scanning tunneling microscopy. It was suggested that the attractive interaction between benzene and carbon monoxide causes the coadsorption system to be more stable. In order to confirm this hypothesis, another aromatic system was chosen to study its surface structure and the change in the structure when coadsorbed with carbon monoxide.

Xylene is a dimethyl benzene molecule that has been extensively studied in kinetic measurements (i.e. [1-3]), but nearly neglected by surface science. Only studies on the Pt(111) surface are available. HREELS, LEED and TPD studies were performed on para- and ortho-xylene on a Pt(111) surface [4]. It was found that xylene molecules

adsorb intact at 245 K with its aromatic ring parallel to the surface, but start to decompose at 350 K. Xylene molecules were chosen for this study since they do not decompose at room temperature (at least on Pt(111), but since Pt and Rh exhibit very similar catalytic characteristics, we do not expect otherwise), and because para-xylene adsorbed its aromatic ring parallel to the surface. As seen with benzene, since these molecules are derivatives of benzene, we do not expect them to be very mobile on the surface for our STM experiments. Xylene molecules also should behave as electron donors (if it is adsorbed through its aromatic ring), we can examine the change in the structure when coadsorbed with carbon monoxide. Xylene has three structural isomers, namely para-, meta- and ortho-xylene, thus allowing us to examine the difference in the structure and the behavior among the isomers.

In this work, we performed STM and LEED experiments on para-xylene (1,4 dimethyl benzene) and meta-xylene (1,3 dimethyl benzene) molecules and their coadsorption with carbon monoxide on Rh(111) surface.

10.2 Experiments

The experiments were carried out in the UHV chamber. The sample was cleaned with repeated cycles of Ar ion sputtering, annealing and oxygen treatment. The sample was flashed to 700 K just before each experiment to remove any contaminants from the surface.

Both para- and meta-xylene were purified by several freeze-thaw cycles. Mass spectrum did not show much increase in the mass 28 peak (corresponding to CO) during exposure to xylene. This way we can discard the possibility of contaminating the surface with CO when not desired. The sample was exposed to xylene at room temperature and its exposure ranges from 0.05 to 2 L. LEED patterns were recorded to characterize the ordering of xylene overlayers before and after the STM experiments. STM experiment were carried out at room temperature in topographic mode.

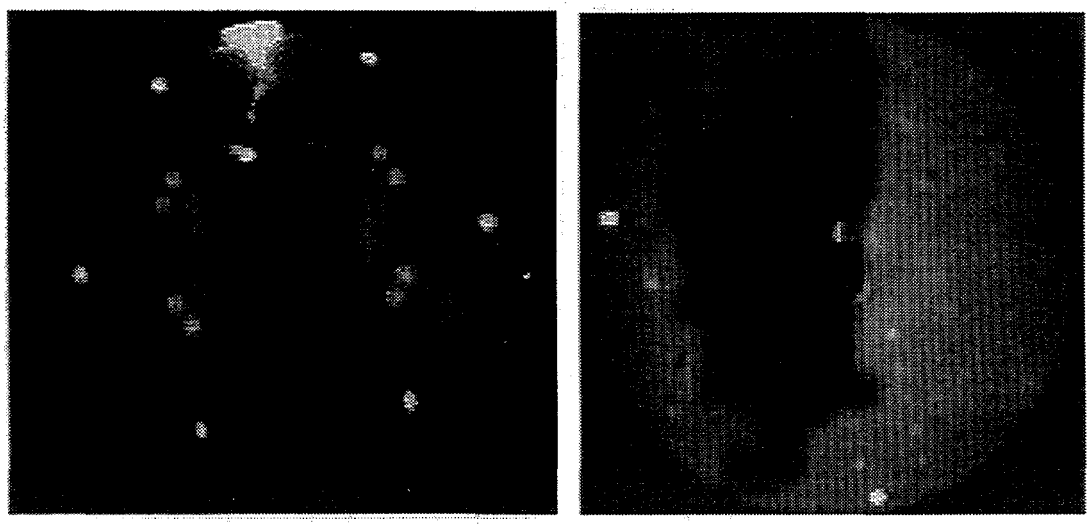

Figure 10.1 LEED patterns of Rh(111)-(6x3)-para-xylene overlayer at 48 eV (a) and 90 eV (b). Three fold symmetry and mirror plane can be seen.

10.3 Results

10.3.1 Surface structure of para xylene

When the sample was exposed to 2 L of para-xylene, a LEED pattern, such as in Figure 10.1, can be seen. It show ordering corresponding to a (6x3) overlayer with some background intensity. Figure 10.2 (a) is a topographic image of para-xylene at saturation coverage. First, para-xylene molecules cover the surface and ordered domains of para-xylene are observed. These domains are separated by steps and the rotational domain boundaries. The angle of the xylene molecules in different domains is measured to be 120° as expected from the surface with three-fold symmetry. The aromatic ring of the para-xylene molecule is visible and it appears to lie parallel to the surface. Para-xylene appears to have the shape of the molecule in the gas phase, as shown in Figure 10.2 (b). Two methyl groups in the para-xylene are imaged as lobes at the opposite end of the benzene ring. The depletion in the center of benzene ring was observed.

When 0.05 L of para-xylene is adsorbed on the surface, images like Figure 10.3 are obtained. Para-xylene molecules are more visible at the step edges. Even with low resolution of the image, the para-xylene molecules can still be identified by the shape of the molecule. At low coverage, preferential adsorption of para-xylene at the step edges is observed.

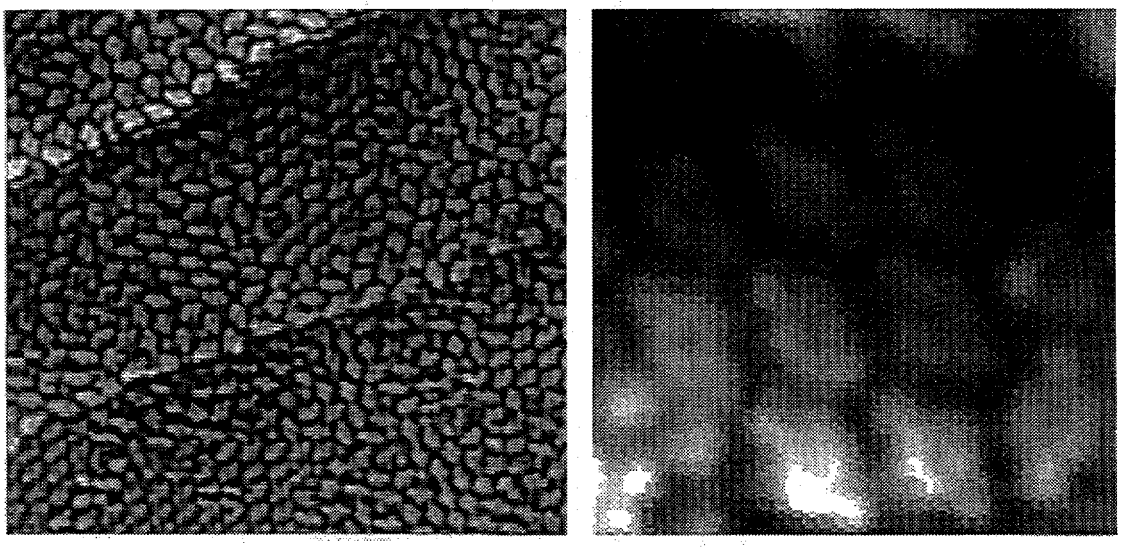

Figure 10.2 Topographic images of para-xylene on Rh(111) surface. (a) Large scan area image show the ordered domains of para-xylene separated by the steps and rotational domain boundaries. (b) Small, high resolution image shows the inner structure of para-xylene. Two methyl groups at the opposite end of benzene ring is visible.

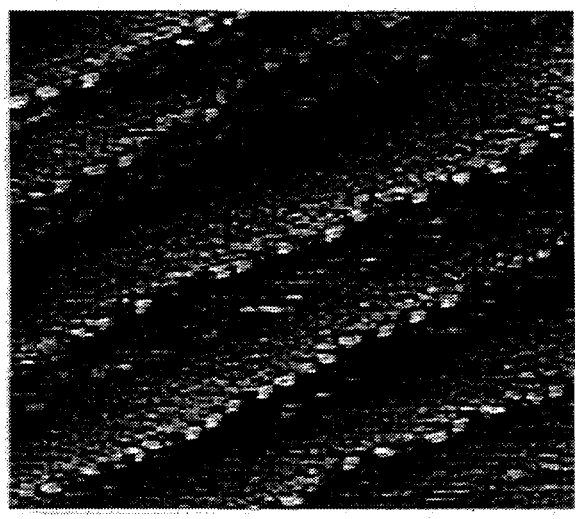

Figure 10.3 A topographic image of Rh(111) surface covered with 0.05 L of para-xylene. Para-xylene molecules are imaged at the step edges implying the preferential adsorption at the step edges.

10.3.2 Structure of meta-xylene

The LEED pattern in Figure 10.4 was obtained after the surface was covered with a saturation coverage of meta-xylene. This pattern corresponds to 'split' (2x2) overlayer. The LEED pattern has very high background intensities suggesting disorder of the surface overlayer. STM images in topographic mode were taken after the LEED pattern was observed. The image shows triangular features which are associated with adsorbed meta-xylene as shown in Figure 10.5. No long range order is apparent, however, the distance between meta-xylene molecules are about the twice the lattice parameter of the substrate. This is consistent with the LEED pattern observed. However, the reason why the shape of molecule in the STM images appears to be triangle is not clear at this moment. One reason may be due to the tilting of the molecule away from the surface. When 0.05 L of meta xylene is adsorbed on the surface, it covers only a small fraction of the surface as shown in Figure 10.6. Meta-xylene molecules are imaged both on the terrace and at the step edges indicating low mobility of these molecules.

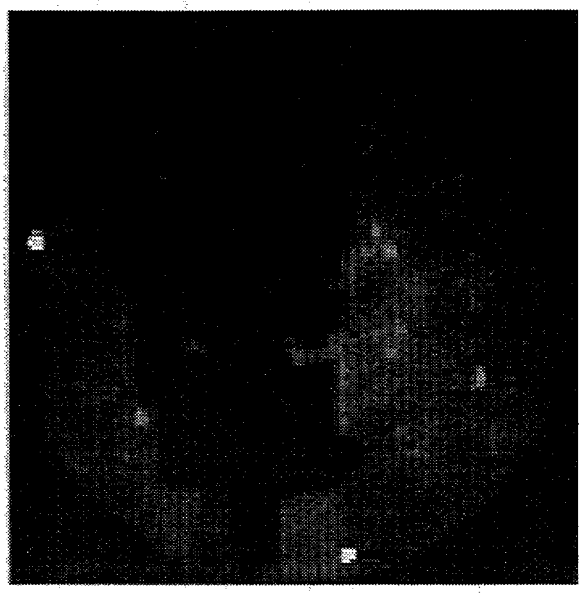

Figure 10.4 The 'split' (2x2) LEED pattern of meta-xylene on Rh(111) surface with high background intensities.

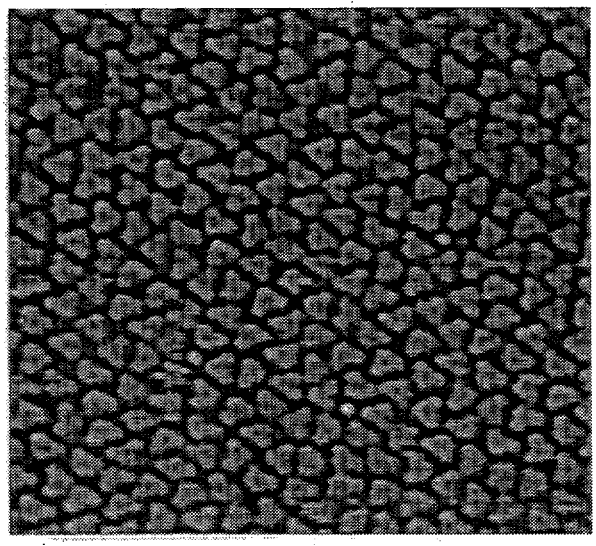

Figure 10.5 STM images of meta-xylene on Rh surface at saturation coverage. Meta-xylene molecules are imaged as triangular shapes. No long range order is observed, however, short range order is shown. The distance between meta-xylene molecules are twice the lattice parameter of the substrate which is consistent with the LEED.

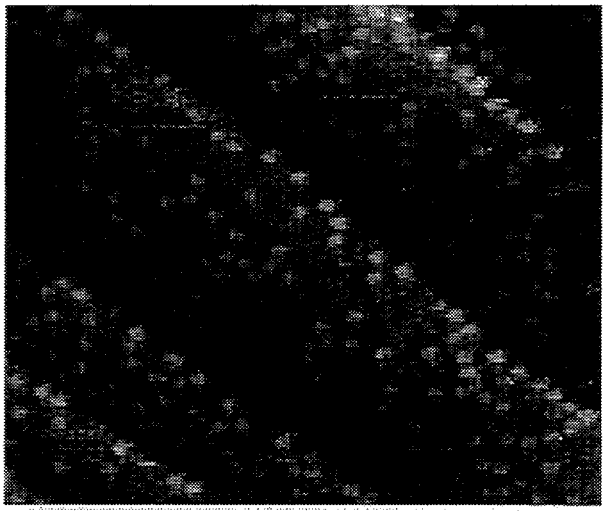

Figure 10.6 Topographic image of meta-xylene at low coverage. Meta-xylene molecules can be imaged both on the terrace and at the step indicating low mobility on the surface.

10.3.3 Coadsorption of xylene with carbon monoxide

Carbon monoxide was adsorbed prior to adsorption of xylene. The resulting LEED patterns are shown in Figure 10.7. Different LEED patterns observed relative to those without CO coadsorption, indicating that both para- and meta-xylene form different ordered overlayers with CO present on the surface. In case of meta-xylene, the LEED patterns become much sharper than without CO. This might indicate that CO enhancing the ordering of meta-xylene through the formation of meta-xylene + CO structure. Figure 10.8 is a topographic image of meta-xylene coadsorbed with CO. The features associated

with meta-xylene are imaged in the STM images. The distances between meta-xylene molecules are larger that those of meta-xylene molecules without CO. A detailed analysis of the LEED results are still in progress as well as additional STM experiments.

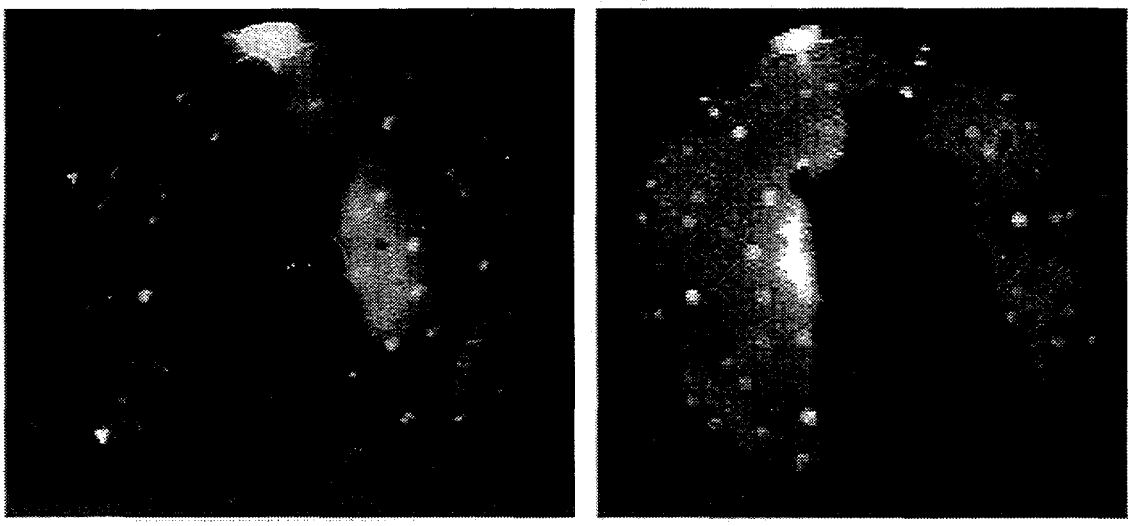

Figure 10.7 LEED patterns of para- (a) and meta-xylene (b) coadsorbed with carbon monoxide.

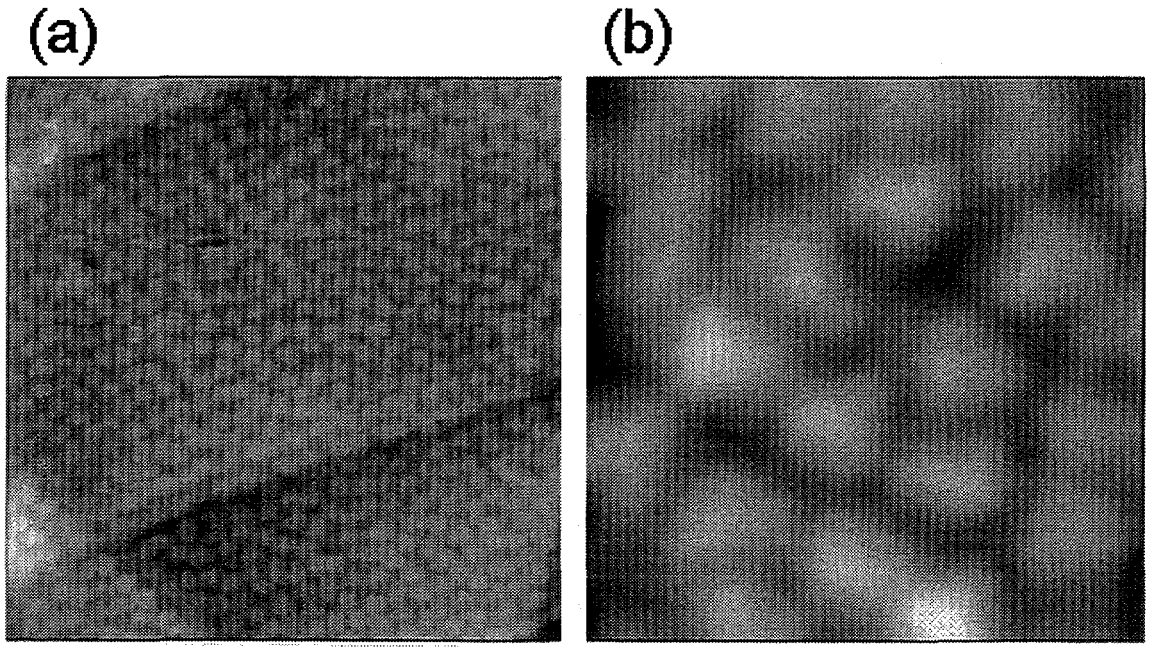

Figure 10.8 Topographic images of meta-xylene coadsorbed with carbon monoxide. Only the meta-xylene can be imaged. (a) 150 Å x 150 Å scan area, (b) 30 Å x 30 Å scan area image shows meta-xylene as triangular feather as seen before.

10.4 Discussion and Conclusion

The study of coadsorption was extended to the study of xylene and carbon monoxide. Two structural isomers were used in this study, para- and meta xylene. At the saturation coverage, para-xylene forms (6x3) ordered overlayers as observed by LEED. Para-xylene was imaged as a ring with two lobes at either end of the ring as one might expect from the its gas phase structure. This suggests adsorption through the π ring to the Rh(111) surface. STM also reveals that there are three rotational domains, rotated by 120°

relative to each other. In the case of meta-xylene, a 'split' (2x2) LEED pattern was observed at saturation coverage. However, weak diffraction spots and high diffuse background suggest weak ordering of the overlayer. STM experiments show no long range order of meta-xylene. These molecules appear as triangular shapes (rather than ring-like shape of its para-isomers) and show random orientation of the triangular features. This may result from the possible tilting of the meta-xylene on the surface. The average distance between the triangular features is about twice the lattice parameter of the substrate, which explains the LEED pattern. When coadsorbed with carbon monoxide, both xylenes form ordered overlayers that are different from those without the carbon monoxide. Para-xylene coadsorbed with CO produced different ordered overlayer by LEED. The LEED pattern of meta-xylene and CO shows improvement in the ordering as the diffraction spots are bright without much background intensity. Meta-xylene appears as triangle in the STM image. In both para- and meta-xylene cases, the carbon monoxide was not imaged by STM, either because of its rapid diffusion or because of the apparent height difference between carbon monoxide and xylene molecules. However, a STM image of meta-xylene and carbon monoxide shows the increase in the spacing between the meta-xylene molecules on the surface. These results suggest the intercalation of CO and metal-xylene on the surface. The studies of para- and meta xylene indicates that there is an attractive interaction between xylenes and carbon monoxide.

Chapter 10 References

1. R.G. Nigmatullin, T.S. Idirisova, A.M. Kashinikov, and R.A. Semina, Chem. & Tech. of Fuels and Oils, 1996. **32**: p. 7.
2. S. Smeds, T. Salmi, and D. Murizin, Applied Catalysis A, 1996. **145**: p. 235.
3. X.J. Zhao, T.G. Roberrie, and K.R. Rajagopalan, Applied Catalysis A, 1996. **145**: p. 407.
4. D.E. Wilk, C.D. Stanners, Y.R. Shen, and G.A. Somorjai, Surf. Sci., 1993. **280**: p. 298.

Chapter 11

Conclusion

Over the years, there has been an attempt to overcome the barrier between surface science and real chemistry that happens on the surface. Within its limit, surface chemistry and surface science of adsorbates still provide the information we need to understand real phenomena. On this line, my research has been focused on understanding of the nature of adsorbate-adsorbate interaction and adsorbate-substrate interactions, especially to elucidate the adsorbate-adsorbate interaction on metal surfaces. In order to achieve this, two different approaches were made.

The first approach is to study the coverage dependency of the overlayer of one atomic or molecular species on the metal surface. In this case, since the change of the interaction between the substrate and the adsorbate is not great, we can see the effect of the adsorbate-adsorbate interaction. On the other hand, since all heterogeneous catalysis involves many different species (i.e. reactants, products, promoters and poisons) on the

surface, it was necessary to study the effect of coadsorption which involves more than two species on the same substrate.

In the first category, the effect of the coverage on the change in the surface structures of sulfur on Pt(111) and Rh(111) was examined. It was found that sulfur atoms have thermodynamically stable sites on both surfaces, namely the fcc site, at low coverage of sulfur up to 0.33 monolayer (ML). However, when additional sulfur atoms were forced to adsorb on the substrate, sulfur overcome this difference in energy between different adsorption sites to accommodate more sulfur on the surface and minimize the repulsive interaction between the sulfur atoms and maximize the sulfur-sulfur distance. On Pt(111), sulfur forms p(2x2) overlayer when there is less than 0.25 ML of sulfur adsorbed, forming a more packed $(\sqrt{3}x\sqrt{3})R30°$ at 0.33 ML. On both structures, it was found that sulfur adsorbs only on fcc sites where it is most stable. However, when the coverage of sulfur exceeds 0.33 ML, it formed more complex $c(\sqrt{3}x7)$rect structure with 3 sulfur atoms per unit cell. On this structure, two different adsorption sites for sulfur atoms were observed - two on fcc sites and one on hcp site in the unit cell. This is indicative of overcoming the repulsive energy between the sulfur atoms by adsorbing sulfur on a hcp site. This becomes clearer when we adsorb sulfur on Rh(111). The lowest coverage of ordered sulfur formed on Rh(111) was the $(\sqrt{3}x\sqrt{3})R30°$ overlayer at 0.33 ML, in which the adsorption site of sulfur was determined to be fcc site by LEED. When the sulfur overlayer was compressed by adsorbing additional sulfur atoms on the surface, it forms a c(4x2) overlayer at 0.5 ML. The STM experiments clearly show that there are two different adsorption sites for sulfur in this structure and are proposed to have one fcc and one hcp site in the unit cell. This was confirmed by Mitchel et. al. who

performed dynamic LEED calculation on this structure. This is also another example of overcoming the repulsive interaction of adsorbates by having thermodynamically less-favorable adsorption sites, but maximizing the separation between adsorbates. The (4x4) overlayer can be formed at the same sulfur coverage as the c(4x2) structure as determined by Auger electron spectroscopy, but at higher annealing temperature. STM images of the (4x4) overlayer show that all sulfur atoms have the same adsorption site, presumably a fcc site, but the distances between sulfur atoms are much shorter than those for the c(4x2) structure. In this case, the repulsive energy between sulfur was overcome by forming a cluster-like structure. This is more evident in (7x7) structure, where it was proposed to have a surface sulfide formation with sulfur dissolved into subsurface. In order to accommodate large number of sulfur atoms on the surface, the substrate metal atoms may have gone through reconstruction to form a more energetically stable overlayer.

The structure of carbon monoxide gave another example of this adsorbate-adsorbate interaction on the Rh(111) surface. It has been observed that CO forms low coverage (2x2) at ¼ ML then transforms to split (2x2) overlayer then finally forms (2x2) with ¾ ML coverage. Usually these LEED experiments were carried out at low sample temperature to prevent CO desorption. However, at room temperature, it becomes a challenge. It has been known that small species such as oxygen atoms or CO molecules diffuse very fast on the surface at room temperature, and thus are not imaged with STM. To prevent or lower its diffusion, new methods were employed for this dissertation. In order to diffuse, there must be an empty site for CO to move, and these empty sites are created when chemisorbed CO molecules desorb from the surface. Thus, the background pressure of CO was maintained during our experiments to have a dynamic equilibrium

between desorption and adsorption of CO molecules. When the vacant sites were created, this can be filled by re-adsorption of CO from the gas phase. It was observed that this method was very effective to image carbon monoxide on the surface. The 'lower' coverage CO structure can be formed and imaged at 5 x 10^{-8} torr partial pressure of CO. The protrusion corresponding to the twice the lattice parameter of Rh was observed. This structure was determined to be the (2x2) overlayer at ¼ ML. When the partial pressure of CO was increased to 5 x 10^{-5} torr, another (2x2) overlayer was observed. The STM images reveal the formation of CO cluster. However, the detailed structure has not been determined yet.

The coadsorption system of benzene and carbon monoxide was studied to elucidate the interaction between different molecular species on a Rh(111) surface. Benzene molecules do not form a long range ordered overlayer on Rh(111) even at saturation coverage. When the coverage is approximately 0.5 monolayer, only the benzene molecules at the top side of the step edges were imaged, while those on the terraces could not be detected by the STM due to rapid diffusion. Coadsorption of carbon monoxide decreased the mobility of benzene which could then be imaged by STM. It was also found that carbon monoxide enhanced the surface ordering by formation of coadsorbed benzene/CO overlayers. The attractive interaction between benzene and carbon monoxide on Rh(111) surface contributes to the inhibition of the benzene diffusion and the enhancement of the surface overlayer ordering.

The study of coadsorption was extended to the study of xylene and carbon monoxide. Two structural isomers were used in this study, para- and meta xylene. At the saturation coverage, para-xylene forms ordered overlayer as observed by LEED. Para-

xylene was imaged as the ring with two lobes at either end of the ring as expected from the its gas phase structure, suggesting its adsorption through its π ring to Rh(111) surface. STM also reveals that there are three rotational domains each rotated by 120°. In the case of meta-xylene, the weak diffraction spots and the high diffuse background suggest weak ordering of overlayer. STM experiments show no long range order of the meta-xylene. They appeared as triangular shapes (rather than ring-like shape of its para-isomers) and shows the random orientation of the triangular features. This may result from the possible tilting of the meta-xylene on the surface suggesting that meta-xylene is bonded through its methyl group rather than π bonded through its aromatic ring. However, the average distance between these triangular features are about twice the lattice parameter of the substrate which explains the LEED pattern. When coadsorbed with carbon monoxide, both xylenes form ordered overlayers that are different from those without carbon monoxide. Para-xylene shows different ordering when coadsorbed with CO by LEED. The LEED pattern of meta-xylene and CO shows improvement in the ordering as the diffraction spots are bright without much back ground intensity. Meta-xylene still appears as a triangle in the STM image. The STM image of meta-xylene and carbon monoxide shows the increase in the spacing between the meta-xylene molecules on the surface. This result suggests the intercalation of CO and metal-xylene on the surface. The studies of para- and meta xylene indicate that there is an attractive interaction between xylenes and carbon monoxide.

The attempt has been made to understand the interaction between adsorbates through the studies of coverage dependency and coadsorption. It is clear from these studies that adsorbates on the metal surfaces will form the structure which has the lowest total energy. The increase in the total energy by additional adsorbates will also cause adsorbates

to form clusters or the substrate to reconstruct to form even surface sulfide. When electron donor molecules (such as benzene and xylene) and electron acceptor molecules (i.e. carbon monoxide) were coadsorbed on the surface, their attractive interaction drives the molecules to form more stable ordered overlayer. It was also found that one species can change the behavior of the other species on the surface such as the inhibition of diffusion and formation of well ordered overlayers.